2010-09-30

Generalized Acoustic Energy Density and Its Applications

Buye Xu
Brigham Young University - Provo

Generalized Acoustic Energy Density and Its Applications

Buye Xu

A dissertation submitted to the faculty of
Brigham Young University
in partial fulfillment of the requirements for the degree of

Doctor of Philosophy

Scott. D. Sommerfeldt, Chair
Timothy W. Leishman
Jonathon D. Blotter
Kent L. Gee
G. Bruce Schaalje

Department of Physics and Astronomy

Brigham Young University

December 2010

ABSTRACT

Generalized Acoustic Energy Density and Its Applications

Buye Xu

Department of Physics and Astronomy

Doctor of Philosophy

The properties of acoustic kinetic energy density and total energy density of sound fields in lightly damped enclosures have been explored thoroughly in the literature. Their increased spatial uniformity makes them more favorable measurement quantities for various applications than acoustic potential energy density (or squared pressure), which is most often used. In this dissertation, a new acoustic energy quantity, the generalized acoustic energy density (GED), will be introduced. It is defined by introducing weighting factors, α and $1-\alpha$, in the formulation of total acoustic energy density. With the additional degree of freedom, the GED can conform to the traditional acoustic energy density quantities, or be optimized for different applications. The properties and applications of the GED are explored in this dissertation. For enclosed sound fields, it was found that GED with $\alpha = 1/4$ is spatially more uniform than the acoustic potential energy density, acoustic kinetic energy density, and the total acoustic energy density, which makes it a more favorable measurement quantity than those traditional acoustic energy density quantities for many indoor measurement applications. For some other applications, such as active noise control in diffuse field, different values of α may be considered superior.

The numerical verifications in this research are mainly based on a hybrid modal expansion developed for this work, which combines the free field Green's function and a modal expansion. The enclosed sound field is separated into the direct field and reverberant field, which have been treated together in traditional modal analysis. Studies on a point source in rectangular enclosures show that the hybrid modal expansion converges notably faster than the traditional modal expansions, especially in the region near the source, and introduces much smaller errors with a limited number of modes. The hybrid modal expansion can be easily applied to complex sound sources if the free field responses of the sources are known. Damped boundaries are also considered in this dissertation, and a set of modified modal functions is introduced, which is shown to be suitable for many damped boundary conditions.

ACKNOWLEDGMENTS

I would like to express my gratitude to the following people:

Scott Sommerfeldt, my advisor, for his guidance and support through this research;

Timothy Leishman, for serving on my committee and his effort to improve the quality of this dissertation;

Jonathan Blotter, for serving on my committee and encouraging me to keep improving;

Kent Gee, for serving on my committee and sharing his experiences and thoughts with me;

Bruce Schaalje, for serving on my committee and helping me prepare for the qualifying exams;

Tracianne Neilsen, for leading me to my first academic conference and the continuous encouragement;

Diann Sorensen, for her efforts in making my graduate study smooth;

The **BYU Acoustics Research Group**, for the collaborations and support from all the students;

Jing Xu, **Qingmei Yang**, **Ping Xu** and **Hai Zhao** for raising me with love and always believing in me;

Jingjing Li, my wife, for her love, support, patience and everything else.

Contents

List of Figures

Chapter 1

Introduction

1.1 Background

Acoustic pressure, p, and acoustic particle velocity, $\mathbf{u}$, are two basic physical quantities describing sound waves in a fluid. In linear acoustics, these two quantities underlie two different forms of energy stored in acoustic waves: potential energy and kinetic energy. Energy per unit volume at a point in space is defined as the energy density. Since the pioneering work by W. C. Sabine,[1] localized measurements based on acoustic pressure, squared pressure, or acoustic potential energy density have become a primary focus for room acoustics. However several researchers have explored the benefits of the kinetic energy density and total energy density.

In the early 1930's, Wolff and Massa experimentally studied the kinetic energy density as well as total energy density in a room with the use of pressure gradient microphones.[2,3] His results showed a better spatial uniformity for both the kinetic energy density and total energy density over the potential energy density.

In 1974, a preliminary experimental study by Sepmeyer, *et al.*[4] showed that for a pure-tone diffuse sound field, the potential energy density has a relative spatial variance of one,

which is consistent with the theoretical results by Waterhouse[5] and Lyon.[6] In addition, they also found that the variance of potential energy density is approximately twice that of the total energy density. In the same year, Cook, *et al.* showed that the spatial variance of total energy density is smaller than that of the squared pressure for standing waves.[7]

Following Waterhouse's free-wave concept,[8,9] Jacobsen studied the statistics of acoustic energy density quantities from a stochastic point of view.[10] Moryl, *et al.*[11,12] experimentally investigated the relative spatial standard deviation of acoustic energy densities in a pure tone reverberant field with a four-microphone probe. Their results are in fair agreement with Jacobsen's prediction.

Jacobsen, together with Molares, revised his 1979 results[10] by applying the weak Anderson localization arguments,[13] and they were able to extend the free-wave model to low frequencies.[14,15] The new formulas for sound power radiation variance and ensemble variance of pure-tone excitations are very similar to those derived from the modal model[6,16,17] but with a simpler derivation. The same authors then investigated the statistical properties of kinetic energy density and total acoustic energy density in the low-frequency range.[18]

The pressure microphone gradient technique for measuring acoustic energy quantities has been studied and improved over time.[3,4,11,19–22] Recently, a novel particle velocity measurement device, the "Microflown" sensor, has been made available to acousticians,[23,24] which expanded the methods available to measure acoustic energy density quantities. With the improvement of the particle velocity measurement techniques, more and more attention is being devoted to energy density quantities. By recognizing the increased uniformity of the total energy density field, Parkins, *et al.* implemented active noise control (ANC) by minimizing the total energy density in enclosures. Significant global attenuation was achieved at low frequencies.[25,26] In 2007, Nutter, *et al.* investigated acoustic energy density quantities for several key applications in reverberation chambers and explored the benefits introduced

by the uniformity of both kinetic energy density and total acoustic energy density.[27]

Most studies of kinetic energy density and total energy density have focused on their improved uniformity in reverberant sound fields. A new energy density quantity, the generalized acoustic energy density (GED), will be introduced in this research and shown to potentially be more uniform than all other commonly used acoustic energy density quantities. In addition, with an additional degree of freedom, GED can be optimized for different applications. GED also requires no more effort to obtain than the total energy density.

1.2 Definition of the Classical Acoustic Energy Densities

1.2.1 Time Domain Definition

In linear acoustics, Euler's equation is one of the fundamental equations that describe the wave dynamics in a fluid:

$$\rho_0 \frac{\partial \mathbf{u}}{\partial t} = -\nabla p, \tag{1.1}$$

where ρ_0 is the ambient fluid density. Both $\mathbf{u}$ and p are functions with respect to time as well as space. Multiplying both sides of Eq. (1.1) by $\mathbf{u}$ leads to

$$\rho_0 \mathbf{u} \cdot \frac{\partial \mathbf{u}}{\partial t} = -\mathbf{u} \cdot \nabla p. \tag{1.2}$$

On the other hand, by taking the divergence of both sides of Eq. (1.1), we have

$$\rho_0 \nabla \cdot \frac{\partial \mathbf{u}}{\partial t} = -\nabla^2 p. \tag{1.3}$$

Considering the linear wave equation

$$\nabla^2 p - \frac{1}{c^2} \frac{\partial^2 p}{\partial t^2} = 0, \tag{1.4}$$

Eq. (1.3) becomes

$$\begin{aligned} & \rho_0 \nabla \cdot \frac{\partial \mathbf{u}}{\partial t} = -\frac{1}{c^2}\frac{\partial^2 p}{\partial t^2} \\ \Rightarrow \quad & \rho_0 \nabla \cdot \mathbf{u} = -\frac{1}{c^2}\frac{\partial p}{\partial t} \\ \Rightarrow \quad & \frac{1}{\rho_0 c^2} p \frac{\partial p}{\partial t} = -p \nabla \cdot \mathbf{u}. \end{aligned} \tag{1.5}$$

Adding Eq. (1.2) to Eq. (1.5) leads to

$$\begin{aligned} & \rho_0 \mathbf{u} \cdot \frac{\partial \mathbf{u}}{\partial t} + \frac{1}{\rho_0 c^2} p \frac{\partial p}{\partial t} = -\mathbf{u} \nabla p - p \nabla \cdot \mathbf{u} \\ \Rightarrow \quad & \frac{\partial}{\partial t}\left(\frac{1}{2}\frac{p^2}{\rho_0 c^2} + \frac{1}{2}\rho_0 \mathbf{u} \cdot \mathbf{u} \right) = -\nabla \cdot (p\mathbf{u}), \end{aligned} \tag{1.6}$$

which is often called the equation of conservation of energy. The right-hand side of Eq. (1.6) represents the net energy flowing into (or out of) an infinitesimal volume, which should be equal to the change of the acoustic energy stored in the volume. Therefore, $\frac{1}{2\rho_0 c^2} p^2 + \frac{1}{2}\rho_0 \mathbf{u} \cdot \mathbf{u}$ on the left-hand side of Eq. (1.6) must represent the total acoustic energy density $\mathcal{E}_T$, where $\frac{1}{2}\rho_0 \mathbf{u} \cdot \mathbf{u}$ represents the kinetic energy density $\mathcal{E}_K$ and $\frac{1}{2\rho_0 c^2} p^2$ represents the potential energy density $\mathcal{E}_P$.

For time harmonic sound fields, the time-averaged total acoustic energy density can be calculated as

$$\begin{aligned} \overline{\mathcal{E}_T} &= \frac{1}{\tau}\int_{\tau_0}^{\tau_0+\tau} \mathcal{E}_T \, dt \\ &= \frac{1}{\tau}\int_{\tau_0}^{\tau_0+\tau} \mathcal{E}_P \, dt + \frac{1}{\tau}\int_{\tau_0}^{\tau_0+\tau} \mathcal{E}_K \, dt \\ &= \frac{1}{4\rho_0 c^2}\tilde{p}^2 + \frac{1}{4}\rho_0 \tilde{u}^2, \end{aligned} \tag{1.7}$$

where $\tilde{p}$ and $\tilde{u}$ represent the peak amplitude of the pressure and particle velocity respectively. This expression is usually seen in the standard acoustics textbooks, and has been widely used by acousticians. However, it emphasized here that Eq. (1.7) is a time-domain expression and the corresponding frequency-domain expression will be studied in the next section.

1.2.2 Frequency Domain Definition

The corresponding frequency-domain quantities of acoustic pressure and particle velocity are usually defined as the Fourier transforms of them, meaning

$$\hat{p}(\omega) = \frac{1}{\sqrt{2\pi}} \int_{-\infty}^{\infty} p(t) e^{-iwt}\, dt, \tag{1.8}$$

$$\hat{\mathbf{u}}(\omega) = \frac{1}{\sqrt{2\pi}} \int_{-\infty}^{\infty} \mathbf{u}(t) e^{-iwt}\, dt, \tag{1.9}$$

and

$$p(t) = \frac{1}{\sqrt{2\pi}} \int_{-\infty}^{\infty} \hat{p}(\omega) e^{iwt}\, dt, \tag{1.10}$$

$$\mathbf{u}(t) = \frac{1}{\sqrt{2\pi}} \int_{-\infty}^{\infty} \hat{\mathbf{u}}(\omega) e^{iwt}\, dt. \tag{1.11}$$

However, the acoustic energy quantities are not usually developed with these expressions in the frequency domain because of the frequency shift caused by the squaring operations that are involved in obtaining the time-domain acoustic energy quantities. Instead, Parseval's theorem[28] is often used to derive the frequency-domain energy quantities from the time-averaged quantities so that they can match the correct energy values at each frequency. As an example, the frequency-domain total acoustic energy density is derived here based on the development of Parseval's theorem:

$$\int_{-\infty}^{\infty} \mathcal{E}_T\, dt = \int_{-\infty}^{\infty} \left(\frac{1}{2} \frac{p^2}{\rho_0 c^2} + \frac{1}{2} \rho_0 \mathbf{u} \cdot \mathbf{u} \right) dt \tag{1.12}$$

$$\begin{aligned} &= \frac{1}{4\pi \rho_0 c^2} \int_{-\infty}^{\infty} \left(\int_{-\infty}^{+\infty} \hat{p} \cdot e^{i\omega_1 t}\, d\omega_1 \right) \left(\int_{-\infty}^{+\infty} \hat{p}^* \cdot e^{-i\omega_2 t}\, d\omega_2 \right) dt \\ &\quad + \frac{\rho_0}{4\pi} \int_{-\infty}^{\infty} \left(\int_{-\infty}^{+\infty} \hat{\mathbf{u}} \cdot e^{i\omega_1 t}\, d\omega_1 \right) \cdot \left(\int_{-\infty}^{+\infty} \hat{\mathbf{u}}^* \cdot e^{-i\omega_2 t}\, d\omega_2 \right) dt \\ &= \frac{1}{2\rho_0 c^2} \int_{-\infty}^{+\infty} \hat{p} \hat{p}^*\, d\omega + \frac{\rho_0}{2} \int_{-\infty}^{+\infty} \hat{\mathbf{u}} \cdot \hat{\mathbf{u}}^*\, d\omega \end{aligned}$$

$$= \int_{-\infty}^{\infty} \left(\frac{1}{2\rho_0 c^2} \hat{p} \hat{p}^* + \frac{\rho_0}{2} \hat{\mathbf{u}} \cdot \hat{\mathbf{u}}^* \right) d\omega. \tag{1.13}$$

Comparison of Eq. (1.12) with Eq. (1.13) suggests that the total energy density in the frequency domain and the time domain can be matched if the frequency-domain total acoustic energy density is defined as

$$E_T = \frac{1}{2\rho_0 c^2}\hat{p}\hat{p}^* + \frac{\rho_0}{2}\hat{\mathbf{u}}\cdot\hat{\mathbf{u}}^*. \tag{1.14}$$

Similarly, for the potential energy density,

$$E_P = \frac{1}{2\rho_0 c^2}\hat{p}\hat{p}^*, \tag{1.15}$$

and for the kinetic energy density,

$$E_K = \frac{\rho_0}{2}\hat{\mathbf{u}}\cdot\hat{\mathbf{u}}^*. \tag{1.16}$$

In order to demonstrate that these quantities represent the correct energy values in the frequency domain, a special example is considered here for the potential energy density. Assuming a sinusoidal signal, the acoustic pressure can be written as

$$p(t) = Acos(\omega_0 t), \tag{1.17}$$

where A is the peak amplitude and w_0 is the angular frequency. The integration of the potential energy density time signal from $-\infty$ to ∞ can be calculated as

$$\begin{aligned}\int_{-\infty}^{\infty}\frac{1}{2}\frac{p^2}{\rho_0 c^2}\,dt &= \frac{A^2}{4\rho_0 c^2}\int_{-\infty}^{\infty}\left[cos^2(\omega_0 t) + sin^2(\omega_0 t)\right]\,dt \\ &= \frac{A^2}{4\rho_0 c^2}\int_{-\infty}^{\infty}1\,dt,\end{aligned} \tag{1.18}$$

which is infinity. In the frequency domain, we have

$$\hat{p}(\omega) = \frac{A\sqrt{2\pi}}{2}\left[\delta(\omega+\omega_0) + \delta(\omega-\omega_0)\right], \tag{1.19}$$

where δ represents the Dirac delta function. Substituting Eq. (1.19) into Eq. (1.15) and integrating within infinitesimal regions centered at $\pm\omega_0$ yields

$$\begin{aligned}
\int_{-\omega_0-}^{-\omega_0+} E_P\, d\omega + \int_{\omega_0-}^{\omega_0+} E_P\, d\omega &= \int_{-\infty}^{\infty} \frac{\pi A^2}{4\rho_0 c^2} \left[\delta(\omega+\omega_0) + \delta(\omega-\omega_0)\right]^2 d\omega \\
&= \frac{\pi A^2}{4\rho_0 c^2} \int_{-\infty}^{\infty} \delta^2(\omega+\omega_0) + \delta^2(\omega-\omega_0)\, d\omega \\
&= \frac{\pi A^2}{2\rho_0 c^2} \int_{-\infty}^{\infty} \delta^2(\omega-\omega_0)\, d\omega \\
&= \frac{\pi A^2}{2\rho_0 c^2} \int_{-\infty}^{\infty} \delta(\omega-\omega_0) \frac{1}{2\pi} \int_{-\infty}^{\infty} e^{i\omega t} e^{-i\omega_0 t}\, dt\, d\omega \\
&= \frac{A^2}{4\rho_0 c^2} \int_{-\infty}^{\infty} e^{-i\omega_0 t} \int_{-\infty}^{\infty} \delta(\omega-\omega_0) e^{i\omega t}\, d\omega\, dt \\
&= \frac{A^2}{4\rho_0 c^2} \int_{-\infty}^{\infty} 1\, dt, \qquad (1.20)
\end{aligned}$$

which is consistent with Eq. (1.18).

In practice, Fourier series are used to study infinite periodic signals in the frequency domain to avoid the Dirac delta function. The pressure signal in Eq. (1.19) can be written in terms of the complex Fourier series as

$$\begin{aligned}
p(t) &= \frac{A}{2} e^{-i\omega_0 t} + \frac{A}{2} e^{i\omega t} \\
&= \hat{p}(-\omega_0) e^{-i\omega_0 t} + \hat{p}(\omega_0) e^{i\omega t}. \qquad (1.21)
\end{aligned}$$

By implementing Eq. (1.15), the total energy at the frequencies $\pm\omega_0$ can be calculated as

$$\begin{aligned}
E_P(-\omega_0) + E_P(\omega_0) &= \frac{1}{2\rho_0 c^2} [\hat{p}^2(-\omega_0) + \hat{p}^2(\omega_0)] \\
&= \frac{A^2}{4\rho_0 c^2}, \qquad (1.22)
\end{aligned}$$

which is same as the time-averaged potential energy density $\overline{\mathcal{E}_P}$.

The frequency-domain expressions developed in this section [Eqs. (1.14) through (1.16)] differ from the widely used time-domain expressions by a factor of 1/2. Since the majority of the acoustic signals consist of an infinite number of frequency components and are

analyzed using Fourier transforms, it is more appropriate to utilize these frequency-domain expressions in practice. It needs to be noted, however, that the expressions developed in this section are based on the Fourier transform given by Eqs. (1.9) through (1.11), where the normalization factor $1/\sqrt{2\pi}$ is used for both forward and inverse transform. If other formulas are utilized, the frequency-domain expressions for the acoustic energy density quantities should be modified accordingly.

1.3 Enclosed Sound Fields

Several different theories have been developed by acousticians to study the sound fields inside rooms under different conditions.[29] Geometrical acoustics, for example, is widely used to study the high-frequency sound fields in large chambers. Statistical room acoustics is a very powerful tool to obtain the global information of the diffuse sound field, while wave (or modal) analysis, which is theoretically universal, is more suitable for low frequencies or small rooms.

1.3.1 Sound Field Prediction

Based on these theories, many methods for predicting the sound pressure field in rooms have been developed, including statistical energy analysis (SEA), classical modal analysis (CMA),[30,31] asymptotic modal analysis (AMA),[32] ray tracing techniques, finite element method (FEM), and so on. SEA and AMA are particularly well-suited for systems which have high modal density and light damping. Ray tracing techniques are powerful for large rooms at high frequencies. The other methods are typically applicable in the low-frequency range.

A perturbation theory was developed to treat the effects of damping[33] and has been

successfully applied to the low-frequency range.[34] CMA also has the capability of computing the acoustic field in damped enclosures, but the extensive computations required restrict it to a very low frequency range.[35]

Thus far, no method has been shown to be excel in the mid-frequency range, especially for highly damped enclosures. In addition, the accuracy of applying current methods to predict particle velocity has not been carefully studied.

1.3.2 Statistical Room Acoustics

The diffuse sound field can be considered as the superposition of many elementary waves coherently interfering with random phases. The maxima and minima of the field form a random pattern referred to as a speckle pattern. Schroeder intensively studied the statistical properties, resulting in rooms which resulted in the wave statistical theory of room acoustics.[36]

1.4 Research Objectives and Dissertation Outline

The main objective of this research is to develop the concept of generalized acoustic energy density (GED). The properties and applications of the GED are explored for enclosed sound fields in both low and high-frequency ranges. Analytical, numerical and experimental studies are carried out.

In Chapter 2, a hybrid modal expansion that combines the free field Green's function and a modal expansion will be presented, based on a review and an extension of the existing modal analysis theories for the sound fields in enclosures. Damped boundaries will also be considered, and a set of modified modal functions will be introduced and shown to be suitable for many damped boundary conditions. The hybrid modal expansion will be utilized

throughout this dissertation as an important numerical simulation tool. The concept and properties of the GED will be introduced in Chapter 3. Its behavior will be explored for room modes, for sound fields below the Schroeder frequency, and for diffuse fields. Computer simulation results will be presented to validate some of the GED properties. In Chapter 4, methods for measuring the GED will be introduced, and two GED-based reverberation chamber measurement techniques will be studied. The active noise control of enclosed sound fields will be studied in Chapter 5. Again, the GED-based techniques will be explored in both the low and high-frequency ranges. Conclusions and suggestions for future research are found in Chapter 6.

1.5 Significance of the Dissertation

The generalized acoustic energy density (GED) is introduced and systematically studied for the first time in this dissertation. The GED is defined by introducing weighting factors in the formulation of total acoustic energy density. It effectively incorporates different traditional acoustic energy density quantities (E_P, E_K and E_T) within a single quantity by proper choice of the weighting factors. The related theories thus become more complete and general. Although the GED itself is not a fixed physical quantity, its study and use can help acousticians better understand the physics behind various acoustic phenomena.

With an additional degree of freedom, the GED can not only conform to the traditional acoustic energy density quantities, but more importantly, it can be optimized for different applications. Results in this dissertation show that by choosing appropriate weighting factors, one can utilize the GED to improve existing indoor acoustic measurement techniques and active noise control techniques. In addition, the GED and the ideas behind it have the potential to be utilized in a much wider range of applications.

To carry out this research, there was a great need for a computational tool to compute

enclosed sound fields at both low frequencies and high frequencies. A hybrid modal expansion that combines the free-field Green's function and a modal expansion has been developed and shown to have dramatically improved performance over the widely used classical modal expansions, especially in the spatial region near the source or in situations where damped boundaries exist.

Chapter 2

A Hybrid Modal Analysis

2.1 Introduction

Modal analysis (MA) has been widely used to study the low frequency response in enclosed sound fields. The fundamental idea of modal analysis is to express an acoustic field quantity as the summation of a complete set of properly weighted modal functions. The weighting factors are often called the modal amplitudes. The summation usually has an infinite number of terms; therefore MA is generally not a closed form solution. However, given that this infinite series converges, one can in practice truncate it to a finite summation and still reach the desired accuracy in the low frequency range. For high frequencies, where a very large number of modal functions must be included to achieve an acceptable accuracy, MA is less applicable.

Normal mode analysis (NMA)[37] is probably the simplest and most widely used modal analysis in the literature. It is, however, only suitable for enclosures with rigid or very lightly damped boundaries. Dowell, *et al.* developed a more comprehensive modal analysis theory, the so-called classical modal analysis (CMA), which is based on the Green's divergence theorem.[31] It is capable of computing sound fields in damped enclosures but, as a consequence,

the modal functions are coupled and the convergence speed is usually very slow.[35] Both NMA and CMA use the same set of eigenfunctions solved from an eigenvalue problem as the modal functions, but have different mechanisms to generate the modal amplitudes. These eigenfunctions are called the "normal modes" in this chapter to distinguish from other sets of modal functions discussed later. The normal modes and their linear combination only satisfy rigid boundary conditions; therefore, large errors are often observed in the regions near damped boundaries. This issue can be understood in terms of the Gibb's phenomenon.[38]

The eigenfunctions that satisfy the same boundary conditions as the enclosure can be solved numerically from an exact eigenvalue problem[39,40] and are called "exact modes" in this chapter. They are uncoupled and automatically match the boundary conditions, which make them very good candidates for the modal functions of modal analysis.[40] However, there are several negative properties associated with them. First of all, the completeness of this set of functions is always assumed without being proven. Second, the "orthogonality" relationship among these functions is abnormal, which may cause inconvenience for many applications. Finally, solving the exact eigenvalue problem involves numerical root searching in the complex domain which is complicated and time consuming. Because of these disadvantages, MA using the exact modes (exact modal analysis or EMA) is not utilized much in the literature.

In this chapter, a new set of modal functions (modified modes), which partially satisfy the boundary conditions, will be introduced. Compared to the normal modes, modified modes are also coupled, but can be easily simplified in many cases. Modal analysis based on the modified modes (MMA) also introduces errors on boundaries but performs better than CMA. Unlike the exact modes, modified modes are orthogonal and complete. Although a numerical root search is still required, only real values need to be considered, which greatly simplifies the searching algorithm.

In the literature related to modal analysis, distributed sources on boundaries, such as a piston source mounted on the inside surface of a room, are often considered. Point sources, though more fundamental and very important for many applications such as sound power prediction for sources inside rooms, active noise control, and so on, are not sufficiently studied, partially due to the very slow convergence rate of MA in the near field. Maa proposed a method of introducing the free-field Green's function (FFGF) in addition to the MA solution for sound fields, which essentially divides the sound field into a direct field and a reverberant field.[41,42] Although his development was based on a faulty assumption that the classical modes are not complete, the idea of dividing the enclosure's sound field into a direct field and a reverberant field has merit.

In this chapter, a hybrid model that combines the free-field Green's function and a modal expansion will be presented based on a rigorous mathematical derivation. Examples shown later confirm that this hybrid method not only greatly improves the convergence rate, but also provides a better way to study the physical properties of enclosed sound fields. For a complex source, the hybrid method can be easily modified by replacing the FFGF with the free-field response of the source. A simple example will be given in Section 2.4.3.

This chapter is organized as follows. In Section 2.2, the general theory of modal expansion will be reviewed; a modified modal expansion and a hybrid model will also be introduced. In Section 2.3, results of different modal expansion models will be compared and discussed for both one dimensional and three dimensional cases. Further examples of implementing the hybrid modal expansion will be discussed in Section 2.4.

2.2 Theoretical Derivation

Inside an enclosure, the sound pressure field excited by a point source satisfies the wave equation

$$\nabla^2 p - \frac{1}{c^2}\frac{\partial^2 p}{\partial t^2} = -Q_0\,(t)\,\delta(\boldsymbol{r}-\boldsymbol{r}_o), \tag{2.1}$$

where p is the sound pressure, c represents the speed of sound, and $Q_0\,(t)\,\delta(\boldsymbol{r}-\boldsymbol{r}_o)$ represents the point source. Taking the Fourier transform of both sides yields the inhomogeneous Helmholtz equation:

$$\nabla^2 \hat{p} + k_o^2 \hat{p} = -\hat{Q}_0\,(\omega_0)\,\delta\,(\boldsymbol{r}-\boldsymbol{r}_o)\,, \tag{2.2}$$

where $\hat{\cdot}$ indicates a complex frequency-domain quantity, ω_0 is the excitation frequency, and k_0 is the acoustic wave number.

The boundary condition is usually assumed to be locally reacting and given as follows:

$$\frac{\partial \hat{p}}{\partial \boldsymbol{n}} \Big/ \hat{p}\Big|_S = \beta = -ik_0\frac{\rho_0 c}{z}, \tag{2.3}$$

where ρ_0 is the ambient air density, z is the specific acoustic impedance of the boundary, and β is the normalized specific acoustic admittance. Note that this β differs from the standard definition of the specific acoustic admittance by the constant $-ik_0\rho_0 c$, which is a pure imaginary number.

The solution, $\hat{p}$, can be expressed as a linear combination of modal functions, ψ_n,

$$\hat{p} = \sum_{n=1}^{N} q_n \psi_n, \tag{2.4}$$

where the modal amplitude, q_n, can be complex and N is the total number of modal functions. [These modal functions are spatially dependent, *i.e.* $\psi_n = \psi_n(\vec{r})$, but for notational simplicity, the spatial dependence is omitted here.] From Euler's equation, one can easily obtain the modal expression for particle velocity (assuming $e^{i\omega t}$ time dependence),

$$\hat{\boldsymbol{u}} = -\frac{1}{i\omega\rho_0}\sum_{n=1}^{N} q_n \nabla\psi_n. \tag{2.5}$$

A frequent choice for ψ_n is the set of eigenfunctions for the following eigenvalue problem:

$$\nabla^2\psi_n = \lambda_n\psi_n = -k_n^2\psi_n, \tag{2.6a}$$

$$\frac{\partial\psi_n}{\partial\boldsymbol{n}}/\psi_n\bigg|_S = \beta', \tag{2.6b}$$

where λ_n denotes the eigenvalue. Different values of β' are used to generate different modal functions. For example, zero is used for the classical modes while β is used for the exact modes. Literally, β' could be any value of choice. However, if it is real the eigenvalues are real and the resulting modal functions are guaranteed to be complete and orthogonal.[38] Orthogonality implies $C_{mn} = \iiint_V \psi_m^*\psi_n\, d^3x = \Lambda_{mn}\delta_{mn}$, where δ_{mn} is the Kronecker delta function, and Λ_{mn} is a normalization constant. The eigenvalues are often assumed nonpositive, and thus written as $-k_n^2$ as shown in Eq. (2.6a), but they could be positive if $\beta' < 0$ for some or all of the boundary.

To solve for q_n, the Green's theorem can be applied as follows:

$$\iiint_V \left(\psi_m^*\nabla^2\hat{p} - \hat{p}\nabla^2\psi_m^*\right)\, d^3x = \oint_S \left(\psi_m^*\frac{\partial\hat{p}}{\partial\boldsymbol{n}} - \hat{p}\frac{\partial\psi_m^*}{\partial\boldsymbol{n}}\right)\, da, \tag{2.7}$$

where the volume integral covers the entire volume inside the enclosure, and the surface integral is evaluated on the entire inside surface of the enclosure. Substitution of Eqs. (2.2), (2.3) and (2.6) into Eq. (2.7) gives

$$\begin{aligned}
&\iiint_V \left[-\hat{Q}_0\delta\left(\boldsymbol{r}-\boldsymbol{r}_0\right)\psi_m^* - k_o^2\hat{p}\,\psi_m^* + k_m^2\hat{p}\,\psi_m^*\right]\, d^3x = \oint_S \left(\beta-\beta'\right)\hat{p}\,\psi_m^*\, da \\
\Rightarrow\quad &\iiint_V \left(k_0^2 - k_m^2\right)\hat{p}\,\psi_m^*\, d^3x + \oint_S \left(\beta-\beta'\right)\hat{p}\,\psi_m^*\, da = -\hat{Q}_0\psi_m^*(\boldsymbol{r_o}) \\
\Rightarrow\quad &\sum_n \left(k_0^2 - k_m^2\right) C_{mn}q_n + \sum_n D_{mn}q_n = -\hat{Q}_0\psi_m^*(\boldsymbol{r_o}) \\
\Rightarrow\quad &\sum_n \left[\left(k_0^2 - k_m^2\right) C_{mn} + D_{mn}\right] q_n = -\hat{Q}_0\psi_m^*(\boldsymbol{r_o}),
\end{aligned} \tag{2.8}$$

where $D_{mn} = \oint_S (\beta - \beta')\, \psi_m^* \psi_n \, da$. Thus, q_n can be solved from this linear equation group, which can also be written in matrix form as

$$\begin{bmatrix} (k_0^2 - k_1^2)\, C_{11} + D_{11} & D_{12} & \cdots \\ D_{21} & (k_0^2 - k_2^2)\, C_{22} + D_{22} & \cdots \\ \vdots & \vdots & \ddots \end{bmatrix} \cdot \begin{bmatrix} q_1 \\ q_2 \\ \vdots \end{bmatrix} = \begin{bmatrix} -\hat{Q}_0 \psi_1^*(\boldsymbol{r_o}) \\ -\hat{Q}_0 \psi_2^*(\boldsymbol{r_o}) \\ \vdots \end{bmatrix}, \tag{2.9}$$

or

$$A \cdot Q = B, \tag{2.10}$$

where $A_{mn} = (k_0^2 - k_m^2)\, C_{mn} + D_{mn}$, $Q_n = q_n$, and $B_m = -\hat{Q}_0 \psi_m^*(\boldsymbol{r_o})$.

As mentioned at the beginning of this chapter, the number N of modal functions is in principle infinite. Moreover, the matrix A is, while often sparse and Hermitian, nondiagonal. Therefore, the q_n's are coupled and it is impossible to obtain an exact solution. In practice, however, if q_n goes to zero quickly enough as n goes to infinity, it is possible to keep only a finite number of ψ_n's as well as q_n's and obtain a desired level of accuracy.

Results that have been developed can be applied to enclosures of any shape. However, this chapter will only focus on rectangular shapes. In particular, the dimensions of the rectangular enclosure are $L_x \times L_y \times L_z$ and one of the corners sits at the origin with the three adjoining edges lying along the positive directions of the x, y and z axes. In addition, it is assumed that the specific acoustic admittance, β, is constant for each of the boundaries, and denoted by β_{x0}, β_{xL}, β_{y0}, β_{yL}, β_{z0} and β_{zL}, where β_{x0} stands for β at $x = 0$, β_{xL} stands for β at $x = L_x$, and so forth.

2.2.1 Classical Modal Analysis

For classical modal analysis, β' in Eq. (2.6b) is set to zero. Therefore, the eigenfunctions (normal modes) and eigenvalues can be solved easily for rectangular enclosures:

$$\psi_n = \psi_{lmo} = \cos(k_{xl}x)\cos(k_{ym}y)\cos(k_{zo}z); \tag{2.11a}$$

$$k_{xl} = \frac{l\pi}{L_x},\ k_{ym} = \frac{m\pi}{L_y},\ k_{zo} = \frac{o\pi}{L_z},$$

$$k_n^2 = k_{xl}^2 + k_{ym}^2 + k_{zo}^2, \tag{2.11b}$$

where l, m, and o are nonnegative integers.

This set of normal modes is complete and orthogonal because β' is real, but it is always infinite and usually coupled for non-rigid boundaries. The hope here is that q_n converges to zero quickly so that truncations can be made. Moreover, if the damping is small, or more precisely if $\beta - \beta' \ll 1$, A_{mn} can be "uncoupled" by setting non-zero off-diagonal terms to zero to simplify the computation.[31] Studies on one-dimensional (1-D) sound fields in ducts show that when damping is added to the system, the coupled model has to be considered and many more iterations are needed.[35,43] Pan also points out that even if a large number of terms are included, the coupled model still converges poorly for the acoustic intensity.[43] The classical modal analysis converges slowly not only for the acoustic intensity but also for sound pressure as well as particle velocity, especially in the spatial region close to the boundaries. All these disadvantages are largely due to the fact that the classical modes only satisfy the rigid boundary condition ($\beta' = 0$) which could be greatly different from the true physical boundary conditions β and result in large off-diagonal terms in matrix A.

2.2.2 Modified Modal Function

As mentioned earlier, the choice of the boundary conditions for the modal functions (β') could be arbitrary. The exact modal analysis sets $\beta' = \beta$, which matches the true physical

boundary and, in turn, automatically diagonalizes the matrix A. However, since the value of β is usually complex, the completeness and orthogonality of the exact modes are not mathematically solid. In order to reduce the effects of off-diagonal terms in the matrix A of Eq. (2.10), while keeping β' real, a good choice for β' is to set it equal to the real part of β. The modified modes can thus be solved for from Eq. (2.6) and have the form

$$\begin{aligned}\psi_n = \psi_{lmo} &= \left[\cos(k_{xl}x) - \frac{\beta'_{x0}}{k_{xl}}\sin(k_{xl}x)\right] \\ &\cdot \left[\cos(k_{ym}y) - \frac{\beta'_{y0}}{k_{ym}}\sin(k_{ym}y)\right] \\ &\cdot \left[\cos(k_{zo}z) - \frac{\beta'_{z0}}{k_{zo}}\sin(k_{zo}z)\right], \end{aligned} \tag{2.12}$$

where k_{xl}, k_{ym}, and k_{zo} can be solved from the following equations:

$$\begin{aligned}\tan(k_{xl}\cdot L_x) &= \frac{(\beta'_{x0}+\beta'_{xL})k_{xl}}{\beta'_{x0}\cdot\beta'_{xL}-k_{xl}^2}, \\ \tan(k_{ym}\cdot L_y) &= \frac{(\beta'_{y0}+\beta'_{yL})k_{ym}}{\beta'_{y0}\cdot\beta'_{ym}-k_{ym}^2}, \\ \tan(k_{zo}\cdot L_z) &= \frac{(\beta'_{z0}+\beta'_{zL})k_{zo}}{\beta'_{z0}\cdot\beta'_{zL}-k_{zo}^2}. \end{aligned} \tag{2.13}$$

The general derivation carried out at the beginning of Section 2.2 [Eqs. 2.4 through 2.10] is also applicable for modal analysis based on this new set of modal functions.

Generally, the values of k_{xl}, k_{ym}, and k_{zo} in Eqs. (2.13) cannot be solved analytically, and thus a numerical method is needed. Because β' is real, these modified modes are complete and orthogonal. The eigenvalues, $\lambda_n = -k_n^2$, are real, but they could be positive for stiffness-like boundary conditions. Therefore, k_{xl}, k_{ym}, and k_{zo} could be pure imaginary numbers.

The matrix A is still not diagonal, since $D_{mn} \neq 0$. However, unlike normal modes, this new set of modal functions do not reach maxima on the boundary and, in addition, the value of β' reduces the value of $\beta - \beta'$, which can be found in the expression for D_{mn}, which implies a reduced effect of the off-diagonal terms, D_{mn}, in A. Because the boundary condition is

partially satisfied, the modified modal analysis is expected to perform better than normal modal analysis.

2.2.3 Hybrid Modal Analysis

Due to the singular nature of a point source, all the modal models discussed earlier converge very slowly at field points close to a point source. In order to overcome this problem, a free-field Green's function is introduced to the solution of Eq. (2.2):

$$\hat{p}(\boldsymbol{r}) = G(\boldsymbol{r}|\boldsymbol{r_o}) + F(\boldsymbol{r}), \tag{2.14}$$

where $G(\boldsymbol{r}|\boldsymbol{r_o})$ represents the pressure field associated with the free-field Green's function that satisfies Eq. (2.2) by itself, and $F(\boldsymbol{r})$ is a solution of the homogenous Helmholtz equation. $G(\boldsymbol{r}|\boldsymbol{r_o})$ can be expressed as

$$G(\boldsymbol{r}|\boldsymbol{r_0}) = \frac{\hat{Q}_0\left(\omega_o\right)}{4\pi\left|\boldsymbol{r}-\boldsymbol{r}_o\right|} e^{-i\boldsymbol{k}_o\cdot(\boldsymbol{r}-\boldsymbol{r}_o)}, \tag{2.15}$$

where $\boldsymbol{r_o}$ designates the location of the point source.

From the point of view of room acoustics, the sound field is then divided into a direct field, $G(\boldsymbol{r}|\boldsymbol{r_0})$, and a reverberant field, $F(\boldsymbol{r})$. For the near field, the direct field dominates; at large distances, the direct field decays at a rate proportional to $\frac{1}{|\boldsymbol{r}-\boldsymbol{r_o}|}$, and eventually, beyond a certain distance, the reverberant field becomes stronger than the direct field. Note that neither $G(\boldsymbol{r}|\boldsymbol{r_o})$ nor $F(\boldsymbol{r})$ satisfies the boundary condition represented by Eq. (2.3), but together they can potentially be constructed to do so.

The solution $F(\boldsymbol{r})$ can be solved in terms of modal expansions, and any modal functions can be used. However, on one hand, because the reverberant field often dominates on the boundaries, a modal function set that can better match the boundary condition is desired; on the other hand, the exact modes may not be the best candidates since, in addition to the issue of completeness and orthogonality, $F(\boldsymbol{r})$ should not satisfy the boundary condition

by itself, *i.e.*, without the addition of $G(\boldsymbol{r}|\boldsymbol{r_0})$. Therefore, the modified modes are expected to be desirable candidates. The mode amplitudes, q_n, can be solved by means very similar to those shown previously. The only difference is that the right hand side of Eq. (2.8) is modified and the new equation reads

$$\sum_n \left[\left(k_0^2 - k_m^2\right) C_{mn} + D_{mn}\right] q_n = -\oint_S \psi_m^* \left(\beta G - \frac{\partial G}{\partial \mathbf{n}}\right) da. \tag{2.16}$$

Consequently, the B matrix in Eq. (2.10) is modified to $B_m = -\oint_S \psi_m^* \left(\beta G - \frac{\partial G}{\partial \mathbf{n}}\right) da$. Note that B_m now involves a surface integral which may not be easy to evaluate analytically, but a numerical evaluation is generally straightforward. By recognizing the spherical spreading nature of G and $\partial G/\partial \mathbf{n}$ one can mesh the surface S accordingly to make the computation more efficient.

2.3 Comparisons

2.3.1 Normal Modes vs. Modified Modes in One-dimensional (1-D) Cases

The sound wave inside a 1-D plane wave duct has been covered extensively by many authors.[28,44,45] The exact closed-form solution for this problem provides a benchmark with which modal analysis results can be compared.[35,43,46]

Assume that the 1-D duct has a length, L, and that, for simplicity, two terminations are made of the same material with the specific acoustic impedance, z. A plane monopole source driven at frequency f_0 is located inside the duct at x_o. The governing equation for this problem is

$$\frac{d^2\hat{p}}{dx^2} + k_0^2\hat{p} = -\hat{Q}_0\delta(x - x_0). \tag{2.17}$$

The exact plane wave solution for the sound pressure can be written as

$$\hat{p}_{exact} = -\hat{Q}_0(A\cos k_0 x + B\sin k_0 x), \tag{2.18}$$

where

$$A = \begin{cases} \frac{k_0\cos[k_0(L-x_0)]-\beta\sin[k_0(L-x_0)]}{2k_0\beta\cos k_0 L+(k_0^2-\beta^2)\sin k_0 L} & \text{if } x < x_0 \\ \\ \frac{(k_0-\beta\tan k_0 L)(k_0\cos k_0 x_0-\beta\sin k_0 x_0)}{k_0[2k_0\beta+(k_0^2-\beta^2)\tan k_0 L]} & \text{if } x > x_0 \end{cases},$$

$$B = \begin{cases} -A\cdot\frac{\beta}{k_0} & \text{if } x < x_0 \\ \\ A\cdot\frac{\beta\cos(k_0 L)+k_0\sin(k_0 L)}{k_0\cos(k_0 L)-\beta\sin(k_0 L)} & \text{if } x > x_0 \end{cases},$$

and β can be found in Eq. (2.3). The exact solution for the particle velocity can be solved from Euler's equation:

$$\hat{v}_{exact} = \frac{-i\hat{Q}_0}{\rho_0 c}\left(A\sin k_0 x - B\cos k_0 x\right). \tag{2.19}$$

The modal expansion solution of Eq. (2.17) can be solved for from Eqs. (2.4) though (2.10) and reads

$$\hat{p}_{modal} = \sum_{n=1}^{N} q_n\psi_n. \tag{2.20}$$

For modal function sets studied in Section 2.2, k_n can be solved from Eq. (2.13), which can be simplified to the following equations for the 1-D plane wave duct

$$k_n\cdot\tan(\frac{k_n L}{2}) = -\beta', \tag{2.21a}$$

$$k_n\cdot\cot(\frac{k_n L}{2}) = \beta'. \tag{2.21b}$$

Note that each equation above by itself only provides half of the solution set for k_n, but the latter equation, Eq. (2.21b), is found missing in some of the literature.[37,40,44] The roots of these two equations could be imaginary numbers if the boundaries are represented by a

Table 2.1 1-D Ducts for Comparing Modal Models.

	$z/\rho_o c$	α_n
Lightly Damped Duct	$50 + 50i$	0.04
Damped Duct 1	$7 - 4.8i$	0.32
Damped Duct 2	$2 + 4i$	0.32

stiffness. However, for this case there should be no more than one imaginary root for each of these equations. For these roots, one can simply replace the trigonometric functions in Eqs. (2.21) by the corresponding hyperbolic functions to maintain the root search in the real domain.

The error associated with modal expansion solutions can be indicated by a single value:

$$Error_p = \sqrt{\frac{\int_0^L |\hat{p}_{modal} - \hat{p}_{exact}|^2 \, dx}{\int_0^L |\hat{p}_{exact}|^2 \, dx}}, \tag{2.22}$$

Although only the sound pressure is shown in Eq. (2.22), errors for other quantities, e.g., particle velocity, acoustic intensity, squared pressure and so forth, can also be calculated in a similar fashion.

Three specific examples will be discussed here to compare modal expansion results. In these examples, L, x_0, and f_0 are unchanged and have values of 2 m, 0.6 m and 500 Hz respectively. The specific acoustic impedance z of the duct ends, however, varies as shown in Table. 2.1. Damped duct 1 and 2 have the same normal-incidence absorption coefficient α_n but different phase angles for z.

Figure 2.1 compares coupled CMA and MMA. Both models work very well and converge to the exact solutions quickly. As the damping increases, especially when the phase angle of the specific acoustic impedance is greater than $\pi/4$, MMA starts to exhibit a notably faster convergence speed for sound pressure, and is thus more accurate with a smaller number of

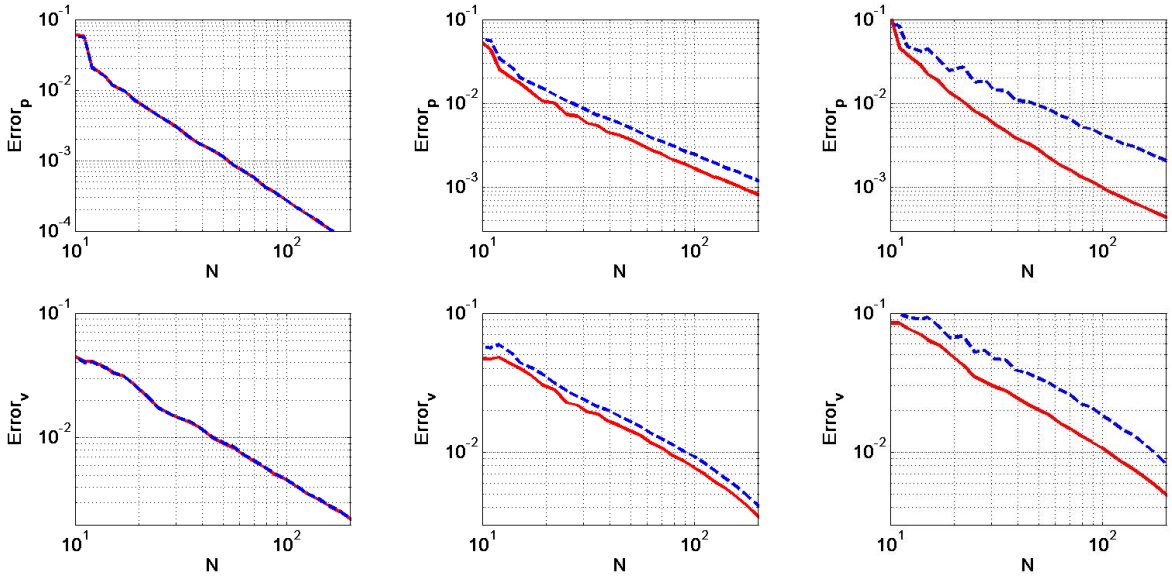

(a) Lightly damped duct. (b) Damped duct 1. (c) Damped duct 2.

Figure 2.1 Accuracy test for the coupled modal expansions in 1-D ducts at 500 Hz [(a) lightly damped duct, (b) damped duct 1, and (c) damped duct 2]. The errors in predicting the complex pressure field and the complex particle velocity field are plotted as functions of the number of modes. Equation (2.22) is evaluated, but regions within 0.1 m from the point source and 0.005 m from the boundaries are excluded when evaluating the integrals. "——": MMA; "– –": CMA.

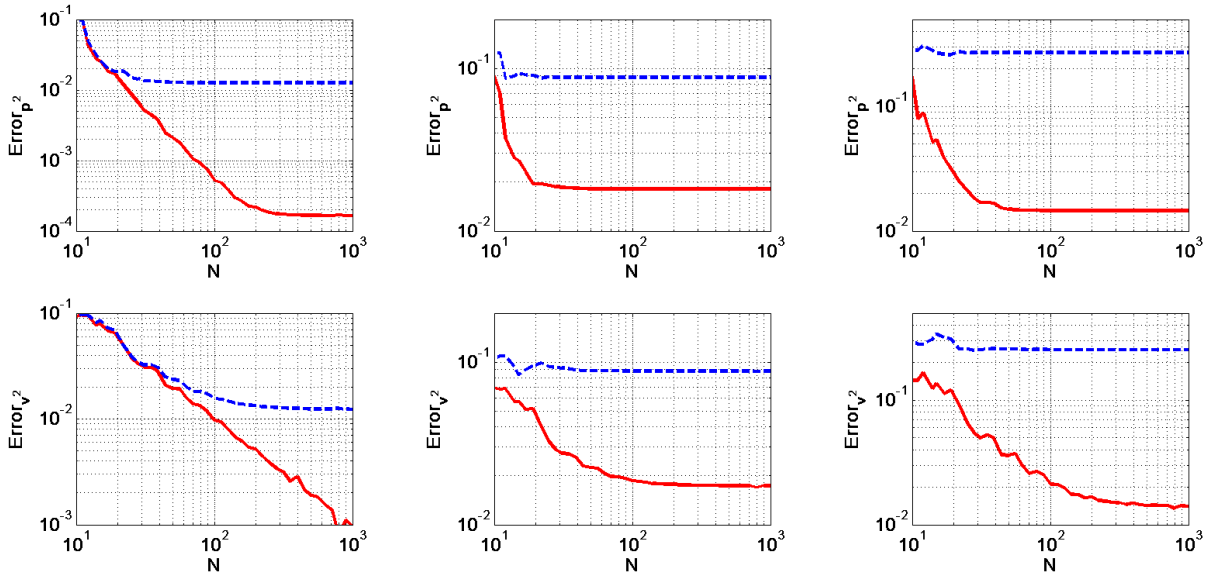

(a) Lightly damped duct. (b) Damped duct 1. (c) Damped duct 2.

Figure 2.2 Accuracy test for the "uncoupled" modal expansions in 1-D ducts at 500 Hz [(a) lightly damped duct, (b) damped duct 1, and (c) damped duct 2]. The errors in predicting the squared pressure field and the squared particle velocity field are plotted as functions of the number of modes. Equation (2.22) is evaluated, but regions within 0.1 m from the point source and 0.005 m from the boundaries are excluded when evaluating the integrals. "——": MMA; "– –": CMA.

modes. For particle velocity, MMA is only slightly better than CMA in terms of prediction errors. Additional studies show that the convergence speed of both MMA and CMA is slow at the source location. Moreover, errors cannot be eliminated for the particle velocity on the boundaries, but MMA has constantly much less error than CMA.

To compare the "uncoupled" models [the off diagonal terms of matrix A in Eq. (2.10) are simply set to zero], errors for squared moduli of pressure and squared particle velocity are computed instead of complex quantities because both models tend to introduce large errors in phase. As shown in Fig. 2.2, MMA is up to ten times more accurate than CMA for both squared quantities. It needs to be pointed out that, unlike the coupled models,

the "uncoupled" models do not converge to the exact solution even in terms of amplitude, but instead reach an error level that cannot be reduced with additional modes, although the error using MMA is likely to be acceptable on a logarithmic scale. Figure 2.3 compares the "uncoupled" model predictions for the sound pressure level and particle velocity level to the exact solutions. For the case of damped duct 2, errors introduced by "uncoupled" MMA are generally acceptably small (within 0.2 decibels except for the nodal points and source location) while large errors are observed with the "uncoupled" CMA. Although MMA dose not predict the correct value at nodal points, it does predict the locations of nodes correctly. Both "uncoupled" models, however, have large errors when computing the acoustic intensity (not shown here), which is the result of significant phase errors for both "uncoupled" models.

Finally, it is worthwhile to take a look at the values of β for the three boundary conditions and the corresponding values of β' used in MMA. At 500 Hz, β can be calculated using Eq. (2.3). The values are $-0.09 - 0.09i$, $0.61 - 0.89i$ and $-1.83 - 0.92i$ for the lightly damped duct, damped duct 1 and damped duct 2, respectively. MMA uses the real part of β for β' and CMA always uses zero. For the coupled models, both CMA and MMA perform well for the lightly damped duct because the value of β is small, which leads to a small difference between β and β' for both modal models. As the modulus of β increases, CMA tends to converge more slowly. The convergence rate of MMA, however, depends not only on the modulus of β but also on the phase. For example, β for the damped duct 2 is larger than that for the damped duct 1; therefore CMA performs worse for the damped duct 2. However, that is not the case for MMA, which is due to the fact that the real part of β is larger than the imaginary part for the damped duct 2, while the opposite is true for the damped duct 1. When it comes to the "uncoupled" models, a similar trend can be observed, except that the difference between MMA and CMA is more clear. Even for the lightly damped duct, there is a notable difference between the results of CMA and MMA.

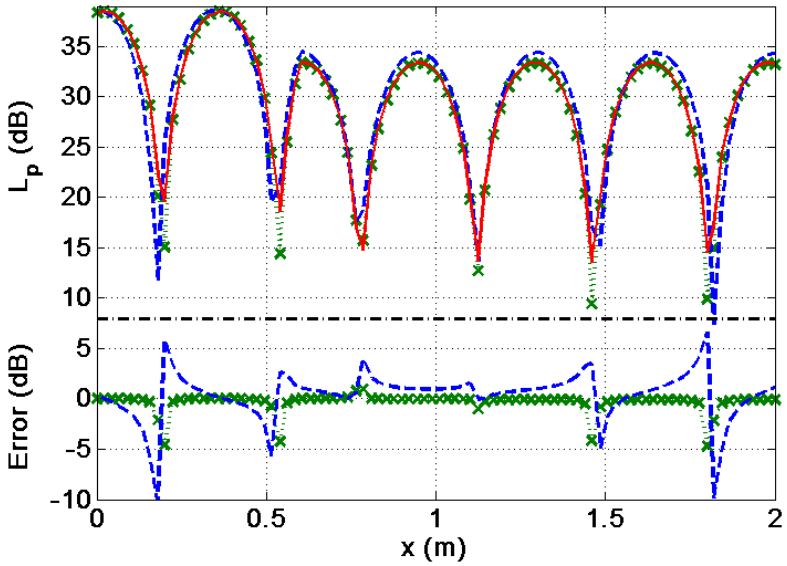

(a) Sound Pressure Level

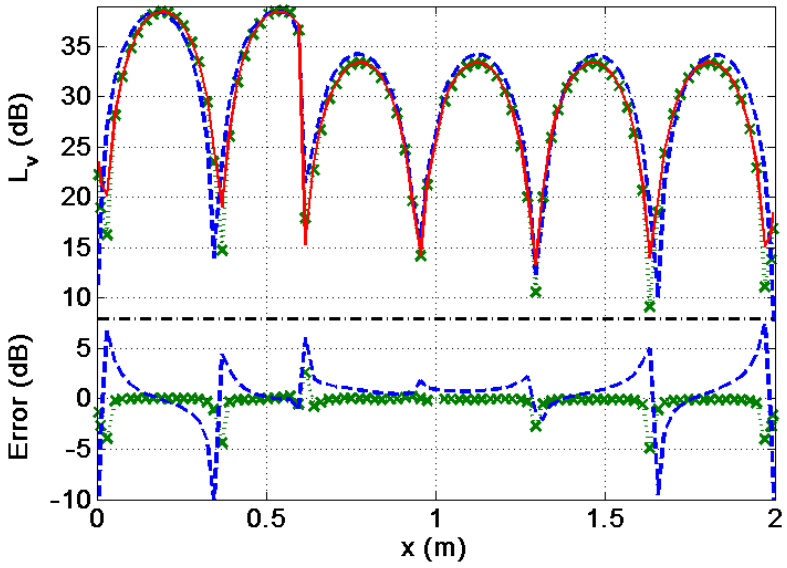

(b) Particle velocity Level

Figure 2.3 (a) Sound pressure level (re 20 μPa) and (b) particle velocity level (re 20 $\mu Pa/(\rho_0 c)$) computed by "uncoupled" modal expansion models compared with the exact solution at 500 Hz in the damped duct 2 ($z = 2 + 4i$). Here, 200 modes are included in each model. In each plot, curves above the dash dot line represent sound pressure level or particle velocity level. Curves below the dash dot line plot the differences between the sound levels computed by two modal models and the exact solutions. "——": exact solution; "·· × ··": MMA; "– –": CMA.

Table 2.2 Rectangular Enclosures Used for Convergence Test.

	$z/\rho_0 c$	α_s	Schroeder Frequency (Hz)
Lightly Damped	$200 + 340i$	0.01	1290
Damped Enclosure 1	$10 + 5.5i$	0.4	190
Damped Enclosure 2	$1 + 2.9i$	0.4	190

2.3.2 Comparisons in Three-Dimensional cases

For three-dimensional (3-D) enclosed sound fields, the closed form solution usually does not exist, so there is not a simple benchmark to compare with. However, since both classical modes and modified modes are complete and the coupled modal expansions should converge absolutely for the entire enclosed volume except at boundaries and source locations, a coupled modal expansion result can be accurate enough to be the benchmark if enough modes are included.

Convergence tests were carried out to compare four coupled models: CMA, MMA, GCMA and GMMA, where GCMA refers to the hybrid model using CMA and GMMA refers to the hybrid model using MMA. Sound fields in three different rectangular enclosures were computed and compared. The enclosures have the same dimensions ($2.7\ m \times 3.1\ m \times 2\ m$) but, as shown in Table 2.2, different specific impedances for the boundaries. A point source was randomly chosen to be located at ($1.09\ m, 1.20\ m, 0.7\ m$), and the driving frequency is 400 Hz.

Figure 2.4 compares the values of $\sum_{n=0}^{N} |q_n|^2$ and $\sum_{n=0}^{N} |q_n k_n|^2 / k_0^2$ that are computed from four "coupled" models. The hybrid models converge notably faster than pure modal models. MMA and GMMA converge faster than CMA and GCMA respectively. The difference in terms of the limit values between the hybrid model results and pure modal model results is due to the fact that hybrid models treat the direct sound field and reverberant field separately

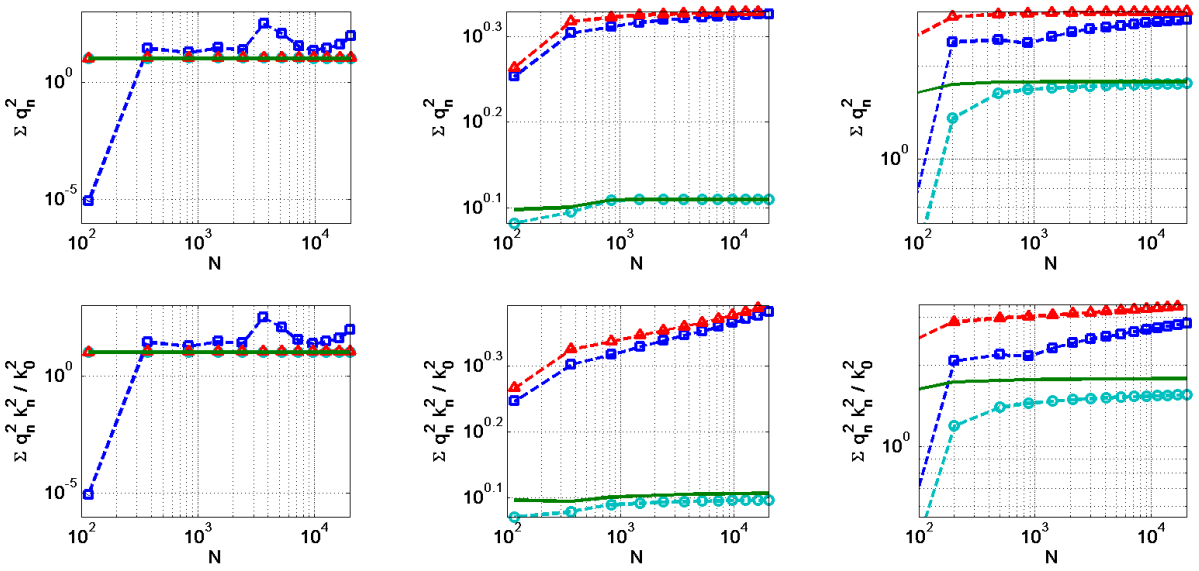

(a) Lightly damped enclosure. (b) Damped enclosure 1. (c) Damped enclosure 2.

Figure 2.4 Convergence speed of the coupled modal expansion models for enclosures with different boundary conditions [(a) lightly damped, (b) damped 1, and (c) damped 2] at 400 Hz. "–□–": CMA; "– ◯ –": GCMA; "– △ –": MMA; "——": GMMA.

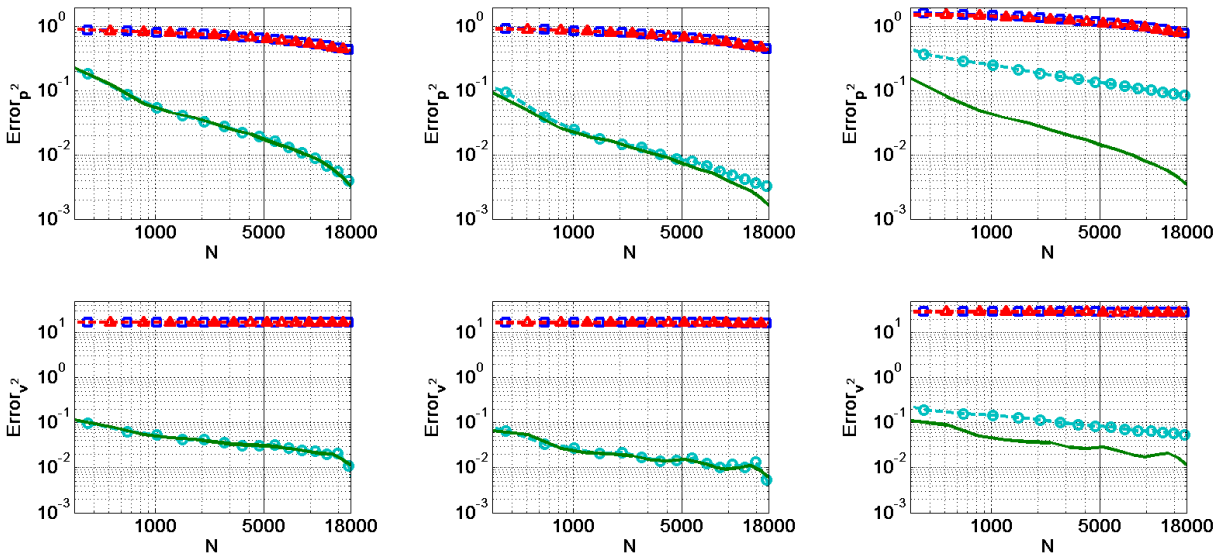

(a) Lightly damped. (b) Damped 1. (c) Damped 2.

Figure 2.5 Accuracy test for the coupled modal expansion models in enclosures [(a) lightly damped, (b) damped 1, and (c) damped 2] at 400 Hz. The errors in predicting the squared pressure field and the squared particle velocity field are plotted as functions of N, the number of modes. "–□–" : CMA; "– ◯ –": GCMA; "– △ –": MMA; "——": GMMA.

but the pure modal models consider them together.

Since the GMMA model shows the fastest convergence speed in all the cases, the results computed by this model (2×10^4 modes included) will be considered as the benchmarks to which other models can be compared. The errors of models can be calculated by Eq. (2.22) with $\hat{p}_{exact}$ being replaced by the benchmark value and the linear integrals being replaced by volume integrals that cover the whole interior of an enclosure. Figure 2.5 plots the errors for squared pressure and squared particle velocity versus the number of modes included in the coupled models. In general, the errors decrease as the number of modes increases for all the coupled models. However, the hybrid models converge much faster and thus have much less error than the pure modal models with a limited number of modes. In addition,

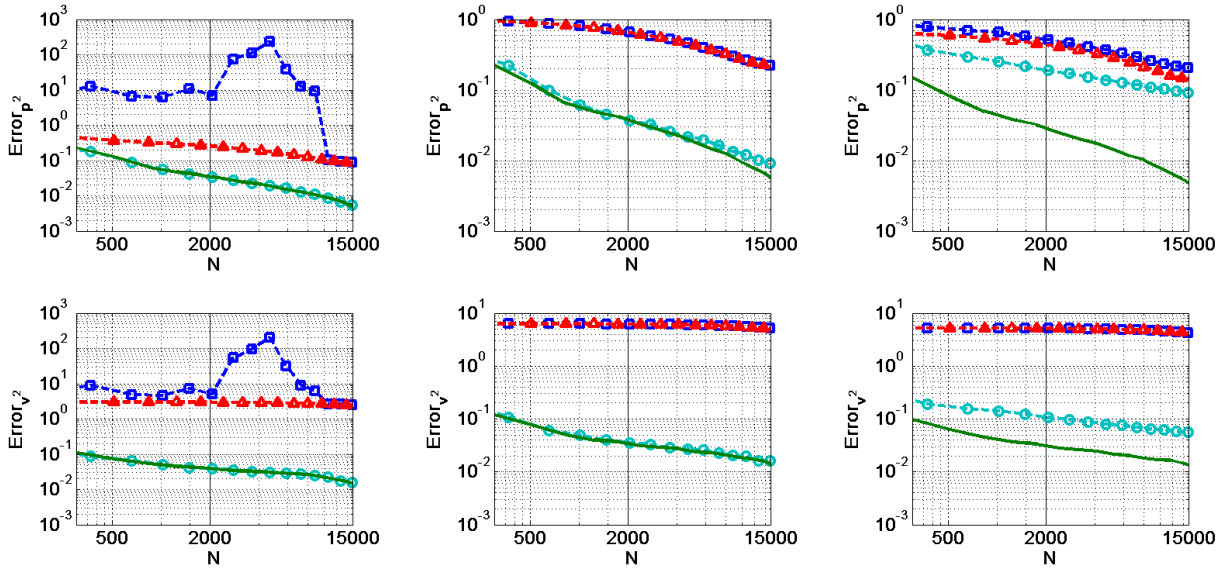

(a) Lightly damped. (b) Damped 1. (c) Damped 2.

Figure 2.6 Errors of the coupled models when the near-field region is excluded. The errors for the squared pressure field and the squared particle velocity field in three enclosures [(a) lightly damped, (b) damped 1, and (c) damped 2] are calculated as functions of the number of modes at 400 Hz. "–□–": CMA; "– ◯ –": GCMA; "– △ –": MMA; "——": GMMA.

GMMA shows obvious advantages over GCMA for the damped boundary conditions where the specific acoustic impedance of the boundary has a large phase angle.

The slow convergence speed of the pure modal models, especially for the particle velocity, is largely due to the singularity at the point source location. Averaged errors in the region that is at least 0.3 m away from the point source have also been computed. The convergence speed and accuracy of the pure modal models improve greatly, but are still notably worse than that of the hybrid models (Fig. 2.6).

Figure 2.7 compares the errors for the "uncoupled" models. Again the hybrid models work much better than the pure modal models. However, unlike the coupled models, "uncoupled" GMMA and GCMA reach an error level quickly and tend to stay at that level. Errors of

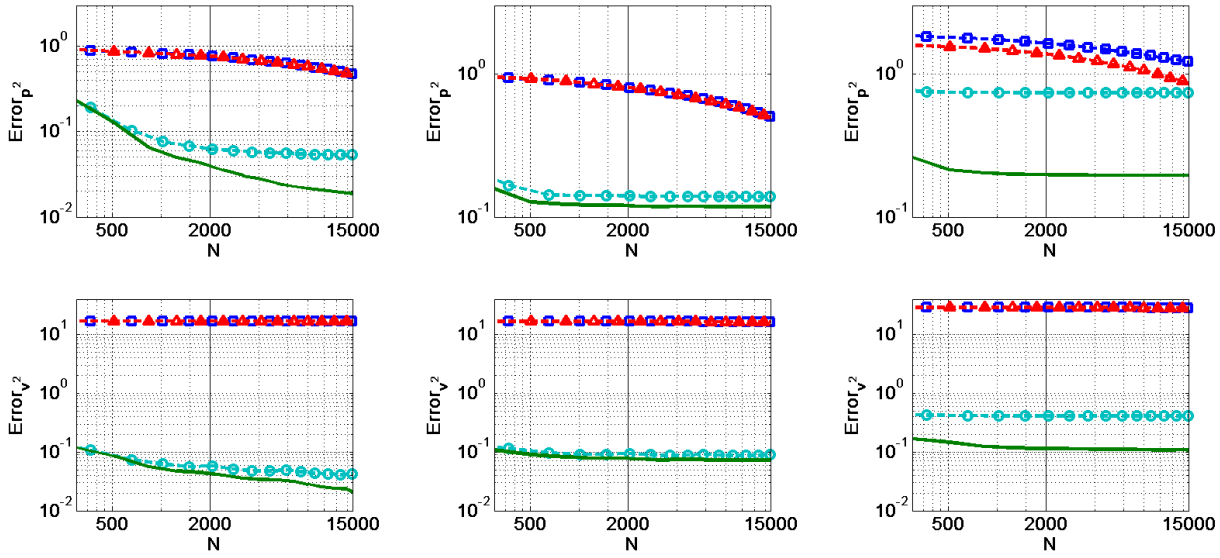

(a) Lightly damped. (b) Damped 1. (c) Damped 2.

Figure 2.7 Accuracy test for the "uncoupled" modal expansion models in enclosures [(a) lightly damped, (b) damped 1, and (c) damped 2] at 400 Hz. The errors in predicting the squared pressure field and the squared particle velocity field are plotted as functions of N, the number of modes. "–□–" : CMA; "–◯–": GCMA; "– △ –": MMA; "——": GMMA.

the pure modal models decrease very slowly as the number of modes increases. GMMA exhibits notably better accuracy than other models. For the damped enclosures ($\alpha_s = 0.4$), the averaged error is around 10 percent.

Above all, the coupled hybrid models converge notably faster and have much better accuracy than the other models when a limited number of modes are included. The difference between the GMMA and GCMA models can be either minor ("lightly damped" and "damped 1") or relatively large ("damped 2") depending on the boundary conditions, but given that GMMA usually requires more computational resources (CPU time and memory), GCMA is probably more desirable in practice. For "uncoupled" models, the pure modal models can introduce significant errors even if the enclosure is lightly damped, but the hybrid models can improve the accuracy greatly. Since there is no notable difference between "uncoupled" GMMA and GCMA in terms of computational resource requirements, GMMA is always preferred due to the better accuracy.

2.4 Examples of Using the Hybrid Modal Analysis

2.4.1 Sound Power

The sound power for a source inside an enclosure can be computed by integrating the acoustic intensity over a Gaussian surface inside the enclosure, where a Gaussian surface is defined as a closed three-dimensional surface through which a flux of the field is to be calculated. In this example, a rectangular enclosure [dimensions: 2.7 m $\times$ 3.1 m $\times$ 4 m, $z = (0.5 + 1i)\rho_0 c$, $\alpha_s = 0.76$] will be considered, and the point source arbitrarily located at (1.09 m, 1.04 m, 1.12 m) is driven at 495 Hz. The Gaussian surfaces are rectangular shapes with each side being parallel and equidistant, d, to the nearest boundary of the enclosure. Figure 2.8 compares the sound power results computed by the coupled GMMA and CMA methods (1400 modes

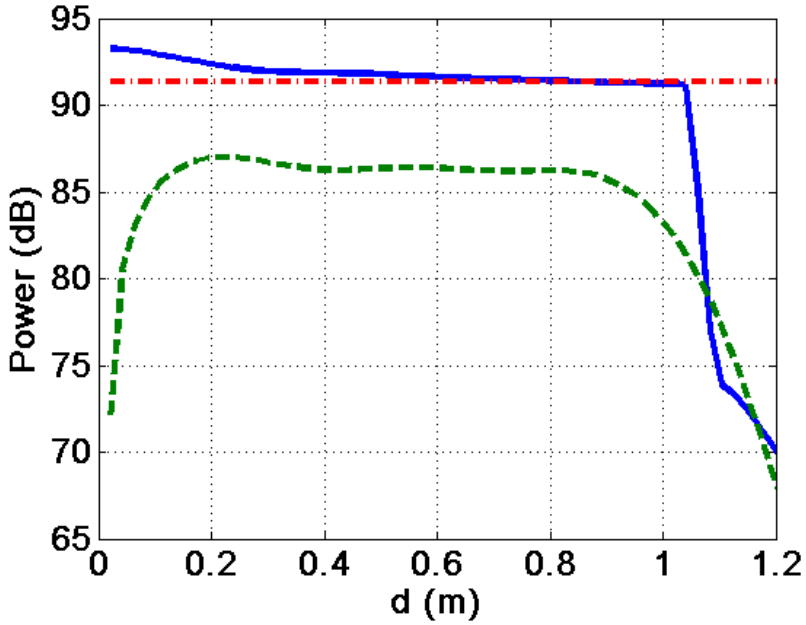

Figure 2.8 Sound power of an enclosed sound field computed by the coupled GMMA and CMA methods at 495 Hz. The enclosed sound field is excited by a pure-tone point source in a damped rectangular enclosure. The sound power results were obtained by integrating the acoustic intensity over multiple Gaussian surfaces which are rectangular shapes with each side being parallel and equal distance (d) to the nearest boundary of the enclosure. "——": GMMA prediction; "– –": CMA prediction; "– · –": free-field source power.

are used). The x axis represents the distance between the Gaussian surface and the enclosure boundary. When $d > 1.04$ the Gaussian surface begins to exclude the point source; therefore, the sound power is expected to be zero. GMMA captures this sharp change very well. In addition, since the driving frequency is above the Schroeder frequency of the enclosure (111 Hz), the sound power emitted from the point source in the enclosure should be approximately equal to its free-field power radiation. GMMA is able to predict the level of the sound power accurately everywhere while CMA fails.

2.4.2 Direct Field and Reverberant Field

The concepts of the direct field and the reverberant field have long been accepted by acousticians. An expression for the time-averaged sound pressure in terms of the direct sound pressure and the reverberant sound pressure has been obtained based on the energy diffusion equation as[47]

$$p^2 = \Pi \rho_0 c \left[\frac{1}{4\pi r_d^2} + \frac{4(1-\alpha_e)}{S\alpha_e} \right], \tag{2.23}$$

where Π is the source power, S is the inner surface area of the room, r_d represents the distance from the point source to the field point, and α_e is the effective absorption coefficient. The first term on the right hand side of Eq. (2.23) corresponds to the direct field and the second term corresponds to the reverberant field. The critical distance is defined as the distance from the source at which the direct sound pressure equals the reverberant sound pressure and can be computed by the following formula:

$$R_c = \sqrt{\frac{S\alpha_e}{16\pi(1-\alpha_e)}}. \tag{2.24}$$

There has been much discussion on how to best compute the effective absorption coefficient, α_e.[1,48–53] Here, the effective absorption coefficient of a room will be computed numerically based on GMMA and compared to the results of some existing formulas. The

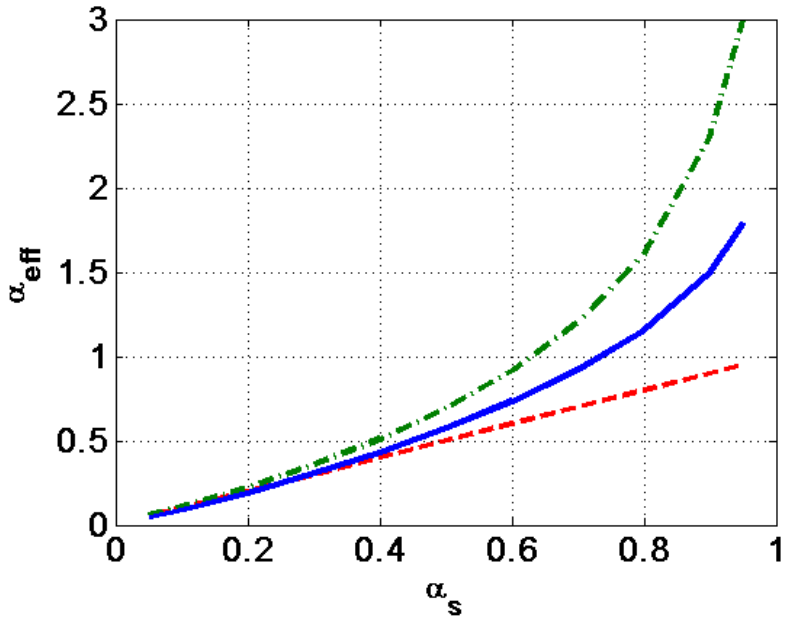

Figure 2.9 Effective absorption coefficient as a function of Sabine's absorption coefficient calculated in a rectangular room for the 630 Hz one-third octave band. "——": GMMA prediction; "– –": Sabine's formula; "– · –": Eyring's formula.

dimensions of the room under test are 3.9 m × 3.1 m × 5.0 m. The different boundary conditions are implemented and the Sabine absorption coefficient varies from 0.05 to 0.8. The Schroeder frequency for these conditions varies from 447 Hz to 100 Hz. Five frequencies in the 630 Hz one-third octave band were chosen to drive a point source. The sound fields are computed ten times at each frequency with the source location randomly chosen each time. The critical distances calculated directly from the direct field and reverberant field results are averaged and used to calculate the effective absorption coefficient using Eq. (2.24). Figure 2.9 compares the numerical results with Sabine's formula and Eyring's formula. The GMMA results (with around 1500 modes) generally fall between them, which is very similar to the results of Joyce[49] (see the curve "$s = 7/9$" in his Fig. 4) and Jing *et al.*[53]

2.4.3 Complex Sources

In practice, sound sources are often complex extended sources, rather than point sources (monopoles). For a distributed source placed inside an enclosure, computation may be very difficult and time consuming with pure modal models; however, a simple modification of the hybrid modal expansion method can solve this problem easily for cases where the size of the source is small compared to the dimensions of the enclosure. If, for example, the free-field directivity pattern, $D(r, \phi, \theta)$, of a distributed source is known, one can simply replace the free-field Green's function (G) in Eqs. 2.14 and 2.16 with $D(r, \phi, \theta)$ and compute the sound field without much additional computation required. Figure 2.10 compares the pressure fields of two different sources placed in the "Damped enclosure 2" (see Table 2.2) using the GMMA model with around 2000 modes. Two small sources are located at the center of the enclosure and both are driven at a frequency of 400 Hz. However, they have different free-field directivity patterns: (1) an omnidirectional source [$D(r, \phi, \theta) = 1$], (2) a complex source [$D(r, \phi, \theta) = \sqrt{2}\cos(\theta/2)$]. Pressure fields on the x-y, y-z and x-z planes that include the source are plotted. Effects of the source directivity are clearly represented by the GMMA model.

The closed form expression of the free-field response of a source is usually not available, but if the multipole expansion is known, the hybrid modal expansion can be certainly implemented straightforwardly and Eqs. 2.14 and 2.16 can be modified to

$$\hat{p}(\boldsymbol{r}) = \hat{p}_0 + F(\boldsymbol{r}), \tag{2.25}$$

and

$$\begin{aligned} \sum_n \left[\left(k_0^2 - k_m^2\right) C_{mn} + D_{mn} \right] q_n &= -\oint_S \psi_m^* \left(\beta \hat{p}_0 - \frac{\partial \hat{p}_0}{\partial \mathbf{n}} \right) da \\ &= -\sum_{m=1}^{M} A_m \oint_S \psi_m^* \left(\beta \Phi_m - \frac{\partial \Phi_m}{\partial \mathbf{n}} \right) da, \end{aligned} \tag{2.26}$$

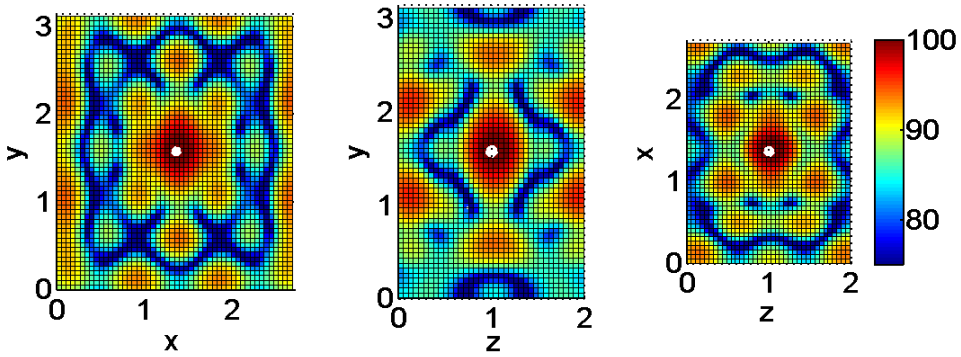

(a)

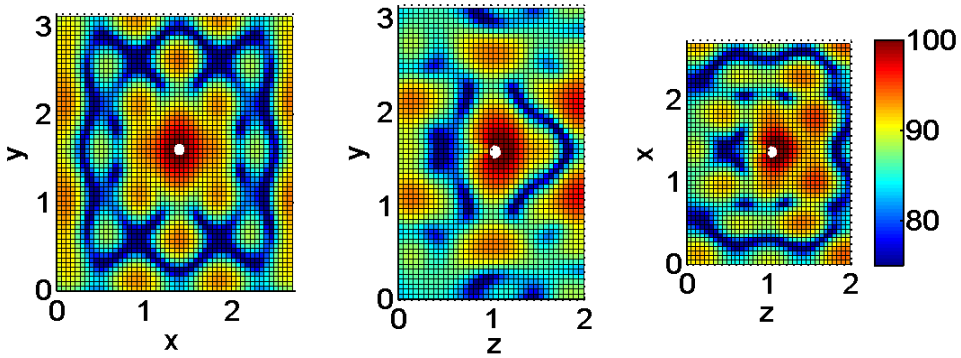

(b)

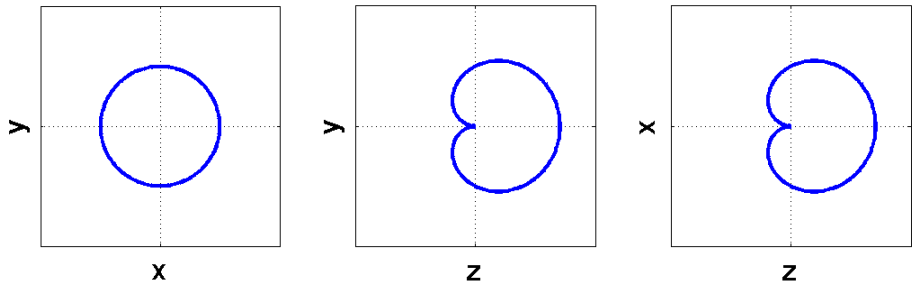

(c)

Figure 2.10 Sound pressure level computed by GMMA for (a) a monopole source and (b) a small complex source in a rectangular room (damped room 2) at 400 Hz. Both sources are placed at the center of the room. Pressure fields on the x-y, y-z and x-z planes that include the source are plotted with the white dots representing the location of the sources. The directivity pattern of the small complex source is shown in (c).

where $\hat{p}_0 = \sum_{m=1}^{M} A_m \Phi_m$, the multipole expansion for the free-field sound pressure of a complex source, and Φ_m represents the expression of the mth multipole and A_m stands for the amplitude of that multipole.

2.5 Conclusions

Different modal expansion methods have been studied here. A set of modified modes are introduced to deal with damped enclosures. A free-field Green's function is integrated to the solution of the inhomogeneous Helmholtz equation to improve both convergence rate and accuracy of modal expansions.

Like the normal modes, the modified modes are complete and orthogonal. For damped boundary conditions, the modified modes are mutually coupled, which causes the computation time to increase significantly, as is the case for the normal modes. However, by partially satisfying the boundary conditions, MMA not only performs better than CMA in the region near boundaries but also is more accurate globally with even fewer modes used. In addition, the "uncoupled" MMA can predict sound pressure level and particle velocity level fairly accurately for many damped boundary conditions, while the "uncoupled" CMA usually introduces large errors. Usually, MMA requires numerically searching for the eigenvalues. This process is fairly straightforward and fast. Utilizing the univariate interval Newton/generalized bisection method,[40] it took less than one second to calculate 20000 eigenvalues for any of the rooms listed in Table 2.2 on a computer with a 2.1 GHz CPU.

The enclosed sound field can be separated into the direct field and reverberant field, but these two are treated together in the traditional modal analysis. The weaknesses include slow convergence rate (especially in the near field of a point source) and difficulty in dealing with complicated sources inside an enclosure. The hybrid modal expansion introduced in this chapter successfully addresses these problems. Studies on a point source in rectangular

enclosures show that the hybrid modal expansions converge notably faster than the regular modal expansions and the hybrid "uncoupled" modal expansions introduce much smaller errors than the regular "uncoupled" expansions. The hybrid modal expansion can be easily applied to complex sound sources if the free-field responses of the sources are known.

Chapter 3

Generalized Energy Density

3.1 Introduction

This chapter will be organized as follows. The GED and some of its general properties will be introduced in Section 3.2. In Section 3.3, its behavior will be explored for room modes. Its properties in a diffuse field will be investigated in Section 3.4, with a focus on single-tone excitation, and some characteristics of narrow-band excitation. In Section 3.5, its spatial variance will be studied for frequencies below the Schroeder frequency of a room. Computer simulation results will be presented in Section 5.5 to validate some of the GED properties introduced in the chapter.

3.2 Generalized Energy Density

The total acoustic energy density is defined as the acoustic energy per unit volume at a point in a sound field. The time-averaged total acoustic energy density can be expressed in the

frequency domain as

$$\begin{aligned} E_T &= E_P + E_K \\ &= \frac{1}{2}\frac{\hat{p}\hat{p}^*}{\rho_0 c^2} + \frac{1}{2}\rho_0 \hat{\mathbf{u}} \cdot \hat{\mathbf{u}}^*, \end{aligned} \tag{3.1}$$

where $\hat{p}$ and $\hat{\mathbf{u}}$ represent the complex acoustic pressure and particle velocity respectively in the frequency domain, ρ_0 is the ambient fluid density, and c is the speed of sound. On the right-hand side of this expression, the first term represents the time-averaged potential energy density (E_P) and the second term represents the time-averaged kinetic energy density (E_K). The time-averaged kinetic energy density can be written as the sum of three orthogonal components as

$$\begin{aligned} E_K &= E_{Kx} + E_{Ky} + E_{Kz} \\ &= \frac{1}{2}\rho_0 \hat{u}_x \hat{u}_x^* + \frac{1}{2}\rho_0 \hat{u}_y \hat{u}_y^* + \frac{1}{2}\rho_0 \hat{u}_z \hat{u}_z^*. \end{aligned} \tag{3.2}$$

The Generalized Energy Density (GED) is defined as follows:

$$E_{G(\alpha)} = \alpha E_P + (1-\alpha) E_K, \tag{3.3}$$

where α is a real variable. By forcing the sum of the weighting factors of E_P and E_K to be one, one can cause the GED to represent the traditional energy density quantities by introducing only one additional degree of freedom. In other words, $E_P = E_{G(1)}$, $E_K = E_{G(0)}$ and $E_T = 2E_{G(1/2)}$. Although, in theory, α could be any real number, the range of zero to one is mainly focused on here because it turns out to be the range that contains all the special values of α that make GED favorable for the applications studied in this dissertation. The theoretical derivations presented in this dissertation, however, are general enough so that the results can be implemented directly to the entire domain of real numbers.

The spatial mean of GED for a sound field can be calculated as

$$\begin{aligned} \mu_G = E[E_G] &= E[\alpha E_P + (1-\alpha)E_K] \\ &= \alpha\mu_P + (1-\alpha)\mu_K \end{aligned} \tag{3.4}$$

where $E[\cdot]$ represents the expectation operator and μ_G, μ_P, and μ_K represent the spatial mean value of E_G, E_P, and E_K, respectively. Given that $\mu_P = \mu_K$ for most enclosed sound fields, one can conclude from Eq. (3.4) that μ_G does not vary due to α, and $\mu_G = \mu_P = \mu_K$, which is another major benefit of defining GED as given in Eq. 3.3.

The relative spatial variance of GED can similarly be calculated as

$$\begin{aligned} \epsilon_G^2 &= \frac{\sigma^2\left[E_G\right]}{E^2\left[E_G\right]} = \frac{E[E_G^2] - E^2[E_G]}{E^2[E_G]} \\ &= \frac{\alpha^2 E[E_P^2] + 2\alpha(1-\alpha)E[E_P E_K] + (1-\alpha)^2 E[E_K^2] - \mu_G^2}{\mu_G^2} \\ &= \frac{\alpha^2(E[E_P^2] - \mu_P^2)}{\mu_P^2} + \frac{(1-\alpha)^2(E[E_K^2] - \mu_K^2)}{\mu_K^2} + \frac{2\alpha(1-\alpha)(E[E_P E_K] - \mu_P\mu_K)}{\mu_P\mu_K} \\ &= \alpha^2\epsilon_P^2 + (1-\alpha)^2\epsilon_K^2 + 2\alpha(1-\alpha)\epsilon_{PK}^2 \qquad (3.5a) \\ &= \alpha^2(\epsilon_P^2 + \epsilon_K^2 - 2\epsilon_{PK}^2) + 2\alpha(\epsilon_{PK}^2 - \epsilon_K^2) + \epsilon_K^2 \qquad (3.5b) \end{aligned}$$

where $\sigma^2\left[\cdot\right]$ represents the spatial variance, ϵ_G^2, ϵ_P^2, and ϵ_K^2 represent the relative spatial variances of E_G, E_P, and E_K respectively, and ϵ_{PK}^2 stands for the relative spatial co-variance of E_P and E_K. In the derivation of the equations above, the relations of $\mu_G = \alpha\mu_P + (1-\alpha)\mu_K$ and $\mu_G = \mu_P = \mu_K$ are utilized. Equation (3.5b) shows that the relative variance of GED is a quadratic function of α. In addition, recognizing that $\epsilon_P^2 + \epsilon_K^2 > 2\epsilon_{PK}^2$, one can conclude that ϵ_G^2 has a global minimum,

$$min\{\epsilon_G^2\} = \frac{\epsilon_P^2\epsilon_K^2 - \epsilon_{PK}^4}{(\epsilon_P^2 + \epsilon_K^2 - 2\epsilon_{PK}^2)}, \tag{3.6}$$

when

$$\alpha = \frac{(\epsilon_K^2 - \epsilon_{PK}^2)}{(\epsilon_P^2 + \epsilon_K^2 - 2\epsilon_{PK}^2)}. \tag{3.7}$$

In the future discussion, it will be shown that the kinetic energy density and total energy density may not be the most spatially uniform quantities.

3.3 Modal Analysis

Below the Schroeder frequency, room modes often dominate the reverberant sound field. For a hard-walled rectangular room with dimensions $L_x \times L_y \times L_z$, if a single mode dominates the response at a resonance frequency, ignoring any constants, E_P and E_K can be expressed approximately as

$$E_P = cos^2(k_x x)cos^2(k_y y)cos^2(k_z z), \tag{3.8a}$$

$$\begin{aligned} E_K = & \frac{k_x^2 sin^2(k_x x)cos^2(k_y y)cos^2(k_z z)}{k^2} \\ & + \frac{k_y^2 cos^2(k_x x)sin^2(k_y y)cos^2(k_z z)}{k^2} \\ & + \frac{k_z^2 cos^2(k_x x)cos^2(k_y y)sin^2(k_z z)}{k^2}, \end{aligned} \tag{3.8b}$$

where k_x, k_y and k_z are eigenvalues and $k^2 = k_x^2 + k_y^2 + k_z^2$.

For an axial mode, where two of the three eigenvalues vanish (assumed here in the y- and z- directions)

$$\begin{aligned} E_G &= \alpha cos^2(kx) + (1-\alpha)sin^2(kx), \\ \epsilon_G^2 &= \frac{1}{2}(2\alpha - 1)^2. \end{aligned} \tag{3.9}$$

With no surprise, the relative variance reaches its minimum value of zero when $\alpha = 1/2$. This is because the total acoustic energy density is uniform for an axial mode.

For a tangential mode (only one eigenvalue equals zero), the expression for the relative variance is not as simple as that for an axial mode. It depends on both α and the ratio $\gamma = k_y/k_x$ (assuming $k_z = 0$), as shown in Table 3.1. Some examples of the spatial variance

Table 3.1 Relative Variance of Single Modes.

Mode	Mean	ϵ_P^2	ϵ_G^2
Axial	1/2	1/2	$\frac{(2\alpha-1)^2}{2}$
Tangential	1/4	5/4	$\frac{5-6\gamma^2+5\gamma^4-4\left(3-2\gamma^2+3\gamma^4\right)\alpha+4\left(3+2\gamma^2+3\gamma^4\right)\alpha^2}{4(1+\gamma^2)^2}$
Oblique	1/8	19/8	$\frac{19-10\gamma_{xy}^2(1+\gamma_{yz}^2)+\gamma_{xy}^4(19-10\gamma_{yz}^2+19\gamma_{yz}^4)}{8\left(1+\gamma_{xy}^2+\gamma_{xy}^2r_2^2\right)^2}$ $-\frac{[3-2\gamma_{xy}^2(1+\gamma_{yz}^2)+\gamma_{xy}^4(3-2\gamma_{yz}^2+3\gamma_{yz}^4)]\alpha}{2\left(1+\gamma_{xy}^2+\gamma_{xy}^2r_2^2\right)^2}$ $+\frac{[3+2\gamma_{xy}^2(1+\gamma_{yz}^2)+\gamma_{xy}^4(3+2\gamma_{yz}^2+3\gamma_{yz}^4)]\alpha^2}{2\left(1+\gamma_{xy}^2+\gamma_{xy}^2r_2^2\right)^2}$

for different γ values are shown in Fig. 3.1 (a). By assuming $k_x \leq k_y$, it is not hard to prove that ϵ_G^2 increases with γ for all α values less than one, and as γ tends to infinity, ϵ_G^2 converges to

$$\epsilon_G^2\big|_{\gamma\to\infty} = \frac{5}{4} - 3\alpha + 3\alpha^2. \tag{3.10}$$

The optimized value of α, which minimizes the relative variance, ranges between 1/4, when $\gamma = 1$ and 1/2, when $\gamma \to \infty$. With the optimal α value, the relative variance can become a tenth that of E_P and half that of E_T.

For an oblique mode, the relative variance depends on α as well as all the eigenvalues. With ratios $\gamma_{xy} = k_y/k_x$ and $\gamma_{yz} = k_z/k_y$, one can derive the expression for ϵ_G^2 shown in Table 3.1. When γ_{xy} approaches infinity while γ_{yz} remains finite, the behavior of ϵ_G^2 is very similar to that of the tangential modes. As a limiting case, when $\gamma_{xy} \to \infty$ and $\gamma_{yz} = 1$, ϵ_G^2 converges to

$$\epsilon_G^2\big|_{\gamma_{xy}\to\infty,\gamma_{yz}=1} = \frac{7}{8} - \frac{3\alpha}{2} + 3\alpha^2, \tag{3.11}$$

which is very similar to the tangential mode with $\gamma = 1$, and the optimal α value is also 1/4. As the value γ_{yz} approaches infinity, ϵ_G^2 converges to

$$\epsilon_G^2\big|_{\gamma_{yz}\to\infty} = \frac{19}{8} - \frac{9\alpha}{2} + \frac{9\alpha^2}{2}, \tag{3.12}$$

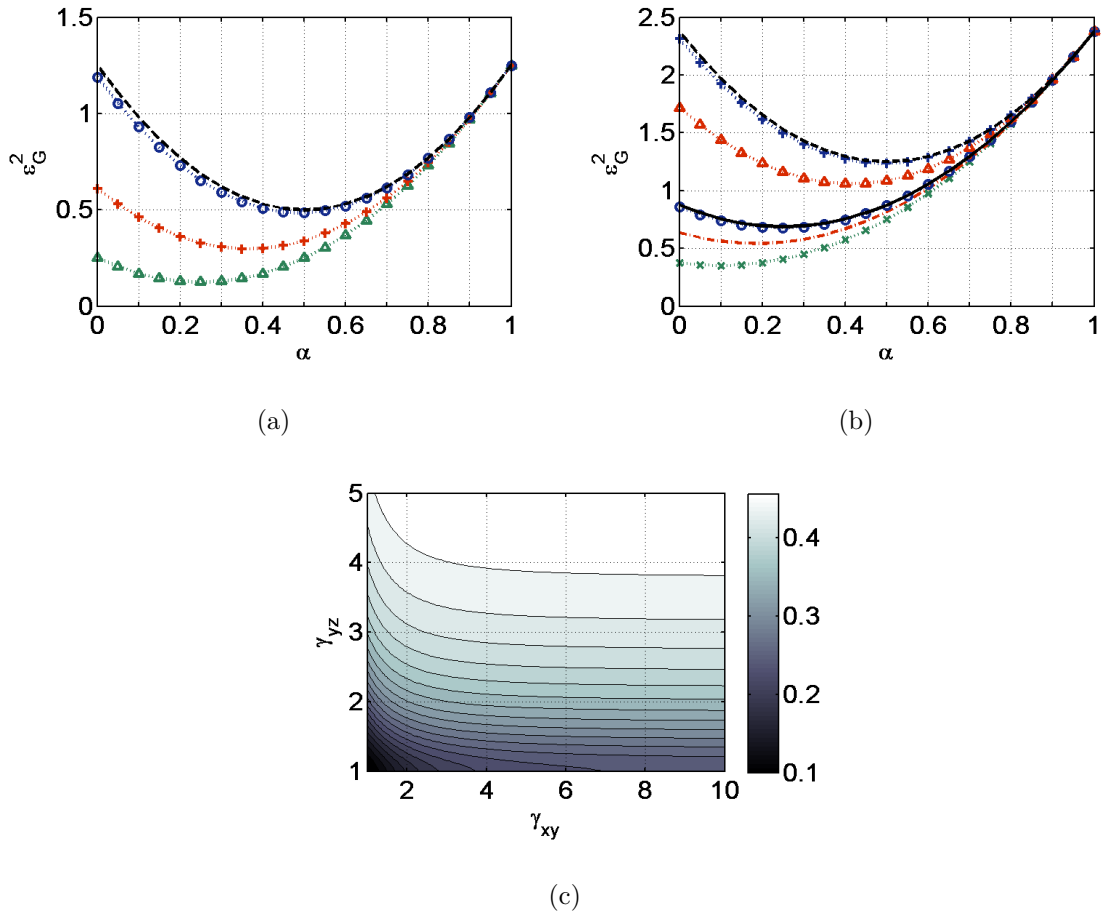

Figure 3.1 Relative spatial variance of GED for (a) a tangential mode, and (b) an oblique mode. The contour plot(c) shows the optimal values of α^2 that minimize ϵ_G for the oblique modes. In (a), "· · △ · ·": $\gamma = 1$; "· · + · ·": $\gamma = 2$; "· · ◯ · ·": $\gamma = 8$; "——": $\gamma \to \infty$ [Eq. (3.10)]. In (b), "· · × · ·": $\gamma_{xy} = 1.0, \gamma_{yz} = 1.0$; "— · —": $\gamma_{xy} = 1.2, \gamma_{yz} = 1.5$; "· · ◯ · ·": $\gamma_{xy} = 9.0, \gamma_{yz} = 1.0$; "· · △ · ·": $\gamma_{xy} = 2.0, \gamma_{yz} = 3.0$; "· · + · ·": $\gamma_{xy} = 9.0, \gamma_{yz} = 9.0$; "——": $\gamma_{xy} \to \infty$, $\gamma_{yz} = 1$ [Eq. (3.11)]; "——": $\gamma_{xy} \to \infty$, $\gamma_{yz} \to \infty$ [Eq. (3.12)].

.

regardless of the value of γ_{xy} [see Fig. 3.1(b)]. The optimal α value varies from 1/10 to 1/2 depending on the values of γ_{xy} and γ_{yz}. However, as can be observed from Fig. 3.1(c), if $\gamma_{yz} < 2$ the optimal α value is generally in the range of 0.1 to 0.35. With the optimal α value, the relative variance can become a factor of 6.8 smaller than that of E_P and half that of E_T. It is interesting to note that for all possible values of γ, γ_{xy} and γ_{yz}, E_P has the highest relative variance, which is a constant for each type of mode.

3.4 GED in Diffuse Fields

The free-wave model[5] has been successfully used to study the statistical properties of diffuse sound fields. It assumes that the sound field at any arbitrary point is composed of a large number of plane waves with random phases and directions. For a single-tone field, the complex acoustic pressure amplitude for a given frequency can thus be written as

$$\hat{p} = \sum_m A_m e^{i(k\mathbf{n}_m \cdot \mathbf{r} + \phi_m)}, \tag{3.13}$$

where A_m is a random real number representing the peak amplitude of the mth wave, and the unit vector $\mathbf{n}_m$ and phase ϕ_m are uniformly distributed in their spans.

It can be shown, based on the central limit theorem, that the rms value of squared pressure has an exponential distribution,[5,10] and the probability density function (PDF) of E_p is

$$f_{E_P}(x) = \frac{1}{\mu_G} e^{-x/\mu_G};\ x \geq 0. \tag{3.14}$$

The mean and variance are μ_G and μ_G^2, respectively, for the exponentially distributed E_P, so the relative variance is one.

Using a similar argument, Jacobsen was able to show that the three components of kinetic energy density (E_{Kx}, E_{Ky} and E_{Kz}) are independent and follow an exponential distribution.

Therefore, the kinetic energy density is distributed as a gamma distribution.[10] Thus, E_K is distributed as $Gamma(3, \mu_G/3)$, and the PDF is

$$f_{E_K}(x) = \frac{27x^2 e^{-3x/\mu_G}}{2\mu_G^3};\ x > 0. \tag{3.15}$$

The mean and variance for this distribution are μ_G and $\mu_G^2/3$ respectively, and the relative variance is 1/3, which is significantly less than that of the potential energy density.

Because E_P and E_K are independent,[10] one can compute the cumulative distribution function (CDF) and PDF for the GED with the following equations:

$$F_{E_G}(x) = \int_0^{\frac{x}{\alpha}} f_{E_P}(y) \int_0^{\frac{x-\alpha y}{1-\alpha}} f_{E_K}(z)\, dz\, dy, \tag{3.16}$$

$$f_{E_G}(x) = \frac{dF_{E_G}(x)}{dx}. \tag{3.17}$$

The calculation is rather involved, so only the final result for the PDF will be shown here:

$$f_{E_G}(x) = \frac{27\alpha^2 \left(e^{\frac{-3x}{\mu_G(1-\alpha)}} - e^{\frac{-x}{\mu_G\alpha}}\right)}{\mu_G(1-4\alpha)^3} + \frac{27x\left[x(1-4\alpha) - 2\mu_G\alpha(1-\alpha)\right] e^{\frac{-3x}{\mu_G(1-\alpha)}}}{2\mu_G^3(1-\alpha)^2(1-4\alpha)^2}. \tag{3.18}$$

With the use of Eq. (3.18) [or Eq. (3.5a)], one can obtain the relative spatial variance

$$\epsilon_G^2 = \frac{1}{3}(4\alpha^2 - 2\alpha + 1), \tag{3.19}$$

as plotted in Fig. 3.2. The minimum relative variance is 1/4 when $\alpha = 1/4$. At this optimal α value, the distribution of the GED turns out to be simply $Gamma(4, \mu_G/4)$, which should not be surprising if it is rewritten as

$$\begin{aligned} E_{G(1/4)} &= \frac{1}{4}E_P + \frac{3}{4}E_K \\ &= \frac{1}{4}E_P + \frac{3}{4}(E_{Kx} + E_{Ky} + E_{Kz}) \\ &= \frac{3}{4}(E_P/3 + E_{Kx} + E_{Ky} + E_{Kz}), \end{aligned} \tag{3.20}$$

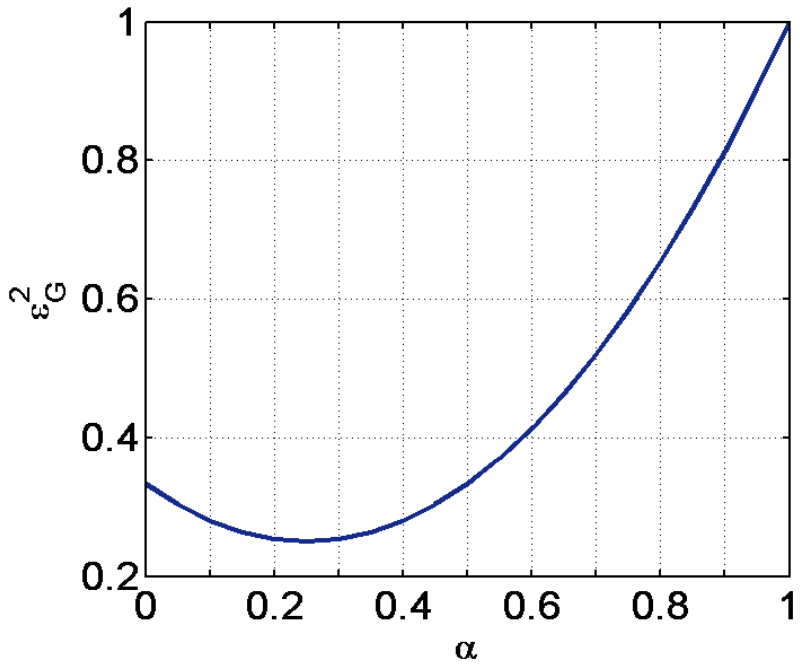

Figure 3.2 Relative spatial variance of GED in a diffuse field. The minimum variance is reached at $\alpha = 1/4$.

which is essentially the sum of four independent $Gamma(1, \mu_G/3)$ random variables multiplied by a shape factor of 3/4.

For narrow-band excitation, the relative spatial variance of the GED is approximately equal to the relative spatial variance for the single-tone excitation multiplied by $(1 + BT_{60}/6.9)^{-1}$, where B is the bandwidth and T_{60} represents the reverberation time.[54]

The spatial correlation between pressures at two separated field points in a single-tone diffuse field was first studied by Cook and Waterhouse.[55] At any arbitrary time t, the spatial correlation coefficient between $p_1 = p(\mathbf{r}_1, t)$ and $p_2 = p(\mathbf{r}_2, t)$ can be calculated as

$$\begin{aligned} \rho_p(r) &= \frac{Cov\left[p_1, p_2\right]}{\sigma[p_1]\sigma[p_2]} \\ &= \frac{sin(kr)}{kr}, \end{aligned} \tag{3.21}$$

where $\sigma[\cdot]$ represents standard deviation, k is the wave number, and $r = |\mathbf{r}_2 - \mathbf{r}_1|$. Lubman[56] obtained a formula for the squared pressures and E_P:

$$\rho_{E_P} = \rho_{p^2} = \left[\frac{sin(kr)}{kr}\right]^2. \tag{3.22}$$

Jacobsen[10] later derived the formulae for squared particle velocity components, as well as squared velocity and squared pressure. These formulae can be applied to E_K and E_P directly as

$$\begin{aligned} \rho_{E_K} &= \rho_{u^2} \\ &= \frac{3\left(6 + 2k^2r^2 + k^4r^4\right)}{2k^6r^6} \\ &\quad + \frac{3\left[4kr\left(-3 + k^2r^2\right)\sin(2kr) - \left(6 - 10k^2r^2 + k^4r^4\right)\cos(2kr)\right]}{2k^6r^6}, \end{aligned} \tag{3.23}$$

$$\rho_{E_P,E_K} = \rho_{p^2,u^2} = \sqrt{3}\left[\frac{\sin(kr) - kr\cos(kr)}{(kr)^2}\right]^2. \tag{3.24}$$

The spatial correlation coefficient for the GED at two field points can then be calculated as

$$\rho_{E_G} = \frac{1}{\epsilon_G^2}\left[\alpha^2\epsilon_P^2\rho_{E_P} + \alpha(1-\alpha)\epsilon_P\epsilon_K\rho_{E_P,E_K} + (1-\alpha)^2\epsilon_K^2\rho_{E_K}\right], \tag{3.25}$$

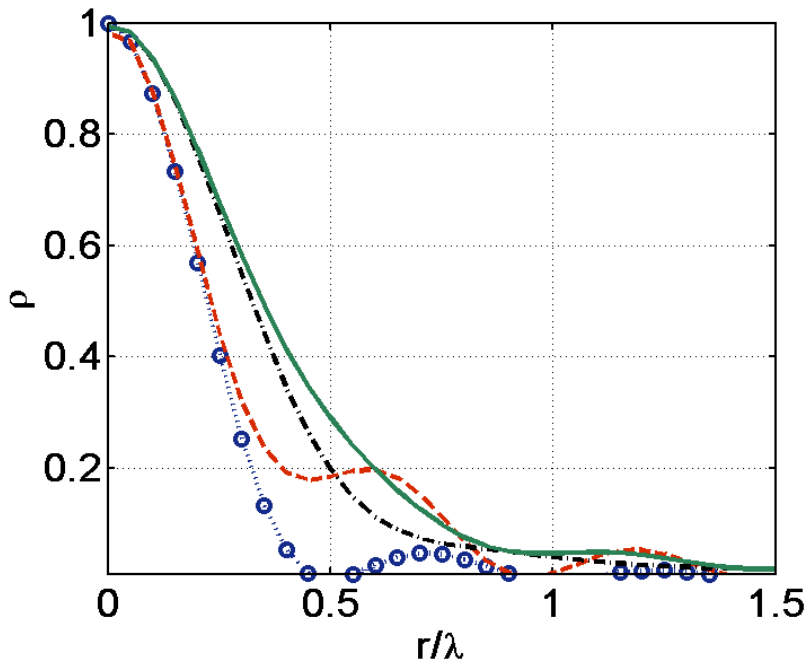

Figure 3.3 Spatial correlation coefficient ρ of different GED quantities in a diffuse field. "· · ◯ · ·": $E_{G(1)}$ (E_P); "– –": $E_{G(0)}$ (E_K); "–·–": $E_{G(1/2)}$ (E_T); "——": $E_{G(1/4)}$.

where $\epsilon_P^2 = 1$ and $\epsilon_K^2 = 1/3$, as indicated earlier. Note that ρ_{E_G}, as ρ_{E_P} and ρ_{E_K}, is also a function of r, although it is not shown explicitly in Eq. (3.25). There is not a concise expression for ρ_{E_G}, and some examples for different values of α are plotted in Fig. 3.3. It is well accepted that the spatial correlation can be neglected for the potential energy density if the distance between two field points is greater than half a wavelength (0.5λ).[10] In order to achieve a similarly low level of correlation (roughly $\rho \leq 0.05$), the separation distance needs to be greater than approximately 0.8λ for E_K, E_T and $E_{G(1/4)}$, which may not be favorable for some applications, such as sound power measurement in a reverberant chamber, because statistically independent sampling is required. It is, in some sense, a trade off for achieving better uniformity. However, for other applications, i.e., active noise control in diffuse fields,[57] a slowly decaying spatial correlation function may be beneficial.

As one approaches the regions close to boundaries, it is hard to claim a truly diffuse field even if the frequency is well above the Schroeder frequency in a reverberation chamber. Because of the strong reflections, one would expect some kind of interference effects. Waterhouse obtained expressions for the mean-squared pressure, mean-squared velocity and mean total energy density as functions of the distance from the boundaries.[58] His results can be directly applied to E_P and E_K. For a sound field close to a flat rigid boundary, one has

$$\langle E_P \rangle / \mu_G = 1 + \frac{\sin(2kx)}{2kx}, \tag{3.26}$$

$$\langle E_K \rangle / \mu_G = 1 - \frac{\sin(2kx)}{2kx} + \frac{\sin(2kx) - 2kx\cos(2kx)}{2(kx)^3}, \tag{3.27}$$

and thus,

$$\begin{aligned} \langle E_G \rangle / \mu_G &= \langle \alpha E_P + (1-\alpha) E_K \rangle / \mu_G \\ &= \alpha \left[1 + \frac{\sin(2kx)}{2kx} \right] + (1-\alpha) \left[1 - \frac{\sin(2kx)}{2kx} + \frac{\sin(2kx) - 2kx\cos(2kx)}{2(kx)^3} \right] \\ &= 1 + \frac{2kx(-1+\alpha)\cos(2kx) + [1 - \alpha - k^2x^2(1-2\alpha)]\sin(2kx)}{2k^3x^3}, \end{aligned} \tag{3.28}$$

where x represents the distance from the boundary, $< \cdot >$ represents a spatial average on the surface that is x away from the boundary and μ_G refers to the mean of GED in the region that is far away from all boundaries. As shown in Fig. 3.4, all the GED quantities have higher mean values at the boundary, and as the distance increases, the mean values converge to μ_G fairly quickly after half a wave length.

Jacobsen re-derived these results from the stochastic perspective, and found that both the potential energy density and all the components of kinetic energy density (either perpendicular or parallel to the boundary) near a boundary are independently distributed with the exponential distribution.[10] Therefore, the relative variance of GED near a boundary can be shown to be

$$\epsilon^2_{E_G}(x) = \frac{\alpha^2 \sigma^2_{E_P}(x) + (1-\alpha)^2 \sigma^2_{E_K}(x)}{\langle E_G \rangle^2}, \tag{3.29}$$

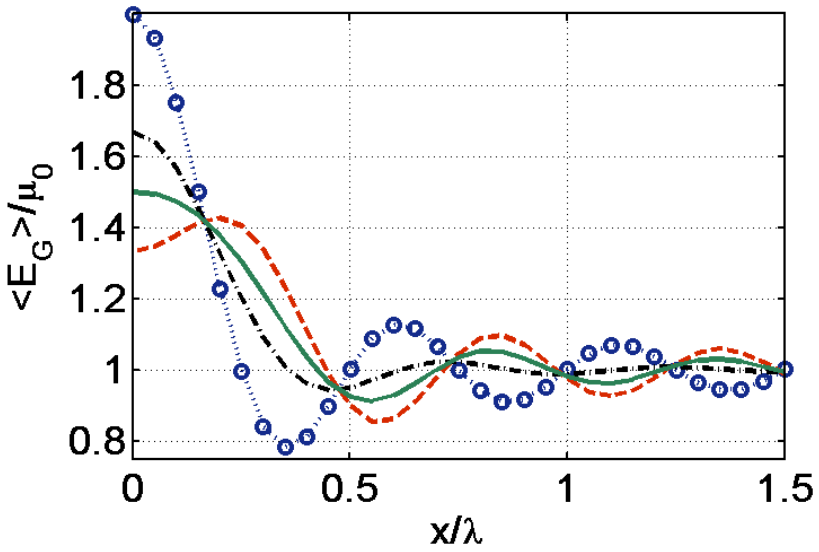

Figure 3.4 Mean values of different GED quantities as a function of the distance, x, from a flat rigid boundary in a diffuse field. "··◯··": $E_{G(1)}$ (E_P); "– –": $E_{G(0)}$ (E_K); "–·–": $E_{G(1/2)}$ (E_T); "——": $E_{G(1/4)}$.

where

$$\sigma^2_{E_P}(x) = \langle E_P \rangle^2 , \tag{3.30}$$

$$\begin{aligned} \sigma^2_{E_K}(x) &= \langle E_{K_\perp} \rangle^2 + 2 \left\langle E_{K_\parallel} \right\rangle^2 \\ &= \left[\frac{1}{3} + \frac{-2kx\cos(2kx) + \sin(2kx)}{8k^3x^3} \right]^2 \\ &\quad + \left[\frac{1}{3} - \frac{4kx\cos(2kx) - 2\sin(2kx) + 4k^2x^2\sin(2kx)}{8k^3x^3} \right]^2 , \end{aligned} \tag{3.31}$$

where $E_{K_\perp}$ represents the component of E_K that is perpendicular to the boundary, and $E_{K_\parallel}$ represents the component that is parallel to the boundary.[10] Right next to the boundary ($x \to 0$), Eq. (3.29) can be simplified to

$$\epsilon^2_{E_G}(0) = \frac{2 - 4\alpha + 11\alpha^2}{(2+\alpha)^2} \tag{3.32}$$

which has a minimum value of $1/3$ at $\alpha = 1/4$. Figure 3.5 plots Eqs. (3.29) and (3.32). It is apparent that $E_{G(1/4)}$ is more uniform than E_P, E_K, and E_T everywhere, both near

the boundary and in the region away from the boundary where a diffuse sound field can be claimed.

3.5 Ensemble Variance

In a recent publication, Jacobsen obtained the ensemble variance for the potential, kinetic and total energy densities by introducing an independent normally distributed random variable W to the diffuse field models discussed previously. The variable W has zero mean and a variance of $2/M_s$, and is meant to represent the relative variance of the point source sound power emission associated with the statistical modal overlap (M_s).[15] Following his approach, the relative ensemble variance of GED can be derived as

$$\begin{aligned}
\epsilon^2_{E_G} &= \frac{E\left[[\alpha E_P + (1-\alpha)(E_{Kx}+E_{Ky}+E_{Kz})]^2(1+W)^2\right]}{E^2\left[[\alpha E_P + (1-\alpha)(E_{Kx}+E_{Ky}+E_{Kz})](1+W)\right]} - 1 \\
&= \frac{3(1-\alpha)^2\left(E\left[E^2_{Kx}\right]+2E^2\left[E_{Kx}\right]\right)+\alpha^2 E\left[E^2_P\right]+6\alpha(1-\alpha)E\left[E_P\right]E\left[E_{Kx}\right]}{\mu^2_G}\left(1+E\left[W^2\right]\right)-1 \\
&= \left[\frac{4}{3}(1-\alpha)^2+2\alpha^2+2\alpha(1-\alpha)\right](1+\frac{2}{M_s})-1 \\
&= \frac{8+M_s-2(2+M_s)\alpha+4(2+M_s)\alpha^2}{3M_s}.
\end{aligned} \tag{3.33}$$

It is interesting to note that the optimal α value is again $1/4$, and the minimum variance is $\frac{1}{4}+\frac{5}{2M_s}$, compared to $1+\frac{4}{M_s}$ for E_P and $\frac{1}{3}+\frac{8}{3M_s}$ for both E_K and E_T.

The modal overlap can be calculated according to

$$M_s = \frac{12\pi ln(10)Vf^2}{T_{60}c^3}, \tag{3.34}$$

where V is the volume of the room and T_{60} is the reverberation time.[14] Figure 3.6 plots Eq. (3.33) for a room with volume 136.6 m^3 and a T_{60} of 6.2 s that is constant over frequency.

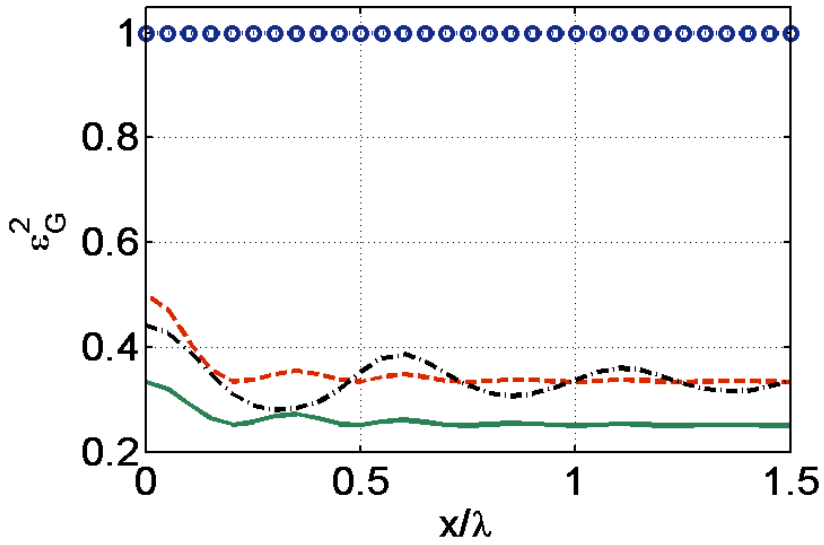

(a)

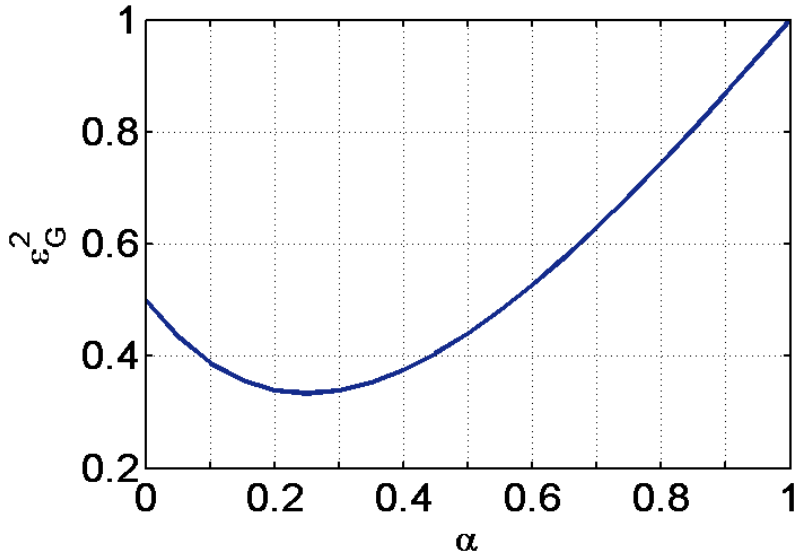

(b)

Figure 3.5 Relative spatial variance of GED close to a flat rigid boundary in a diffuse field. Plot (a) compares the relative variance for different GED quantities as a function of the distance x from the boundary. Plot (b) shows the relative variance of GED as a function of α at the boundary ($x \to 0$). In (a), "· · ◯ · ·": $E_{G(1)}$ (E_P); "– –": $E_{G(0)}$ (E_K); "–·–": $E_{G(1/2)}$ (E_T); "——": $E_{G(1/4)}$.

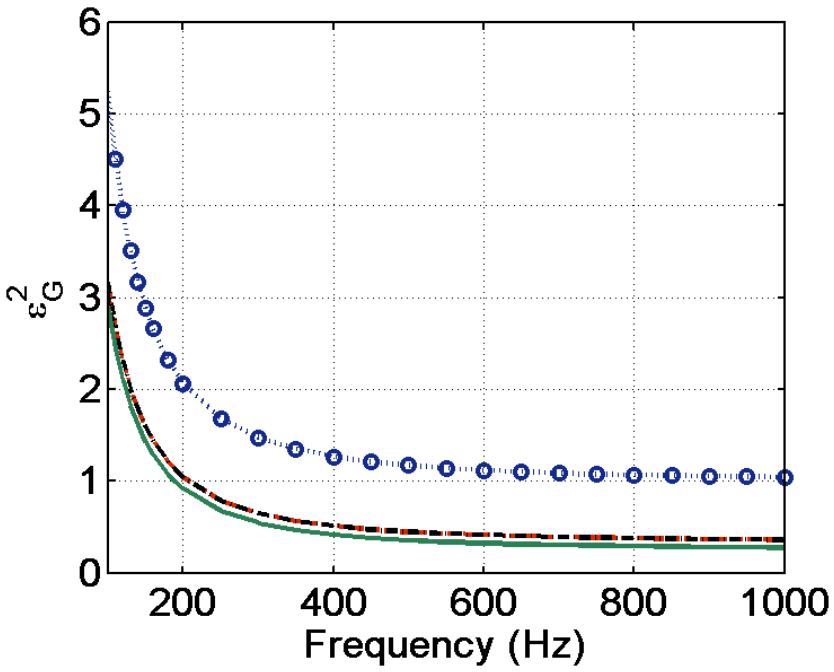

Figure 3.6 Ensemble variance of different GED quantities for a reverberation chamber with $V = 136.6\ m^2$ and uniform $T_{60} = 6.2$ s . "· · ◯ · ·": $E_{G(1)}$ (E_P); "– –": $E_{G(0)}$ (E_K); "–·–": $E_{G(1/2)}$ (E_T); "——": $E_{G(1/4)}$.

3.6 Numerical Verification

The hybrid modal expansion model was applied to compute the internal sound field (both complex pressure and complex particle velocity) of a rectangular room with dimensions $5.4\ m \times 6.3\ m \times 4\ m$. The room is very lightly damped with a uniform wall impedance $z = (50 + 100i)\rho_0 c$ and a Schroeder frequency of 347.6 Hz. Both the complex pressure and complex particle velocity fields are computed over the bandwidth of 200 Hz to 800 Hz with 1 Hz increment. Because of the fast convergence rate of the hybrid model, only about 3×10^4 modes were required for even the highest frequency. The source location was randomly selected for each frequency.

The relative variance of E_G with different α values is estimated by calculating the relative variance for E_G at 100 randomly selected receiver locations inside the room. The receiver locations are chosen to be at least a half wavelength away from the source as well as the boundary. The relative variance for 100 samples is then averaged over ten frequency bins to simulate the ensemble variance.[15,18] As shown in Fig.3.7, the simulation results match the theoretical predictions reasonably well (see Fig. 3.6).

The spatial correlation coefficient was estimated at 800 Hz using $11,000$ pairs of field points randomly sampled with the constraint that the separation distance between any two points of a pair is less than one and a half wavelengths. In addition, the sampling process was carefully designed so there were about 500 pairs falling into each of 22 intervals that equally divided one and a half wavelengths. The spatial correlation coefficient was calculated for each interval based on the samples. The results are shown in Fig. 3.8, which is in fairly good agreement with the theoretical predictions shown in Fig. 3.3.

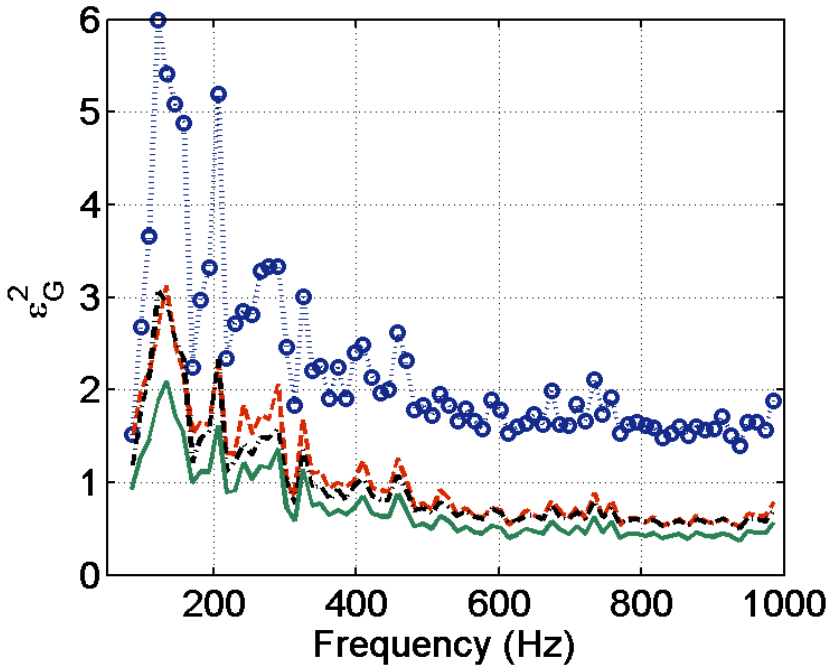

Figure 3.7 Numerical simulation results for the ensemble variance of different GED quantities for a lightly damped room. "··○··": $E_{G(1)}$ (E_P); "– –": $E_{G(0)}$ (E_K); "–·–": $E_{G(1/2)}$ (E_T); "——": $E_{G(1/4)}$.

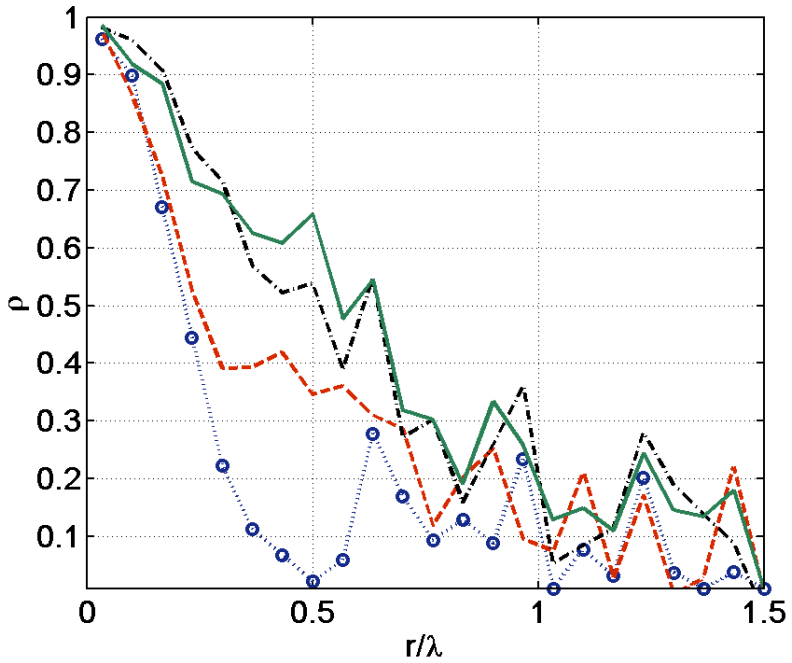

Figure 3.8 Numerical simulation results for the spatial correlation coefficient of GED in a diffuse field. "··◯··": $E_{G(1)}$ (E_P); "– –": $E_{G(0)}$ (E_K); "–·–": $E_{G(1/2)}$ (E_T); "——": $E_{G(1/4)}$.

3.7 Conclusions

Generalized acoustic energy density has been introduced in this chapter. Averaging over the volume of an enclosure, the GED has the same mean value as the acoustic total energy density and can revert to the traditional energy density quantities, such as acoustic potential energy density, acoustic kinetic energy density, and acoustic total energy density. By varying the weighting factors for the combination of acoustic potential energy density and acoustic kinetic energy density, an additional degree of freedom is added to the summed energy density quantity so that it can be optimized for different applications. Properties for GED with different values of α have been studied for individual room modes, the diffuse sound field, and the sound field below the Schroeder frequency.

The uniformity of a measured sound field often plays an important role in many applications. This work has shown that optimal weighting factors based on a single parameter α can minimize the spatial variance of the GED. For a single room mode, the optimal value of α may vary from 1/10 to 1/2, depending on the specific mode shape. For a diffuse field, the optimal value is 1/4 for both single frequency and narrow-band frequency excitations, and even for the region close to a rigid reflecting surface. For a diffuse field excited by a single tone source, $E_{G(1/4)}$ follows the distribution of $Gamma(4, \mu_0/4)$ and has a relative spatial variance of 1/4, compared to 1/3 for E_K and E_T. Below the Schroeder frequency of a room, a smaller ensemble variance can also be reached when $\alpha = 1/4$.

Chapter 4

GED-Based Measurement Techniques

4.1 Introduction

In this chapter, some preliminary studies will be reported to demonstrate the utilization of GED in applications of acoustic measurements in reverberation chambers.

4.2 Measuring GED

The techniques for measuring GED are essentially the same as those for measuring the total acoustic energy density. Obtaining the GED information involves measuring the sound pressure as well as the particle velocity at the same field point. The particle velocity estimation is usually where the difficulties lie.

The pressure microphone gradient technique for measuring the particle velocity has been studied and improved over time.[3,4,11,19–22] Although there are several approaches to implement the microphone gradient technique, they are all based on the same basic methodology which estimates the particle velocity from the spatial gradient of the sound pressure field. The spatial gradient of the sound pressure field is approximated from the difference between

the signals of closely spaced microphones. There is much discussion about this technique in the literature;[19–22] therefore the technical details will not be discussed here. The GED probe used in this research consisted of three pairs of phase-matched 1/2-inch microphones manufactured by G.R.A.S. (see Fig. 4.1). The microphone pairs were mounted perpendicular to each other, so three orthogonal particle velocity components could be estimated based on the pressure gradients. The spacing between microphones in each pair was 5 cm, which allowed good accuracy below 1000 Hz. The acoustic pressure was estimated by averaging the pressure signals from all six microphones in the probe.

Recently, a novel particle velocity measurement device, the "Microflown" sensor, has been made available to acousticians,[23,24] which expanded the methods available to measure acoustic energy density quantities. A typical Microflown sensor uses two or more very thin platinum wires that are heated electrically to detect the micro air flow (acoustic particle velocity) around the wires. After signal conditioning, the sensor is generally sensitive in the audio frequency range but with an imperfect frequency response. Multiple Microflown sensors can be mounted together with microphones to serve as a stand alone GED probe (see Fig. 4.2). However, the Microflown probe has not been used in this dissertation.

4.3 Reverberation Time Estimation

In the paper by Nutter, *et al.*,[27] the procedure of reverberation time (T_{60}) estimation based on the total acoustic energy density is investigated in detail. In that paper, impulse responses of multiple source-receiver locations were obtained for both acoustic pressure and particle velocity, from which an impulse response associated with the total energy density, h_{E_T}, could be computed as

$$h_{E_T}(t) = \frac{1}{2\rho_0 c^2} h_p^2(t) + \frac{\rho_0}{2} h_u^2(t), \tag{4.1}$$

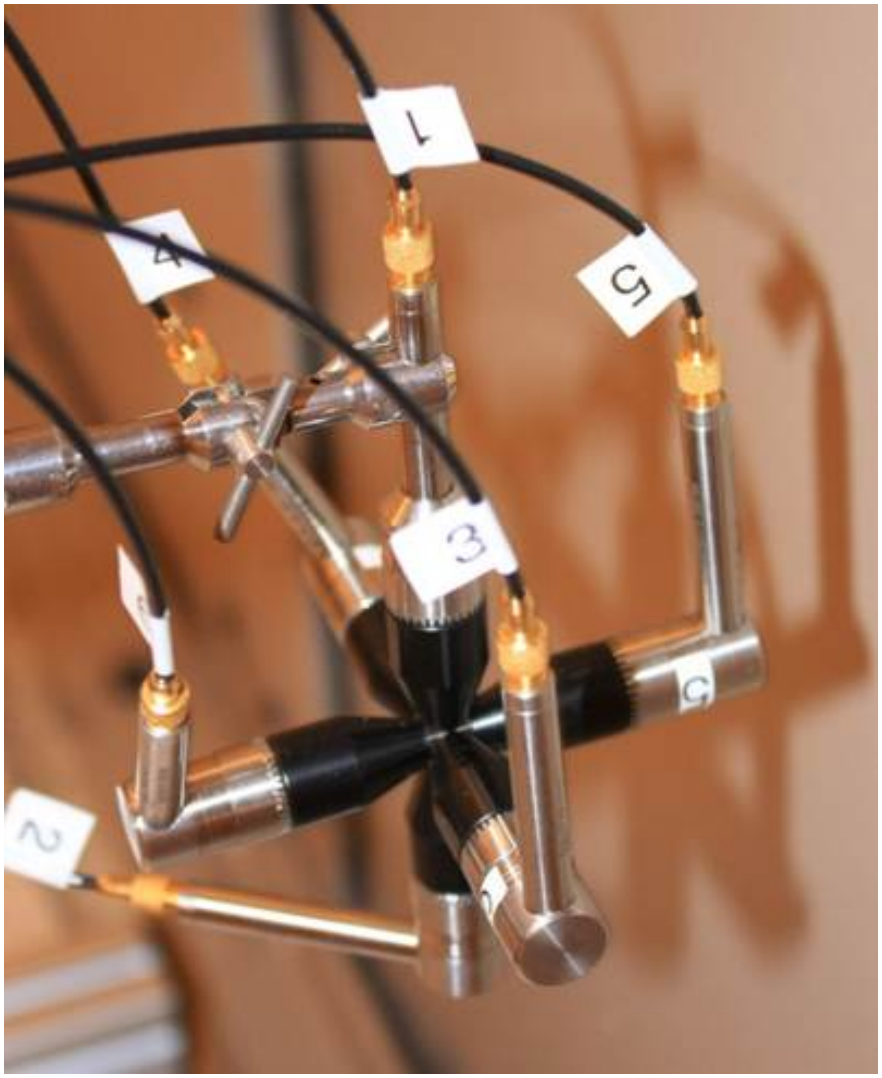

Figure 4.1 The microphone gradient GED probe.

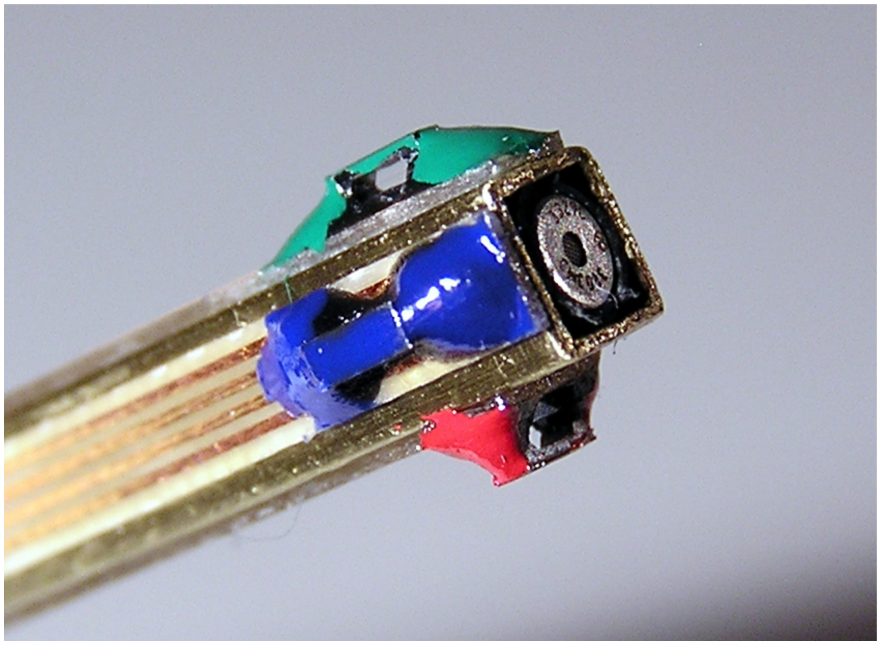

Figure 4.2 The Ultimate Sound Probe (USP). A USP probe consists of three orthogonal particle velocity components (the Micoflown sensors) and one pressure component (a microphone).

where h_p and h_u represent the impulse responses of acoustic pressure and particle velocity, respectively. The filtered impulse response for each frequency band of interest was then backward integrated to reduce the estimation variance.[59] After averaging the backward integrated curves for all source-receiver combinations, T_{60} values could be estimated from the slopes of the averaged curves. To utilize GED, the procedure is very much the same, except that the impulse response associated with GED, instead of the total energy density, is calculated by simply changing the coefficients in Eq. (4.1) from 1/2 to α and $1-\alpha$ for the first and second terms, respectively.

Reverberation times were thus obtained for a reverberation chamber based on GED with different values of α. The reverberation chamber dimensions were 4.96 $m \times$ 5.89 $m \times$ 6.98 m, giving a volume of 204 m^3. The chamber also incorporated stationary diffusers. The Schroeder frequency for this chamber was 410 Hz without added low-frequency absorption. A

dodecahedron loudspeaker driven by white noise was placed sequentially at two locations in the chamber. Again, the acoustic pressure and particle velocity fields were sampled with the pressure microphone gradient probe at six locations for each source location. The acoustic pressure was estimated by averaging the pressure signals from all six microphones in the probe. The impulse responses were computed by taking the inverse Fourier transform of the frequency responses between the acoustic pressure or particle velocity signal and the white noise signal input to the source. Technically, these impulse responses represent responses of both the chamber and the dodecahedron loudspeaker. However, the impulse response of the loudspeaker was too short to appreciably influence the T_{60} estimations. The impulse responses were filtered with one-third-octave band filters and backward integrated to estimate the T_{60} values within the bands.

Figure 4.3(a) compares the averaged T_{60} estimation based on GED with different α values. The various GED quantities result in almost identical reverberation times in most one-third-octave bands. However, the variance due to source-receiver locations differs, especially in the low frequency range. As shown in Fig. 4.3(b), the estimations based on E_K, E_T and $E_{G(1/4)}$ have notably less variance than E_P. Less variance implies a smaller number of measurements or better accuracy. Although the improvement over E_K and E_T is not large, the variance is the smallest for $E_{G(1/4)}$. Considering that there is essentially no additional effort added for measuring E_G comparing to E_K and E_T, $E_{G(1/4)}$ is recommended.

4.4 Sound Power Measurement in a Reverberation Chamber

Sound power measurement based on the use of kinetic energy density or total energy density was also investigated by Nutter, *et al.*[27] The procedure is relatively simple and very similar

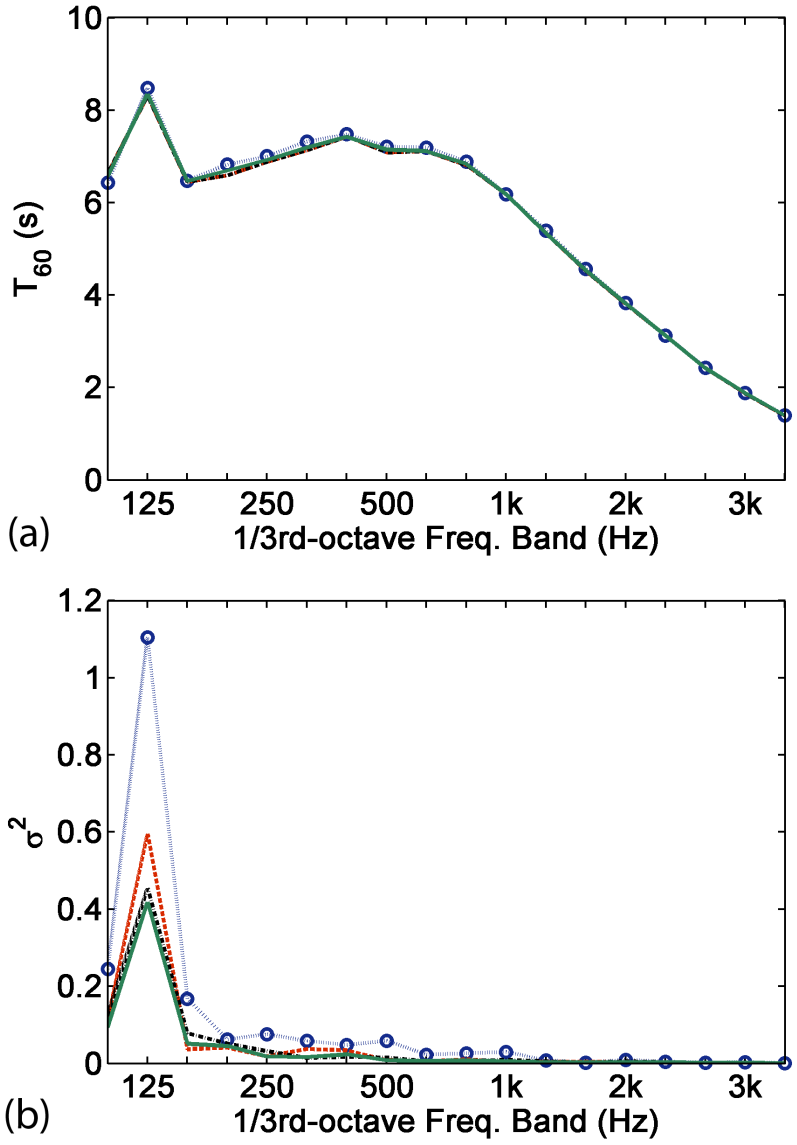

Figure 4.3 Reverberant time measurements using GED. (a) The averaged T_{60} estimation based on different GED quantities for a reverberation chamber. (b) Comparison of the variances of the T_{60} estimations due to the different source-receiver locations. "··◯··": $E_{G(1)}$ (E_P); "– –": $E_{G(0)}$ (E_K); "–·–": $E_{G(1/2)}$ (E_T); "——": $E_{G(1/4)}$.

to that based on the squared pressure described in the ISO 3741 standard. The spatially averaged sound level is the key parameter in the sound power estimation. In general, the more spatially uniform the sound field is, the fewer measurements are required to estimate the averaged sound level. The sound power measurement based on GED was investigated experimentally with the same equipment and in the same reverberation chamber described in the previous section. With the source being placed close to a corner in the reverberation chamber (the source was about 1.5 m away from the floor and walls), the GED field was sampled with the microphone gradient probe at six well separated locations (at least 1.5 m apart). The locations were randomly chosen with the constraint of being at least 1.5 m from the source and the walls.

Figure 4.4(a) shows the averaged GED levels, which can be calculated as $L_G = 10log(E_G/E_{Gref})$, where

$$\begin{aligned} E_{Gref} &= \alpha\frac{p_{ref}^2}{2\rho_0 c^2} + (1-\alpha)\frac{\rho_0}{2}v_{ref}^2 \\ &= \alpha\frac{p_{ref}^2}{2\rho_0 c^2} + (1-\alpha)\frac{\rho_0}{2}\frac{p_{ref}^2}{\rho_0^2 c^2} \\ &= \frac{p_{ref}^2}{2\rho_0 c^2} \\ &= \frac{(20\ \mu Pa)^2}{2\rho_0 c^2}. \end{aligned} \tag{4.2}$$

The agreement among different α values is good below the 1 kHz one-third-octave band. Above that frequency, the estimations diverge, likely due to the increased errors caused by the pressure gradient technique. The large difference at 100 Hz is caused by the large variance for the sound level of E_P. This can be seen in Fig. 4.4(b), which shows the standard deviation of the sound level for different measurement locations and different GED α values. Again, less variance for GED with $\alpha < 1$ can be observed, especially in the low-frequency range. In general, the sound level of $E_{G(1/4)}$ has the smallest standard deviation, but the improvement is not too dramatic when compared to E_K and E_T. However, again, $E_{G(1/4)}$ is

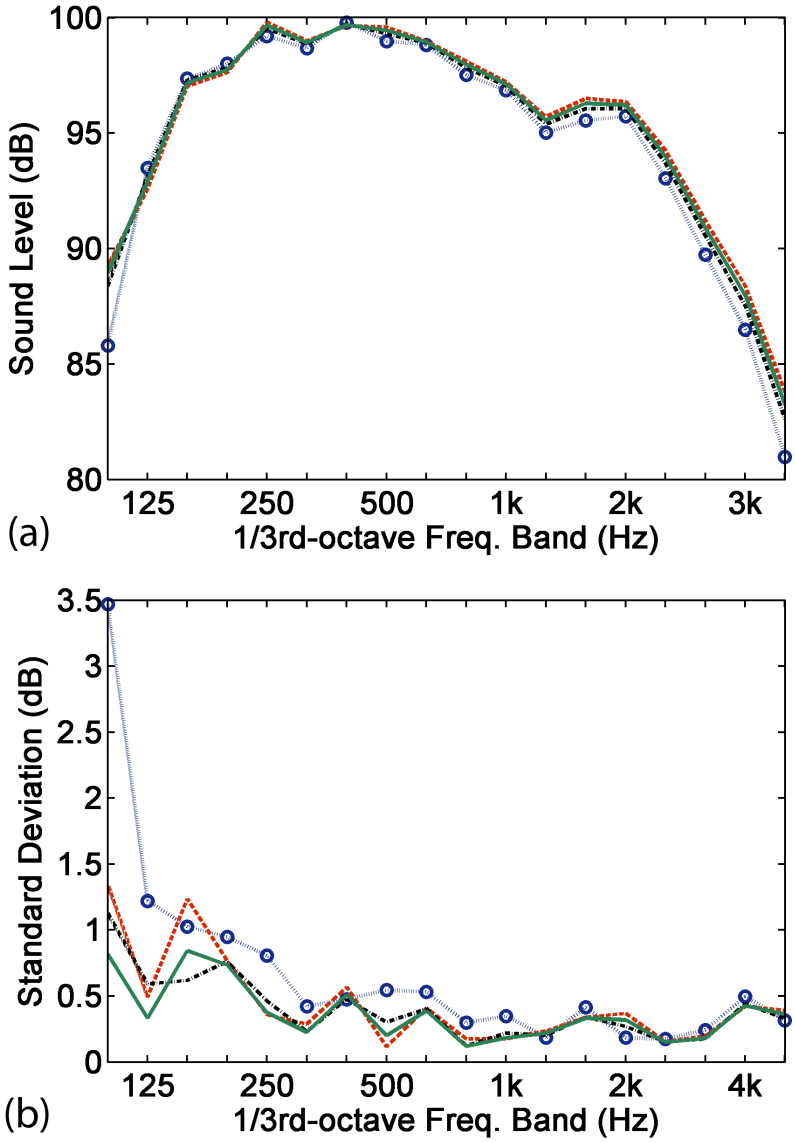

Figure 4.4 Sound level data for sound power measurements using GED. (a) Spatially averaged sound levels for different GED quantities in a reverberation chamber where the source under test is placed in a corner and 1.5 m away from the floor and walls. (b) Standard deviation of sound levels for the different source-receiver locations. "··◯··": $E_{G(1)}$ (E_P); "– –": $E_{G(0)}$ (E_K); "–·–": $E_{G(1/2)}$ (E_T); "—": $E_{G(1/4)}$.

recommended due to its improved uniformity with a measurement effort similar to those of E_T and E_K.

4.5 Conclusion

The techniques of measuring GED have been introduced in this chapter. In general, the approach used for measuring the total acoustic energy density can be easily modified for GED measurements.

Benefits of total-energy-density-based techniques have been shown in the past. Experimental studies of GED-based reverberation time and sound power measurements in a reverberation chamber confirm the improved uniformity of $E_{G(1/4)}$, especially in the low-frequency region. They indicate that more reliable results may be obtained using $E_{G(1/4)}$ for those measurements.

In general, $E_{G(1/4)}$-based techniques do result in improvements compared to E_T-and E_P-based techniques. The degree of the improvements was not large compared to the E_T-based techniques. However, since $E_{G(1/4)}$ requires no additional effort to implement in most applications, and it is very simple to modify existing E_T-based techniques, the $E_{G(1/4)}$-based techniques may be considered to be superior.

Chapter 5

GED-Based Active Noise Control

5.1 Introduction

Active noise control (ANC) of enclosed sound fields was first studied systematically by Nelson, *et al.* more than twenty years ago.[60–62] In the low frequency range (below the Schroeder frequency), it has been shown that control of the global potential energy can be achieved for resonance frequencies of an enclosure by minimizing the squared pressure response at one or multiple field locations with one or more remotely placed secondary sources. Because of the relatively large spatial fluctuations in the enclosed squared pressure field, research has been carried out to determine the optimal location for the error sensors as well as the secondary source locations.[41,61,63]

For a diffuse sound field (above the Schroeder frequency) global control is usually not feasible with remotely placed secondary sources,[60] and only local "quiet zones" can be achieved.[57,64,65] The average 10 dB zone of quiet, which is defined to be the region around the error sensor where the attenuation is at least 10dB, is reported to be a sphere with a diameter of about one-tenth of a wavelength for one error sensor and one remote secondary source ANC system.[57] Effort has been carried out to increase this 10 dB quiet zone by

placing the error sensor in the near-field of the secondary source.[64]

Instead of minimizing squared pressure, the use of total acoustic energy density (ED) as the minimization quantity has been demonstrated to yield improved performance in low modal density acoustic fields, often resulting in improved global attenuation due to the fact that ED is more spatially uniform than squared pressure and therefore provides more global information.[25,26]

In this chapter, the GED-based active noise control of the enclosed sound field will be studied in both the low and high frequency ranges. It will be shown that GED-based active noise control can improve the results of ED-based ANC in the low frequency range. In addition, GED will be optimized to control noise in a diffuse sound field.

This chapter will be organized as follows. An expression for the secondary source strength to minimize the GED response will be derived in Section 5.2. GED-based global control in the low frequency range will be studied numerically in Section 5.3. In Section 5.4, the zone of quiet for GED-based ANC will be studied analytically for diffuse fields. Then, the analytical results will be verified by a numerical simulation in Section 5.5. In Section 5.6, a modified filtered-x algorithm will be introduced for GED-based ANC. finally, an experimental study will be presented in Section 5.7.

5.2 GED-based ANC

For active noise control inside an enclosure, the usual approach taken is to minimize the squared pressure response at an error sensor location by adjusting the complex source strength (both amplitude and phase) of the secondary source. In this section, a mathematical derivation is carried out to find the optimal complex source strength if the GED response is minimized.

Suppose the noise field in an enclosure is excited by a single-tone primary noise source.

The acoustic pressure and three particle velocity components are known and denoted as $\hat{p}_p(\mathbf{r})$, $\hat{v}_{p1}(\mathbf{r})$, $\hat{v}_{p2}(\mathbf{r})$ and $\hat{v}_{p3}(\mathbf{r})$, respectively. The subscript $_p$ represents the primary sound field. If a secondary source is introduced in the enclosure, then the superposed GED field can be calculated as

$$\begin{aligned} E_{G(\alpha)}(\mathbf{r_0}) &= \frac{\alpha}{2\rho_0 c^2}(\hat{p}_p(\mathbf{r_0})+\hat{p}_s(\mathbf{r_0}))(\hat{p}_p(\mathbf{r_0})+\hat{p}_s(\mathbf{r_0}))^* \\ &+ \frac{1-\alpha}{2}\rho_0\sum_{l=1}^{3}(\hat{v}_{pl}(\mathbf{r_0})+\hat{v}_{sl}(\mathbf{r_0}))(\hat{v}_{pl}(\mathbf{r_0})+\hat{v}_{sl}(\mathbf{r_0}))^*, \end{aligned} \tag{5.1}$$

where $\hat{p}_s(\mathbf{r_0})$ and $\hat{v}_{sl}(\mathbf{r_0})$ represent the pressure and the three components of the particle velocity fields due to the secondary source only. The subscript $_s$ represents the secondary sound field.

The secondary sound pressure and particle velocity fields are usually not known before the control system is turned on. However, the spatial transfer functions are often known and Eq. (5.1) can be modified to

$$\begin{aligned} E_{G(\alpha)}(\mathbf{r_0}) &= \frac{\alpha}{2\rho_0 c^2}[\hat{p}_p(\mathbf{r_0})+(\hat{Q}_{sr}+i\hat{Q}_{si})\hat{Z}p_s(\mathbf{r_0}))(\hat{p}_p(\mathbf{r_0})+(\hat{Q}_{sr}+i\hat{Q}_{si})\hat{Z}p_s(\mathbf{r_0}))^* \\ &+ \frac{1-\alpha}{2}\rho_0\sum_{l=1}^{3}[\hat{v}_{pl}(\mathbf{r_0})+(\hat{Q}_{sr}+i\hat{Q}_{si})\hat{Z}v_{sl}(\mathbf{r_0})][\hat{v}_{pl}(\mathbf{r_0})+(\hat{Q}_{sr}+i\hat{Q}_{si})\hat{Z}v_{sl}(\mathbf{r_0})]^*, \end{aligned}$$

where $\hat{Q}_{sr}$ and $\hat{Q}_{si}$ represent the real and the imaginary parts of the complex secondary source strength $\hat{Q}_s$, and $\hat{Z}p_s$ and $\hat{Z}v_{sl}$ represent the transfer functions of the pressure and the different components of the particle velocity for the secondary sound field.

If one is trying to minimize the GED response at location $\mathbf{r_0}$, the optimal $\hat{Q}_s$ value can be solved for from

$$\begin{cases} \frac{\partial E_{G(\alpha)}(\mathbf{r_0})}{\partial \hat{Q}_{sr}} = 0, \\ \frac{\partial E_{G(\alpha)}(\mathbf{r_0})}{\partial \hat{Q}_{si}} = 0, \end{cases} \tag{5.2}$$

and the solution is

$$\begin{aligned}\hat{Q}_s &= \hat{Q}_{sr} + i\hat{Q}_{si} \\ &= -\frac{\alpha\hat{p}_p(\mathbf{r_0})\hat{Z}p_s^*(\mathbf{r_0}) + (1-\alpha)\rho_0^2c^2\left[\sum_{l=1}^{3}\hat{v}_{pl}(\mathbf{r_0})\hat{Z}v_{sl}^*(\mathbf{r_0})\right]}{\alpha\hat{Z}p_s(\mathbf{r_0})\hat{Z}p_s^*(\mathbf{r_0}) + (1-\alpha)\rho_0^2c^2\left[\sum_{l=1}^{3}\hat{Z}v_{sl}(\mathbf{r_0})\hat{Z}v_{sl}^*(\mathbf{r_0})\right]}.\end{aligned} \tag{5.3}$$

If the primary sound field is also expressed in terms of the primary source strength, $\hat{Q}_p$, and the spatial transfer functions for pressure and particle velocity components, $\hat{Z}p_p$ and $\hat{Z}v_{pl}$, then Eq. (5.3) becomes

$$\hat{Q}_s = -\hat{Q}_p\frac{\alpha\hat{Z}p_p(\mathbf{r_0})\hat{Z}p_s^*(\mathbf{r_0}) + (1-\alpha)\rho_0^2c^2\left[\sum_{l=1}^{3}\hat{Z}v_{pl}(\mathbf{r_0})\hat{Z}v_{sl}^*(\mathbf{r_0})\right]}{\alpha\hat{Z}p_s(\mathbf{r_0})\hat{Z}p_s^*(\mathbf{r_0}) + (1-\alpha)\rho_0^2c^2\left[\sum_{l=1}^{3}\hat{Z}v_{sl}(\mathbf{r_0})\hat{Z}v_{sl}^*(\mathbf{r_0})\right]}. \tag{5.4}$$

5.3 Global Active Noise Control in the Low-Frequency Range of an Enclosure

In a lightly damped enclosure, the total acoustic potential energy can be reduced at resonance frequencies below the Schroeder frequency by actively minimizing the squared acoustic pressure at error sensor locations using one or more secondary sources.[63] However, for given primary and secondary source locations, the global attenuation may vary over a large range for different error sensor placements. At off-resonance frequencies, negative attenuation can often be observed. There is an upper-bound limit for the attenuation that can be achieved by minimizing the global acoustic potential energy. However, in principle, this requires an infinite number of error sensors placed in the enclosure. If, instead of squared pressure, the total acoustic energy density is minimized at discrete locations, the undesirable effects of the error sensor positions can be reduced.[19,26] With the same number of error sensors, the global attenuation of the total-energy-density-based ANC is generally closer to the upper bound limit than the squared-pressure-based ANC.

Table 5.1 Room Modes of a Lightly Damped Enclosure (dimensions: 2.7 $m \times$ 3 $m \times 3.1$ m).

Mode	(0,0,1)	(1,2,0)	(0,0,2)	(2,0,1)	(1,2,1)	(1,1,2)
Modal Frequency (Hz)	54.59	126.10	126.18	126.70	138.45	138.53

In this section, the active noise cancellation based on GED in a lightly damped enclosure will be simulated numerically. The dimensions of the enclosure are 2.7 $m \times 3$ $m \times 3.1$ m and a few of the normal modes are listed in Table 5.1. One of the corners of the enclosure sits at the origin with the three adjoining edges lying along the positive direction of the x, y and z axes. One primary source is located close to a corner at $(0.27\ m, 0.3\ m, 0.31\ m)$, and one secondary source is located at $(2.2\ m, 2.0\ m, 0.94\ m)$. One error sensor is randomly placed in the enclosure with the only constraint being that it is at least one wavelength away from both sources. One hundred tests were performed, with the secondary source strength being adjusted each time to minimize GED at the randomly chosen error sensor location. The bandwidth of 40 Hz to 180 Hz was studied, with 1 Hz increments. The average attenuation over the tests of the total potential acoustic energy in the enclosure was compared for the various control schemes. As shown in Fig. 5.1(a), the E_T-based ANC is notably better than the E_K or E_P-based ANC. The E_P (or squared pressure) based ANC can result in large boosts for off-resonance frequencies, while the E_K and E_T-based ANC result in much smaller boosts. Figure 5.1(b) compares GED-based ANC for the α values of 0.1, 1/4, and $1/2(E_T)$, along with the upper bound limit. These three ANC results are very similar. The $E_{G(1/4)}$-based ANC tends to achieve a slightly better attenuation than the other two. The difference, however, is small except for the frequencies around 154 Hz. It can also be observed that the $E_{G(1/4)}$-based ANC generally has less variance than the other schemes (Fig. 5.2).

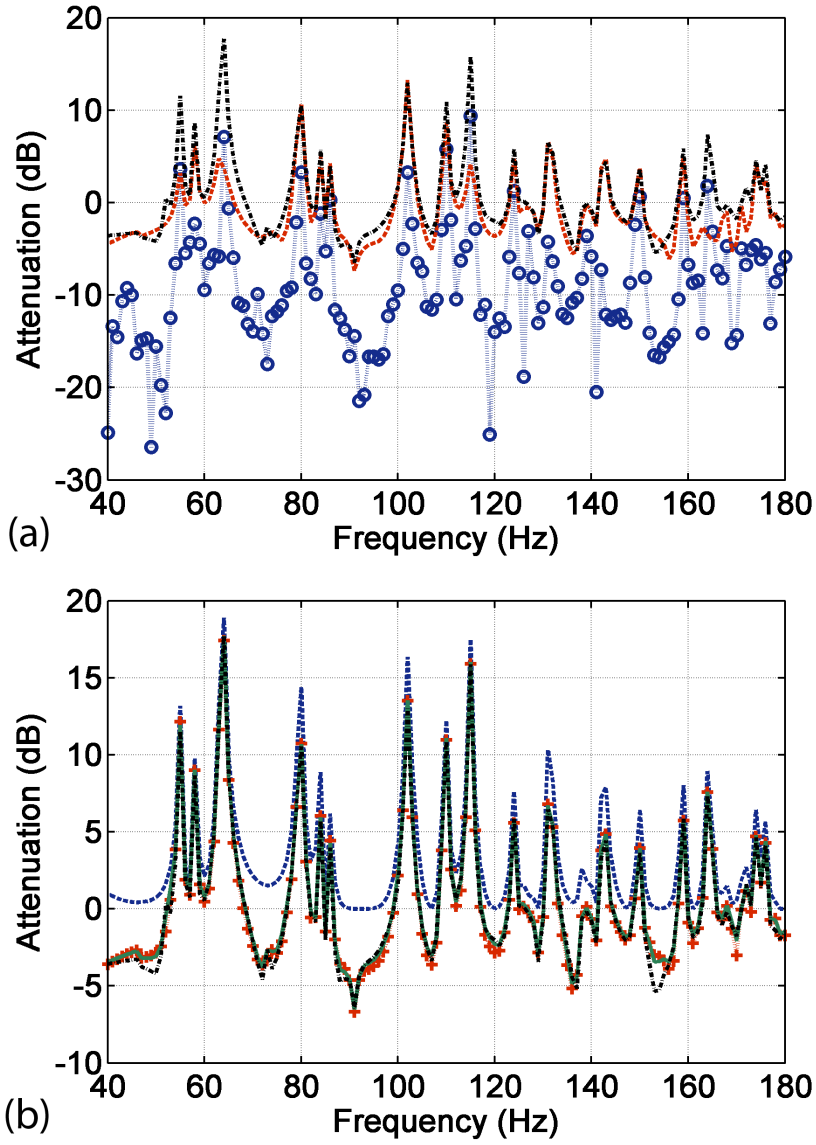

Figure 5.1 Averaged global attenuation using GED-based active noise cancellation in an enclosure with random error sensor locations. (a) Average attenuation based on $E_{G(1)}$ (E_P,"$-\bigcirc-$"), $E_{G(0)}$ (E_K, "$--$") and $E_{G(1/2)}$ (E_T, "$-.-$"). (b) Average attenuation based on $E_{G(1/2)}$ ("$-.-$"), $E_{G(1/4)}$ ("$—$") and $E_{G(1/10)}$ ("$\cdot + \cdot$") with the total potential energy upper-bound limit("$--$"). The attenuation based on total potential energy is considered optimal.

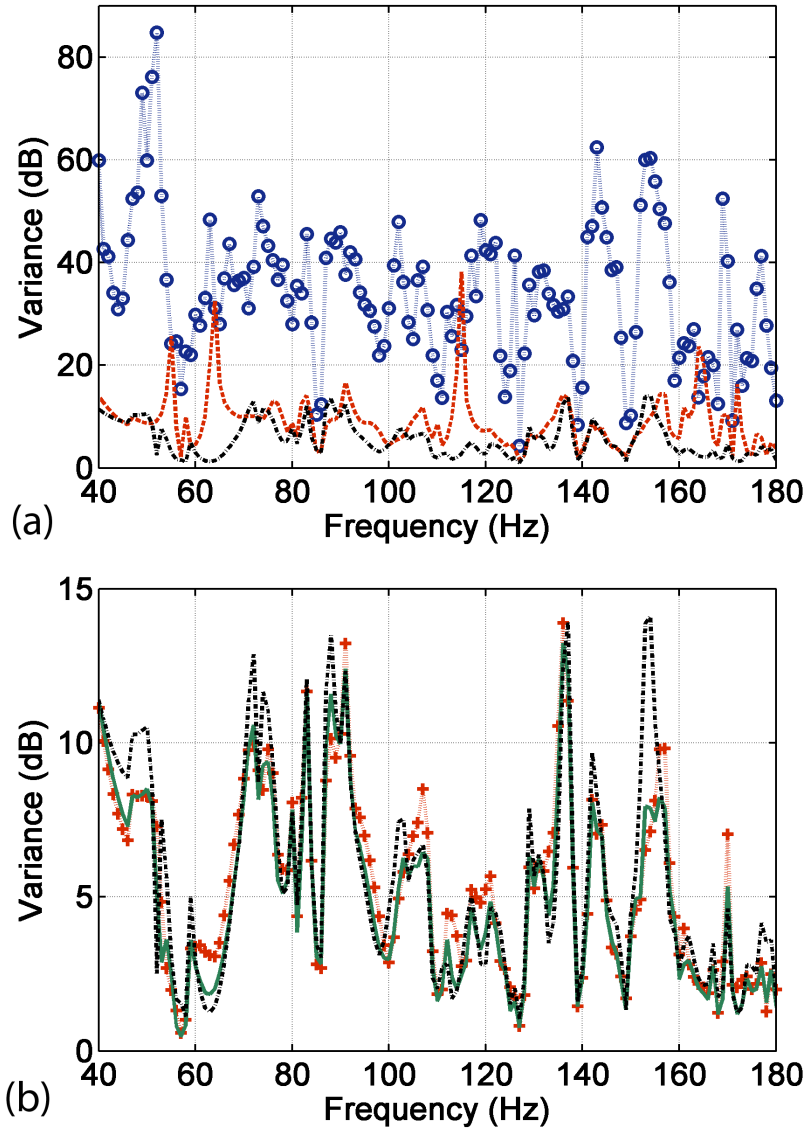

Figure 5.2 Variance of the attenuation. (a) Variance of the attenuation for $E_{G(1)}$ (E_P,"··○··"), $E_{G(0)}$ (E_K), "——") and $E_{G(1/2)}$ (E_T, "—·—"). (b) Variance of the attenuation for $E_{G(1/2)}$ ("—·—"), $E_{G(1/4)}$ ("——") and $E_{G(1/10)}$ ("··+··").

5.4 Zone of Quiet in A Diffuse Sound Field

For a diffuse sound field excited by a single-tone noise source, global active noise control cannot be achieved unless the control source is placed within half a wavelength from the primary source.[60] When the control source and the primary source are far away from each other, only local attenuation can be obtained. If the pressure response is minimized at the location $\mathbf{r_0}$, which is in the far-field of both sources, an expression for the spatially averaged squared pressure field around $\mathbf{r_0}$ has been derived by Elliot, *et al.*[57] The derivation begins by treating the instantaneous sound pressure at $\mathbf{r_0} + \mathbf{\Delta r}$ in the diffuse field excited by the primary source as the sum of two components,

$$p_p(\mathbf{r_0} + \mathbf{\Delta r}) = p_{pc}(\mathbf{r_0} + \mathbf{\Delta r}) + p_{pu}(\mathbf{r_0} + \mathbf{\Delta r}), \tag{5.5}$$

where $p_{pc}(\mathbf{r_0} + \mathbf{\Delta r}) = sinc(k\Delta r)p_p(\mathbf{r_0})$, in which k is the wavelength and $\Delta r = |\mathbf{\Delta r}|$. p_{pc} is fully correlated to $sinc(k\Delta r)p_p(\mathbf{r_0})$, while it will be shown later that p_{pu} is absolutely uncorrelated to $sinc(k\Delta r)p_p(\mathbf{r_0})$.

For the pressure at two points in a diffuse field that are $\mathbf{\Delta r}$ apart, the time averaged spatial cross-correlation function can be written as[55]

$$\overline{\langle p(\mathbf{r})p(\mathbf{r} + \mathbf{\Delta r})\rangle} = \mu^2 sinc(k\Delta r), \tag{5.6}$$

where $\overline{\cdots}$ denotes the time average, $< \cdot >$ denotes the spatial average with respect to $\mathbf{r}$, and $\mu^2 = \overline{\langle p^2(r)\rangle}$ is the spatially averaged mean square pressure. Utilizing Eq. (5.6), one can derive that

$$\begin{aligned}
\overline{\langle p_p(\mathbf{r_0})p_p(\mathbf{r_0} + \mathbf{\Delta r})\rangle} &= \overline{\langle p_p(\mathbf{r_0})p_{pc}(\mathbf{r_0} + \mathbf{\Delta r})\rangle} + \overline{\langle p_p(\mathbf{r_0})p_{pu}(\mathbf{r_0} + \mathbf{\Delta r})\rangle} \\
&= \mu_p^2 sinc(k\Delta r) + \overline{\langle p_p(\mathbf{r_0})p_{pu}(\mathbf{r_0} + \mathbf{\Delta r})\rangle} \\
&= \mu_p^2 sinc(k\Delta r).
\end{aligned} \tag{5.7}$$

Comparing to Eq. (5.6), Eq. (5.7) leads to $\overline{\langle p_p(\mathbf{r_0})p_{pu}(\mathbf{r_0}+\mathbf{\Delta r})\rangle} = 0$ as well as $\overline{\langle p_{pc}p_{pu}\rangle} = 0$. Therefore $p_{pu}(\mathbf{r_0}+\mathbf{\Delta r})$ is uncorrelated to both $p_p(\mathbf{r_0})$ and $p_{pc}(\mathbf{r_0}+\mathbf{\Delta r})$. With the use of the correlation relationship, the spatially averaged squared pressure can be calculated as

$$\begin{aligned}\overline{< p_p^2(\mathbf{r_0}+\mathbf{\Delta r}) >} &= \overline{< [p_{pc}(\mathbf{r_0}+\mathbf{\Delta r}) + p_{pu}(\mathbf{r_0}+\mathbf{\Delta r})]^2 >} \\ &= sinc^2(k\Delta r)\overline{< p_p^2(\mathbf{r_0}) >} + \overline{< p_{pu}^2(\mathbf{r_0}+\mathbf{\Delta r}) >}. \end{aligned} \tag{5.8}$$

Given that $\overline{< p_p^2(\mathbf{r_0}+\mathbf{\Delta r}) >} = \overline{< p_p^2(\mathbf{r_0}) >} = \mu_p^2$, $\overline{< p_{pu}^2(\mathbf{r_0}+\mathbf{\Delta r}) >}$ can be solved for from Eq. (5.8):

$$\begin{aligned} & \overline{< p_p^2(\mathbf{r_0}+\mathbf{\Delta r_0}) >} = sinc^2(k\Delta r)\overline{< p_p^2(\mathbf{r_0}) >} + \overline{< p_{pu}^2(\mathbf{r_0}+\mathbf{\Delta r}) >} \\ \Rightarrow\ & \mu_p^2 = sinc^2(k\Delta r)\mu_p^2 + \overline{< p_{pu}^2(\mathbf{r_0}+\mathbf{\Delta r}) >} \\ \Rightarrow\ & \overline{< p_{pu}^2(\mathbf{r_0}+\mathbf{\Delta r}) >} = [1 - sinc^2(k\Delta r)]\mu_p^2. \end{aligned} \tag{5.9}$$

Similarly, for the diffuse field excited by the secondary source, we have

$$p_s(\mathbf{r_0}+\mathbf{\Delta r}) = p_{sc}(\mathbf{r_0}+\mathbf{\Delta r}) + p_{su}(\mathbf{r_0}+\mathbf{\Delta r}), \tag{5.10}$$

where $p_{sc}(\mathbf{r_0}+\mathbf{\Delta r}) = sinc(k\Delta r)p_s(\mathbf{r_0})$, and

$$\overline{< p_{su}^2(\mathbf{r_0}+\mathbf{\Delta r}) >} = [1 - sinc^2(k\Delta r)]\mu_s^2. \tag{5.11}$$

For both the primary and secondary source operating together, the total pressure field around the error sensor location can be written as

$$p(\mathbf{r_0}+\mathbf{\Delta r}) = p_p(\mathbf{r_0}+\mathbf{\Delta r}) + p_s(\mathbf{r_0}+\mathbf{\Delta r}). \tag{5.12}$$

The ensemble average of the mean square value can be calculated using Eqs. (5.9) and (5.11):

$$\begin{aligned}\overline{< p^2(\mathbf{r_0}+\mathbf{\Delta r}) >} &= \overline{< [p_p(\mathbf{r_0}+\mathbf{\Delta r}) + p_s(\mathbf{r_0}+\mathbf{\Delta r})]^2 >} \\ &= \overline{< [p_{pc}(\mathbf{r_0}+\mathbf{\Delta r}) + p_{sc}(\mathbf{r_0}+\mathbf{\Delta r})]^2 >} \\ &\quad + \overline{< p_{pu}^2(\mathbf{r_0}+\mathbf{\Delta r}) >} + \overline{< p_{su}^2(\mathbf{r_0}+\mathbf{\Delta r}) >} \\ &= sinc^2(k\Delta r)\overline{< p^2(\mathbf{r_0}) >} + [1 - sinc^2(k\Delta r)][\mu_p^2 + < \mu_s^2 >]. \end{aligned} \tag{5.13}$$

Here, μ_s^2 is treated as a random variable because it varies according to the primary field as well as the error sensor and secondary source locations [See Eq. (5.4)]. Equation (5.13) shows that the squared pressure around the error sensor is influenced by both the pressure at the error sensor $\overline{< p^2(\mathbf{r_0}) >}$ and the sum of the averaged primary pressure and the averaged secondary pressure $\mu_p^2 + < \mu_s^2 >$. When $\Delta r \ll 1$, $sinc^2(k\Delta r) \approx 1$ and the first term on the right hand-side of Eq. (5.13) dominates. Thus in the near-field of the error sensor, one has

$$\overline{< p^2(\mathbf{r_0} + \mathbf{\Delta r}) >} \approx sinc^2(k\Delta r)\overline{< p^2(\mathbf{r_0}) >}. \tag{5.14}$$

On the other hand, in the far-field of the error sensor ($\Delta r > 1/2\lambda$), one has

$$\overline{< p^2(\mathbf{r_0} + \mathbf{\Delta r}) >} \approx \mu_p^2 + < \mu_s^2 >, \tag{5.15}$$

which is greater than or equal to the averaged primary pressure field, μ_p^2.

If the spatially averaged mean square pressure quantities are normalized by the averaged mean squared primary pressure, Eq. (5.13) becomes

$$\frac{\overline{< p^2(\mathbf{r_0} + \mathbf{\Delta r}) >}}{\mu_p^2} = sinc^2(k\Delta r)\frac{\overline{< p^2(\mathbf{r_0}) >}}{\mu_p^2} + [1 - sinc^2(k\Delta r)](1 + \frac{< \mu_s^2 >}{\mu_p^2}). \tag{5.16}$$

The fraction in the first term of the right-hand side of Eq. (5.16) represents the normalized mean squared pressure at the error sensor location. If the pressure response is minimized at location $\mathbf{r_0}$, then ideally $\overline{< p^2(\mathbf{r_0}) >}$ vanishes, and Eq. (5.13) becomes

$$\frac{\overline{< p^2(\mathbf{r_0} + \mathbf{\Delta r}) >}}{\mu_p^2} = [1 - sinc^2(k\Delta r)](1 + \frac{< \mu_s^2 >}{\mu_p^2}) \tag{5.17}$$

which was originally derived by Elliot, *et al.*.[57] If GED is minimized instead, the normalized pressure at $\mathbf{r_0}$ is not zero anymore, and can be calculated in the frequency domain as

$$\begin{aligned}
\frac{\overline{< p^2(\mathbf{r_0}) >}}{\mu_p^2} &= \frac{< [\hat{p}_p(\mathbf{r_0}) + \hat{p}_s(\mathbf{r_0})][\hat{p}_p(\mathbf{r_0}) + \hat{p}_s(\mathbf{r_0})]^* >}{< \hat{p}_p\hat{p}_p^* >} \\
&= \frac{< [\hat{Q}_p\hat{Z}p_p(\mathbf{r_0}) + \hat{Q}_s\hat{Z}p_s(\mathbf{r_0})][\hat{Q}_p\hat{Z}p_p(\mathbf{r_0}) + \hat{Q}_s\hat{Z}p_s(\mathbf{r_0})]^* >}{< \hat{Q}_p\hat{Z}p_p\hat{Q}_p^*\hat{Z}p_p^* >} \\
&= \frac{< [\hat{Z}p_p(\mathbf{r_0}) + (\hat{Q}_s/\hat{Q}_p)\hat{Z}p_s(\mathbf{r_0})][\hat{Z}p_p(\mathbf{r_0}) + (\hat{Q}_s/\hat{Q}_p)\hat{Z}p_s(\mathbf{r_0})]^* >}{< \hat{Z}p_p\hat{Z}p_p^* >},
\end{aligned} \tag{5.18}$$

where Q_s can be found in Eq. (5.4). The substitution of Eq. (5.4) into Eq. (5.18) makes the expression rather complicated. However, given that $\hat{Z}p_p$, $\hat{Z}p_s$, $\hat{Z}v_{pl}$ and $\hat{Z}v_{sl}$ are all mutually independent variables with mean values being equal to zero, and $< \hat{Z}v_{pl}\hat{Z}v_{pl}^* > / < \hat{Z}p_p\hat{Z}p_p^* >= 1/3$,[10] the expression can be simplified to

$$\frac{\overline{< p^2(\mathbf{r_0}) >}}{\mu_p^2} = \frac{(1-\alpha)^2}{3}\left\langle \frac{E_{PZs}E_{KZs} + 3E_{KZs}^2}{\left[\alpha E_{PZs} + (1-\alpha)E_{KZs}\right]^2} \right\rangle, \tag{5.19}$$

where $E_{PZs} = \hat{Z}p_s\hat{Z}p_s^*$ and $E_{KZs} = \rho_0^2 c^2 \sum_{i=1}^{3} \hat{Z}v_{sl}\hat{Z}v_{sl}^*$. E_{PZs} and E_{KZs} are independent random variables and have the same mean value, $< E_{PZs} >=< E_{KZs} >= \mu_Z$. In addition, E_{PZs}/μ_Z is distributed as $Gamma(1,1)$, and E_{KZs}/μ_Z is distributed as $Gamma(3,1/3)$. Therefore, Eq. (5.19) can be expressed as

$$\begin{aligned}
\frac{\overline{< p^2(\mathbf{r_0}) >}}{\mu_p^2} &= \frac{(1-\alpha)^2}{3}\left\langle \frac{E_{PZs}E_{KZs} + 3E_{KZs}^2}{\left[\alpha E_{PZs} + (1-\alpha)E_{KZs}\right]^2} \right\rangle \\
&= \frac{(1-\alpha)^2}{3}\left\langle \frac{E_{PZs}E_{KZs}/\mu_Z^2 + 3E_{KZs}^2/\mu_Z^2}{\left[\alpha E_{PZs}/\mu_Z + (1-\alpha)E_{KZs}/\mu_Z\right]^2} \right\rangle \\
&= \frac{(1-\alpha)^2}{3}\int_0^\infty\int_0^\infty \frac{xy + 3y^2}{\left[\alpha x + (1-\alpha)y\right]^2}\cdot e^{-x}\cdot\frac{27y^2e^{-3y}}{2}\,dx\,dy.
\end{aligned} \tag{5.20}$$

The integration in Eq. (5.20) is still involved. However, it is possible to obtain some important properties of $\overline{< p^2(\mathbf{r_0}) >}/\mu_p^2$ fairly easily. First, $\overline{< p^2(\mathbf{r_0}) >}/\mu_p^2$ is monotonically decreasing in the domain of $0 \le \alpha \le 1$, which can be proven by showing that the derivative with respect to α is always negative. When α is equal to one, GED reverts to the potential energy density (or squared pressure). Therefore it is not surprising that the squared pressure at the error sensor location reaches its minimum value, zero, when squared pressure is minimized.

When $\alpha = 0$, which is equivalent to minimizing the squared particle velocity, Eq. (5.20) is relatively easier to evaluate and becomes

$$\left.\frac{\overline{< p^2(\mathbf{r_0}) >}}{\mu_p^2}\right|_{\alpha=0} = \frac{1}{3}\int_0^\infty\int_0^\infty \frac{x+3y}{y}\cdot e^{-x}\cdot\frac{27y^2e^{-3y}}{2}\,dx\,dy = \frac{3}{2}, \tag{5.21}$$

which indicates an amplified pressure field at the error sensor location. Another easily

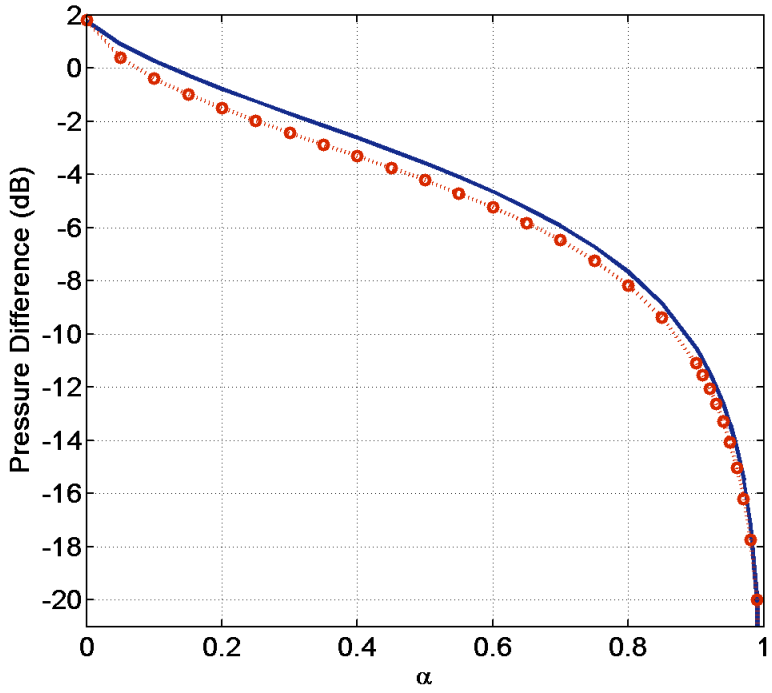

Figure 5.3 Averaged mean square pressure at the error sensor location when GED is minimized. Eq. (5.20) is evaluated numerically and $10log(\overline{< p^2(\mathbf{r_0}) >}/\overline{< p_p^2 >})$ is plotted. "——": analytical results; "· · ◯ · ·": numerical simulation.

integrated case is when $\alpha = 1/4$, resulting in

$$\left.\frac{\overline{< p^2(\mathbf{r_0}) >}}{\mu_p^2}\right|_{\alpha=0} = \frac{3}{64}\int_0^\infty\int_0^\infty \frac{y}{x+3y}\cdot e^{-x}\cdot\frac{27y^2e^{-3y}}{2}\,dx\,dy = \frac{3}{4}. \tag{5.22}$$

A numerical evaluation of Eq. (5.20) for $0 \le \alpha \le 1$ is plotted in Fig. 5.3 on a logarithmic scale. In order to reduce the squared pressure at the error sensor location to at least 10 dB lower than the averaged primary squared pressure, α needs to be greater than about 0.9. When α is around 0.6, only about 5 dB reduction can be achieved.

In a similar manner, the term, $< \mu_s^2 >$, in Eq. (5.13) and Eq. (5.16) can be calculated as

follows.

$$\begin{aligned} < \mu_s^2 > &= < \hat{Q}_s(\mathbf{r_0})\hat{Z}p_s(\mathbf{r})\hat{Q}_s^*(\mathbf{r_0})\hat{Z}p_s^*(\mathbf{r}) > \\ &= < \hat{Q}_s\hat{Q}_s^* >< \hat{Z}p_s\hat{Z}p_s^* > \end{aligned} \tag{5.23}$$

For the frequency range well above the Schroeder frequency, $\left\langle \hat{Z}p_s\hat{Z}p_s^* \right\rangle$ is equal to $< \hat{Z}p_p\hat{Z}p_p^* >$; therefore

$$\begin{aligned} < \hat{Q}_s\hat{Q}_s^* >< \hat{Z}p_s\hat{Z}p_s^* > &= \frac{< \hat{Q}_s\hat{Q}_s^* >}{\hat{Q}_p\hat{Q}_p^*} \cdot \hat{Q}_p\hat{Q}_p^* < \hat{Z}p_p\hat{Z}p_p^* > \\ &= \left\langle \frac{\hat{Q}_s}{\hat{Q}_p}\frac{\hat{Q}_s^*}{\hat{Q}_p^*} \right\rangle \mu_p^2 \end{aligned} \tag{5.24}$$

By substituting Eq. (5.4) and following the considerations to derive Eq. (5.20), the averaged ratio of secondary source strength to the primary source strength can be calculated as

$$\begin{aligned} \left\langle \frac{\hat{Q}_s}{\hat{Q}_p}\frac{\hat{Q}_s^*}{\hat{Q}_p^*} \right\rangle &= \left\langle \frac{3\alpha^2 E_{PZs} + (1-\alpha)^2 E_{KZs}}{3[\alpha E_{PZs} + (1-\alpha)E_{KZs}]^2} \right\rangle \\ &= \int_0^\infty\int_0^\infty \frac{3\alpha^2 x + (1-\alpha)^2 y}{3\left[\alpha x + (1-\alpha)y\right]^2} \cdot e^{-x} \cdot \frac{27y^2e^{-3y}}{2}\, dx\, dy, \end{aligned} \tag{5.25}$$

Substituting Eqs. (5.24) and (5.25) into Eq. (5.23) leads to

$$\begin{aligned} \frac{< \mu_s^2 >}{\mu_p^2} &= \left\langle \frac{\hat{Q}_s}{\hat{Q}_p}\frac{\hat{Q}_s^*}{\hat{Q}_p^*} \right\rangle \\ &= \int_0^\infty\int_0^\infty \frac{3\alpha^2 x + (1-\alpha)^2 y}{3\left[\alpha x + (1-\alpha)y\right]^2} \cdot e^{-x} \cdot \frac{27y^2e^{-3y}}{2}\, dx\, dy. \end{aligned} \tag{5.26}$$

It can be shown that the source strength ratio has a minimum value of 1/3 when $\alpha = 1/4$. In addition, the ratio approaches infinity when $\alpha = 0$, which was originally derived theoretically by Elliott, *et al.*[57] In that reference, Elliott, *et al.* assigned a value of 3 for this situation based on a numerical study due to the consideration that the secondary source power may not reach infinity in reality. Those authors, however, noticed the lack of repeatability in the numerical simulation results. As is found later in this chapter, it was found numerically and

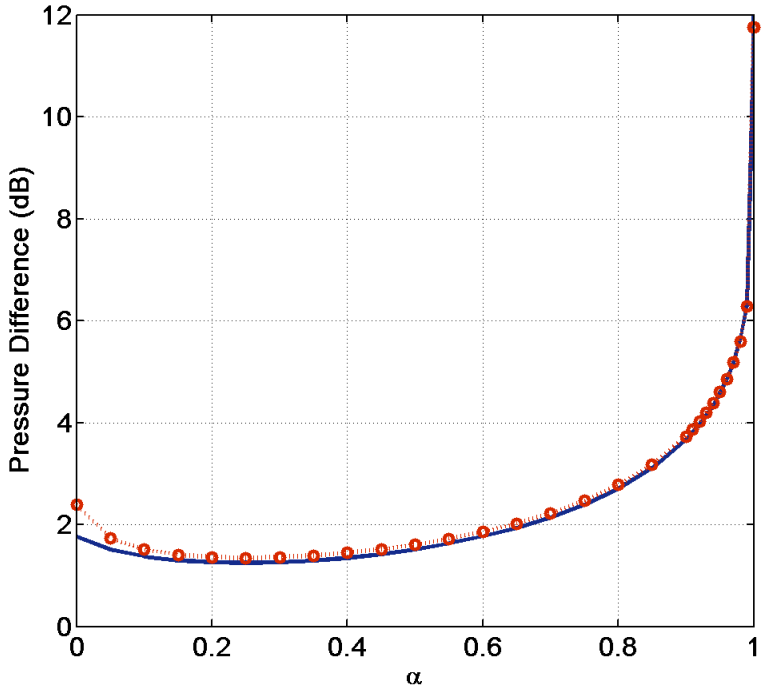

Figure 5.4 Averaged mean squared pressure at the remote location from the error sensor when GED is minimized. Eq. (5.26) is evaluated numerically and $10log(1+<\mu_s^2>/\mu_p^2)$ is plotted."——": analytical results; "· · ◯ · ·": numerical simulation.

experimentally that the averaged sound power ratio can be very high and cause an increase of more than 12 dB in the far-field of the error sensor when $\alpha \to 1$. Combining Eqs. (5.23)-(5.26), the far-field squared pressure value $\mu_p^2 + <\mu_s^2>$ can be evaluated numerically and is plotted in Fig. (5.4).

The value of α has a different impact on the near-field and the far-field regions of the sound pressure after ANC is implemented. To maximize the noise reduction at the error sensor location, α needs to be equal to one. On the other hand, however, the value of $\alpha = 1$ should be avoided due to the possible extremely high secondary source strength and significant amplification introduced in the far-field. The averaged sound pressure level around the error sensor is plotted in Fig. (5.5) for values of α being 0.999999, 0.95, 0.85 and

0.25. Because of the divergent nature of minimizing squared pressure, the value 0.999999 is used instead of one. One can observe from the plot that the 10 dB "quiet zone" for minimizing pressure is notably smaller than the generally reported volume - a sphere with diameter being one-tenth of the wavelength. This size, however, can be reached by setting $\alpha = 0.95$. If a controlled volume of 5 dB reduction is desired, a value of α in the range of approximately 0.85 to 0.95 can provide a "quiet zone" with the diameter being around one-fifth of the wavelength. In the far-field, greater than about half a wavelength away from the error sensor, the averaged pressure field is much lower for $\alpha < 0.95$ than for $\alpha \approx 1$. The theoretical minimum average far-field pressure can be achieved when $\alpha = 0.25$. However, for this case the largest noise reduction is only around 2 dB. In addition, the general "quiet zone", defined as the region where the noise is reduced, has a diameter of around two-fifths of the wavelength for $\alpha < 0.95$, which is notably larger than for $\alpha \approx 1$.

5.5 Numerical Simulation for the Zone of Quiet

Computer simulations were carried out to verify the theoretical derivations in Section 5.4. Inside a lightly damped room (dimensions: $2e\ m \times 2\pi\ m \times 6\ m$), the GED field of the primary point source is minimized at an error sensor location by one remotely placed secondary point source. The room has a uniform wall impedance, $z = (50 + 100i)\rho_0 c$, with the Schroeder frequency being 310 Hz. The error sensor is placed at 3/8 of the length along one diagonal line of the room. The primary and secondary source locations are randomly chosen within the region that is at least two wavelengths from the error sensor and the boundaries. Sound fields for a point source at 200 such selected random locations are computed with the hybrid modal expansion model at 800 Hz, which is well above the Schroeder frequency of the room to meet the diffuse field condition. Based on these 200 source locations, a search was carried out to look for two sources that are at least ten wavelengths away from each other. More than

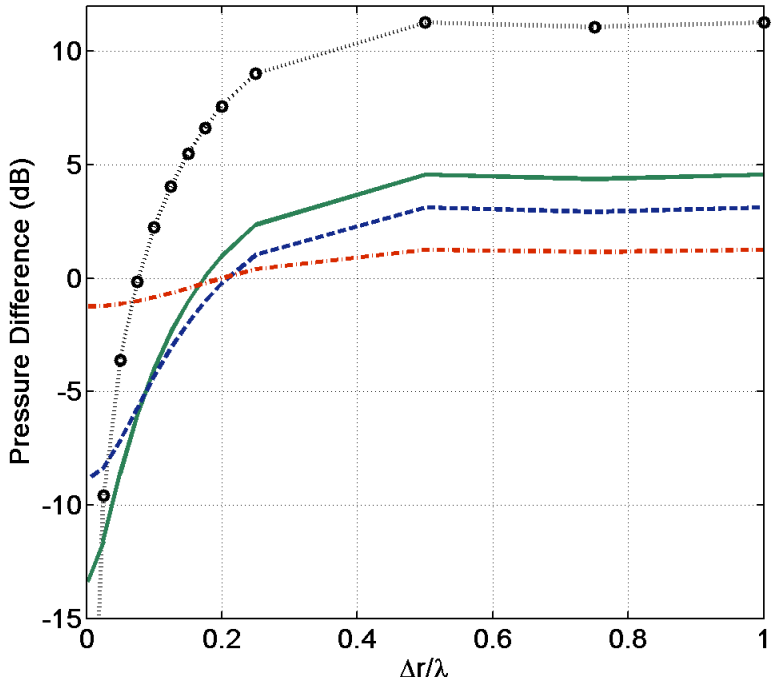

Figure 5.5 Averaged mean square pressure in the near-field of the error sensor when GED is minimized. Eq. (5.16) is evaluated numerically and $10log(\overline{< p^2(\mathbf{r_0} + \mathbf{\Delta r}) >}/< p_p^2 >)$ is plotted."• • ◯ • •": $E_{G(1)}$ (E_P); "——": $E_{G(0.95)}$; "– –": $E_{G(0.85)}$; "–·–": $E_{G(1/4)}$.

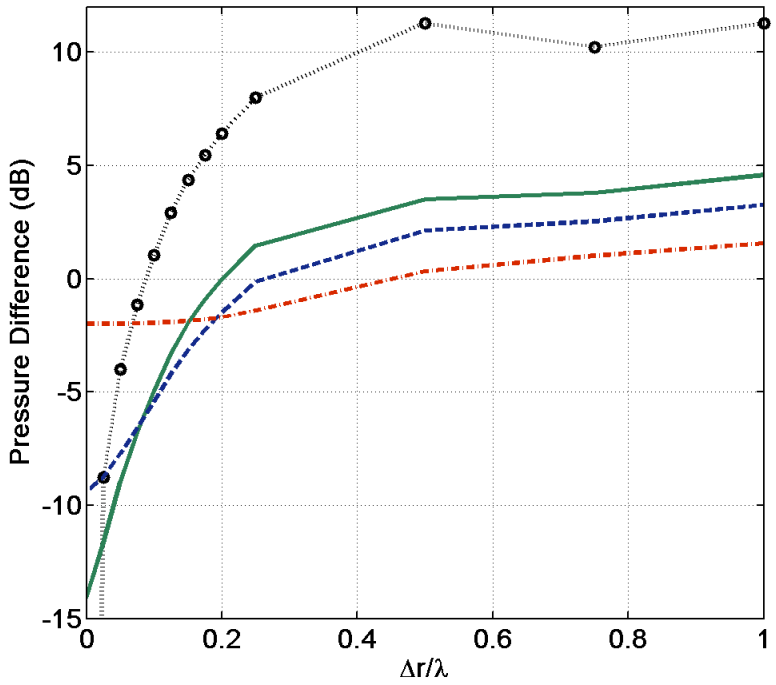

Figure 5.6 Averaged mean square pressure in the near-field of the error sensor when GED is minimized. This is a computer simulation result. "• • ◯ • •": $E_{G(1)}$ (E_P); "——": $E_{G(0.95)}$; "– –": $E_{G(0.85)}$; "–•–": $E_{G(1/4)}$.

4000 such pairs were found, and with each pair, one source was randomly selected to serve as the primary source while the other one was used as the secondary source. Since the complex source strengths are unity, the pressure and particle velocity fields computed correspond to the spatial transfer functions. Therefore, the secondary source strength required to minimize the GED response at the error sensor location can be calculated using Eq. (5.4). The controlled sound field is then computed by superposing the primary and secondary fields. The averaged squared pressure (over 4000 trials) at the error sensor location and at a remote region have been plotted in Figs. 5.3 and 5.4, to be compared with the analytical predictions. The averaged near-field results are plotted in Fig. 5.6 to verify the analytical results shown in Fig. 5.5. All the numerical simulations agree well with theoretical results.

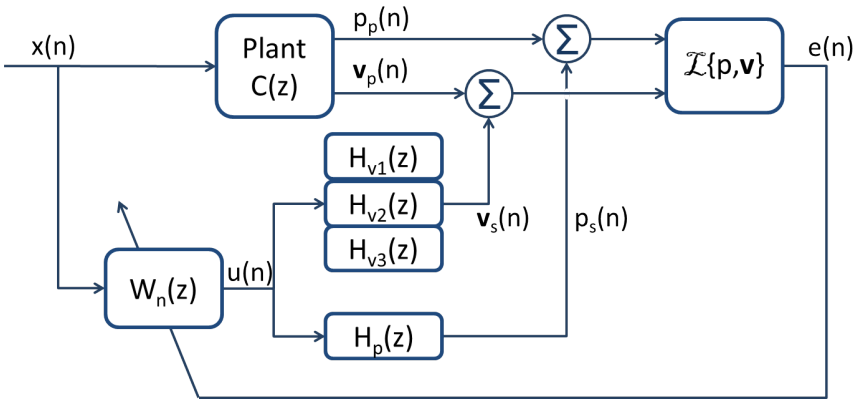

Figure 5.7 Block diagram of the energy-based filtered-x algorithm.

5.6 A Filtered-X Algorithm for GED

The ANC algorithm utilized in this study is based on a version of the widely used adaptive filtered-x algorithm, which has been modified for the minimization of the acoustic energy-based quantities.[66] A block diagram representing the ANC algorithm is shown in Fig. 5.7. In this figure, $p_p(n)$, $\mathbf{v}_p(n)$, $p_s(n)$ and $\mathbf{v}_s(n)$ represent the pressure and particle velocity at the error sensor due to the primary and secondary source, respectively. Here, n denotes a discrete-time index. W_n in the diagram represents the adaptive active control filter, while H_{vi} and H_p denote the transfer functions representing the secondary path for the particle velocity and pressure, respectively. The functions $\mathcal{J}\{p, \mathbf{v}\}$ in the figure represents a procedure of computing the squareroot of GED, and the output $e(n)$ can be calculated as

$$\begin{aligned} e(n) &= |E_G(n)|^{1/2} \\ &= \left[\frac{\alpha}{2\rho_0 c^2} p^2(n) + \frac{(1-\alpha)\rho_0}{2} \mathbf{v}(n) \cdot \mathbf{v}(n)\right]^{1/2}. \end{aligned} \tag{5.27}$$

Here, $p(n)$ and $\mathbf{v}(n)$ represent the pressure and particle velocity at the error sensor, which can be calculated using matrix notation as

$$\begin{aligned} p(n) &= p_p(n) + p_s(n) \\ &= p_p(n) + \mathbf{w}^T(n)\mathbf{X}(n)\mathbf{h}_p(n), \qquad (5.28a) \\ v_i(n) &= v_{pi}(n) + v_{si}(n) \\ &= v_{pi}(n) + \mathbf{w}^T(n)\mathbf{X}(n)\mathbf{h}_{vi}(n),\ i = 1, 2, 3, \qquad (5.28b) \end{aligned}$$

where $\mathbf{w}(n)$, $\mathbf{h}_p(n)$ and $\mathbf{h}_{vi}(n)$ denote the coefficient vectors for the finite impulse response (FIR) filters representing $W_n(z)$, $H_p(z)$ and $H_{vi}(z)$, respectively, and $\mathbf{X}(n)$ represents the reference signal matrix. These vector and matrix quantities can be written as follows:

$$\begin{aligned} \mathbf{w}(n) &= [w_0(n)\ w_1(n)\ \cdots\ w_{J-1}(n)]^T, \\ \mathbf{h}_p(n) &= [h_{p,0}(n)\ h_{p,1}(n)\ \cdots\ h_{p,I-1}(n)]^T, \\ \mathbf{h}_{vi}(n) &= [h_{vi,0}(n)\ h_{vi,1}(n)\ \cdots\ h_{vi,I-1}(n)]^T, \end{aligned}$$

and

$$\mathbf{X}(\mathbf{n}) = \begin{bmatrix} x(n) & x(n-1) & \cdots & x(n-I+1) \\ x(n-1) & x(n-2) & \cdots & x(n-I) \\ \vdots & \vdots & \vdots & \vdots \\ x(n-J+1) & x(n-J) & \cdots & x(n-I-J+2) \end{bmatrix}^T,$$

where I and J represent the length of the FIR filters W_n and H. In addition, the "filtered-x" signals are defined as follows

$$\begin{aligned} \mathbf{r}_p(n) &= \mathbf{X}(n)\mathbf{h}_p(n), \qquad (5.29a) \\ \mathbf{r}_{vi}(n) &= \mathbf{X}(n)\mathbf{h}_{vi}(n). \qquad (5.29b) \end{aligned}$$

With the substitution of Eqs. 5.28 and 5.29, one can obtain the gradient of the squared error signal as

$$\frac{\partial e^2(n)}{\partial \mathbf{w}} = \frac{\alpha}{\rho_0 c^2} p(n)\mathbf{r}_p + (1-\alpha)\rho_0 \sum_{l=1}^{3} v_i(n)\mathbf{r}_{vi}. \tag{5.30}$$

Thus, the control filter update equation can be written as

$$\mathbf{w}(n+1) = \mathbf{w}(n) - \mu_X \left[\frac{\alpha}{\rho_0 c^2} p(n)\mathbf{r}_p + (1-\alpha)\rho_0 \sum_{l=1}^{3} v_i(n)\mathbf{r}_{vi} \right], \tag{5.31}$$

where μ_X is the convergence parameter. With no surprise, this expression can revert to the active control filter update equations for minimizing the squared pressure, squared velocity or total acoustic energy density by choosing the appropriate corresponding value for α. Of note is the fact that an existing ANC system based on minimizing E_T can be very easily modified to minimize E_G instead.

5.7 Experimental Study of ANC in a Diffuse Field

An experimental study was carried out in a reverberation chamber which has dimensions of 4.96 m × 5.89 m × 6.98 m (a volume of 204 m^3) and is incorporated with stationary diffusers. The Schroeder frequency for this chamber is 410 Hz. The pressure microphone gradient probe served as the error sensor One loudspeaker driven by a 650 Hz pure-tone signal served as the primary source while another identical loudspeaker was used as the secondary source to minimize the E_G response at the error sensor. Twenty tests were carried out. The error sensor was located near the center of the chamber and the location remained constant. The locations of the two sources were chosen randomly for each test, but the sources were at least two wavelengths from the boundaries and the error sensor. The distance between the two sources was at least 5 wavelengths away from each other. The sound pressure fields both without and with control were sampled at different distances from the error

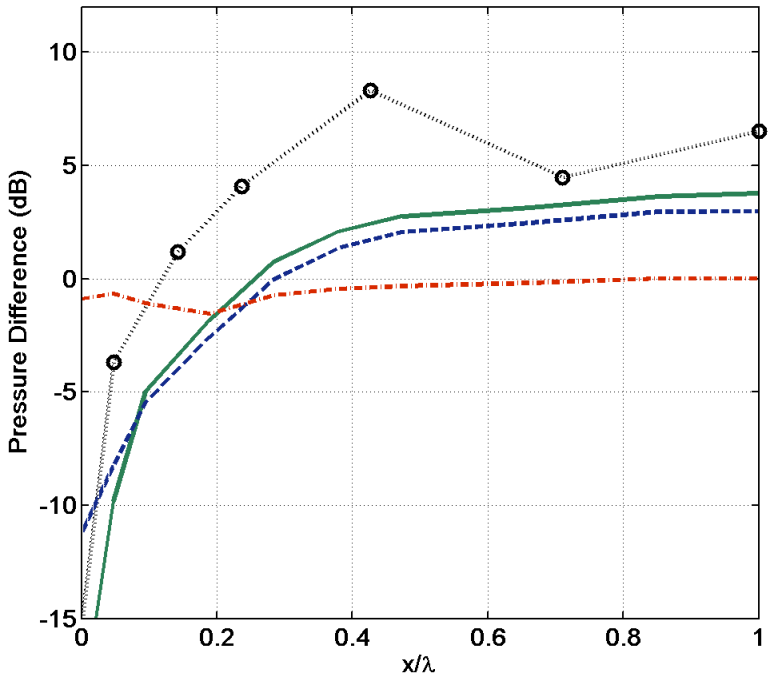

Figure 5.8 Experimental results for averaged mean square pressure in the near-field of the error sensor when GED is minimized. "••◯••": $E_{G(1)}$ (E_P); "——": $E_{G(0.95)}$; "– –": $E_{G(0.85)}$; "–·–": $E_{G(1/4)}$.

sensor. The averaged difference between the sound pressure fields with control on and off are calculated and plotted in Fig. 5.8 with respect to the distance from the error sensor for some specific values of α. Simultaneously, the far-field pressure field was sampled with six far-field microphones. The difference between the averaged far-field squared pressure values for control on and off are plotted in Fig. 5.9 as a function of α. The experimental results agree with the theoretical and computer simulation results fairly well.

5.8 Conclusions

GED-based active noise control is studied in this chapter. Global active noise control in a lightly damped enclosure has been studied through computer simulation. The results

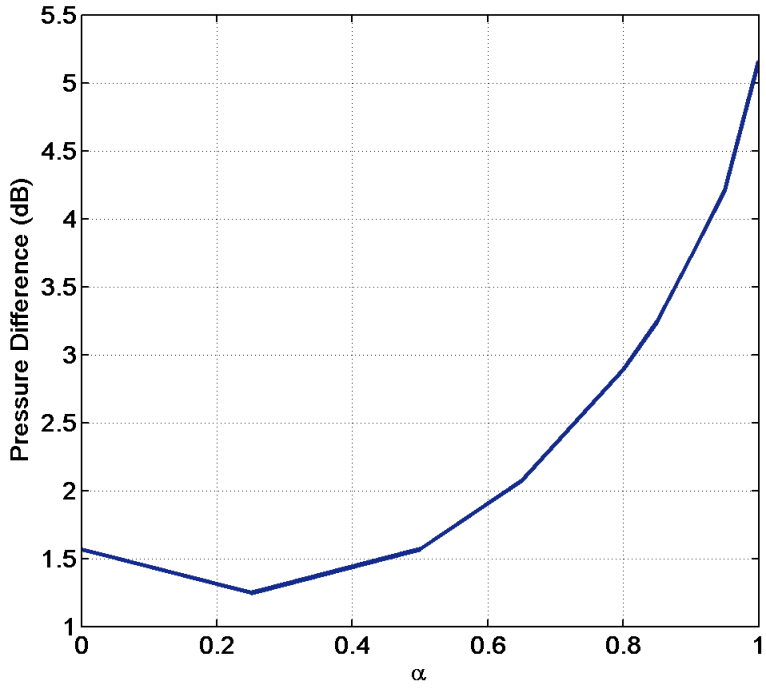

Figure 5.9 Experimental results for averaged mean squared pressure at the remote location from the error sensor when GED is minimized.

demonstrated that when $\alpha \leq 1/2$, the average global attenuation is not particularly sensitive to the specific value of α, but $E_{G(1/4)}$ introduces less variance for the attenuation than other quantities. For diffuse sound fields, the averaged zone of quiet in the near-field of the error sensor was derived theoretically and verified by a numerical simulation. Compared to minimizing squared pressure response, by varying the value of α of GED, one can increase the general zone of quiet by as much as 3 times. As a trade off, the maximum attenuation may decrease to around 1.25 dB. By choosing appropriate values of α, one can maximize the volume of the quite zone and at the same time obtain the desired attenuation. For example, if 10 dB zone of quiet is required, a value of 0.95 may be assigned to α. When the attenuation of 5 dB is desired, a value of 0.85 should be assigned to α. In the far-field of the error sensor, there is usually a boost for the squared pressure. However, it was shown in this work that by minimizing the GED response with $\alpha < 1$, the boost in the far-field can be dramatically reduced.

A modified filtered-x adaptive algorithm was developed in this paper for GED-based ANC. The algorithm is very similar to that for minimizing the total acoustic energy density that was developed previously in the literature, and, in practice, very limited effort is needed to modifying a existing ED-based ANC system to a GED-based ANC system.

The experimental study conducted in a reverberation chamber largely confirmed the theoretical results derived in the paper.

Chapter 6

Conclusions and Recommendations for Future Work

6.1 Conclusions

Different modal expansion methods have been studied in this dissertation. A set of new room modes are introduced to deal with damped enclosures. Moreover, a free field Green's function is integrated into the solution of the non-homogeneous Helmholtz equation to improve both the convergence rate and the accuracy of modal expansions. For damped boundary conditions, by partially satisfying the boundary conditions, the modified modal analysis (MMA) not only performs better than the classical modal analysis (CMA) in the region near boundaries but also is more accurate globally with fewer modes used in the expansion. In addition, the "uncoupled" MMA can predict sound pressure level and particle velocity level fairly accurately for many damped boundary conditions, while the "uncoupled" CMA usually introduces large errors. Generally, MMA requires numerical searching for the eigenvalues. However, this process is fairly straightforward and fast. The enclosed sound field can

be separated into the direct field and reverberant field, but these two are treated together in the traditional modal analysis. The weaknesses include slow convergence rate (especially in the near field of a point source) and difficulty in dealing with complex sources inside an enclosure. The hybrid modal expansion introduced in Chapter 2 successfully addresses these problems. Studies using a point source in rectangular enclosures show that it converges notably faster than the regular modal expansion and the hybrid "uncoupled" modal expansion introduces much smaller errors than the regular "uncoupled" expansion. The hybrid expansion can be easily applied to complex sound sources if the free field responses of the sources are known.

Generalized acoustic energy density (GED) has been introduced in this dissertation. Averaging over the volume of an enclosure, the GED has the same mean value as the acoustic total energy density and can revert to the traditional energy density quantities, such as acoustic potential energy density, acoustic kinetic energy density, and acoustic total energy density. By varying the weighting factors for the combination of acoustic potential energy density and acoustic kinetic energy density, an additional degree of freedom is added to the summed energy density quantity so that it can be optimized for different applications. Properties for GED with different values of the weighting factor, α, have been studied for individual room modes, for the diffuse sound field, and for the sound field below the Schroeder frequency.

The uniformity of a measured sound field often plays an important role in many applications. This work has shown that optimal weighting factors based on the single parameter α can minimize the spatial variance of the GED. For a single room mode, the optimal value of α may vary from 1/10 to 1/2, depending on the specific mode shape. For a diffuse field, the optimal value is 1/4 for both single frequency and narrow-band frequency excitations, even for the region close to a rigid reflecting surface. For a diffuse field excited by a single tone

source, this $E_{G(1/4)}$ follows the distribution of $Gamma(4, \mu_0/4)$ and has a relative spatial variance of 1/4, compared to 1/3 for E_K and E_T. Below the Schroeder frequency of a room, a smaller ensemble variance can also be reached when $\alpha = 1/4$.

Benefits of total-energy-density-based techniques have been shown in the past. Experimental studies of GED-based reverberation time and sound power measurements in a reverberation chamber confirm the improved uniformity of $E_{G(1/4)}$, especially in the low-frequency region. They indicate that more reliable results may be obtained using $E_{G(1/4)}$ for those measurements. Global active noise control in a lightly damped enclosure has also been studied through computer simulation. The results demonstrated that when $\alpha \leq 1/2$, the average global attenuation is not particularly sensitive to the specific value of α, but $E_{G(1/4)}$ introduces less variance for the attenuation than other quantities. For diffuse fields, the zone of quiet is usually very small around a pressure error sensor for active noise control. GED-based active noise control can not only increase the size of the quiet zone, but also dramatically decrease the boost in the far field caused by the secondary source.

In general, GED-based techniques result in significant improvements compared to potential energy density-based techniques. Utilizing E_G can often yield favorable results compared to E_T. However, the degree of the improvements may not be large. Nonetheless, since E_G requires no additional effort to implement in most applications, and it is very simple to modify existing E_T-based techniques, the GED-based techniques may be considered to be superior. In addition, because of the additional degree of freedom, the GED can be utilized in broader applications.

6.2 Suggestions for Future Research

Studies have been carried out for some GED-based applications such as acoustic measurement techniques in a reverberation chamber and active noise control of enclosed sound fields.

There are broad areas that GED can be applied to. Applications such as sound equalization, acoustic source power measurement in standard non-ideal rooms, and so on could possibly benefit from the improved uniformity properties of GED.

The generalized energy density weights the potential energy density and the kinetic energy density differently to introduce an additional degree of freedom. There is a potential to extend this idea even further. One possibility is to weight the orthogonal components of the kinetic energy density differently. A preliminary study on active noise control in a diffuse field showed that by choosing different weighting factors for the kinetic energy density components, a similar volume of the zone of quiet can be achieved compared to the GED based techniques, which suggests the possibility of reducing the number of channels for the error sensor. In addition, the shape of the zone of quiet may not remain spherical. Thus, by choosing appropriate weighting factors, one may be able to adjust the shape and orientation of the zone of quiet.

Bibliography

[1] W. C. Sabine, *Collected papers on acoustics* (Dover Publications, New York,) (1964).

[2] I. Wolff and F. Massa, "Direct meaurement of sound energy density and sound energy flux in a complex sound field", J. Acoust. Soc. Am. **3**, 317–318 (1932).

[3] I. Wolff and F. Massa, "Use of pressure gradient microphones for acoustical measurements", J. Acoust. Soc. Am. **4**, 217–234 (1933).

[4] L. W. Sepmeyer and B. E. Walker, "Progress report on measurement of acoustic energy density in enclosed spaces", J. Acoust. Soc. Am. **55**, S12 (1974).

[5] R. V. Waterhouse, "Statistical properties of reverberant sound fields", J. Acoust. Soc. Am. **43**, 1436–1444 (1968).

[6] R. H. Lyon, "Statistical analysis of power injection and response in structures and rooms", J. Acoust. Soc. Am. **45**, 545–565 (1969).

[7] R. K. Cook and P. A. Schade, "New method for measurement of the total energy density of sound waves", in *Inter-Noise*, 101–106 (Washington DC) (1974).

[8] R. V. Waterhouse and R. K. Cook, "Diffuse sound fields: Eigenmode and free-wave models", J. Acoust. Soc. Am. **59**, 576–581 (1976).

[9] R. V. Waterhouse and D. W. v. W. Palthe, "Space variance for rectangular modes", J. Acoust. Soc. Am. **62**, 211–213 (1977).

[10] F. Jacobsen, "The diffuse sound field: statistical considerations concerning the reverberant field in the steady state", Technical Report, Technical University of Denmark (1979).

[11] J. A. Moryl and E. L. Hixson, "A total acoustic energy density sensor with applications to energy density measurement in a reverberation room", Proceedings of Inter-Noise **II**, 1195–1198 (1987).

[12] J. A. Moryl, "A study of acoustic energy density in a reverberation room.", Ph.D. thesis, The University of Texas at Austin (1987).

[13] R. L. Weaver and J. Burkhardt, "Weak Anderson localization and enhanced backscatter in reverberation rooms and quantum dots", J. Acoust. Soc. Am. **96**, 3186–3190 (1994).

[14] F. Jacobsen and A. R. Molares, "Sound power emitted by a pure-tone source in a reverberation room", J. Acoust. Soc. Am. **126**, 676–684 (2009).

[15] F. Jacobsen and A. R. Molares, "The ensemble variance of pure-tone measurements in reverberation rooms", J. Acoust. Soc. Am. **127**, 233–237 (2010).

[16] J. L. Davy, "The relative variance of the transmission function of a reverberation room", J. Sound Vib. **77**, 455–479 (1981).

[17] R. L. Weaver, "On the ensemble variance of reverberation room transmission functions, the effect of spectral rigidity", J. Sound Vib. **130**, 487–491 (1989).

[18] F. Jacobsen and A. R. Molares, "Statistical properties of kinetic and total energy densities in reverberant spaces", J. Acoust. Soc. Am. **127**, 2332–2337 (2010).

[19] J. W. Parkins, S. D. Sommerfeldt, and J. Tichy, "Error analysis of a practical energy density sensor", J. Acoust. Soc. Am. **108**, 211–222 (2000).

[20] B. S. Cazzolato and C. H. Hansen, "Errors arising from three-dimensional energy density sensing in one-dimensional sound fields", J. Sound Vib. **236**, 375–400 (2000).

[21] J. Ghan, B. Cazzolato, and S. Snyder, "Statistical errors in the estimation of time-averaged acoustic energy density using the two-microphone method", Journal of the Acoustical Society of America **115**, 1179–1184 (2004).

[22] J.-C. Pascal and J.-F. Li, "A systematic method to obtain 3d finite-difference formulations for acoustic intensity and other energy quantities", J. Sound Vib. **310**, 1093–1111 (2008).

[23] B. H.-E. De, P. Leussink, T. Korthorst, H. Jansen, T. S. J. Lammerink, and M. Elwenspoek, "The u-flown: A novel device for measuring acoustic flows", Sensors and Actuators, A: Physical **54**, 552–557 (1996).

[24] T. G. H. Basten and H.-E. d. Bree, "Full bandwidth calibration procedure for acoustic probes containing a pressure and particle velocity sensor", J. Acoust. Soc. Am. **127**, 264–270 (2010).

[25] J. W. Parkins, "Active minimization of energy density in a three-dimensional enclosure", Dissertation, The Pennsylvania State University (1998).

[26] J. W. Parkins, S. D. Sommerfeldt, and J. Tichy, "Narrowband and broadband active control in an enclosure using the acoustic energy density", J. Acoust. Soc. Am. **108**, 192–203 (2000).

[27] D. B. Nutter, T. W. Leishman, S. D. Sommerfeldt, and J. D. Blotter, "Measurement of sound power and absorption in reverberation chambers using energy density", J. Acoust. Soc. Am. **121**, 2700–2710 (2007).

[28] A. D. Pierce, *Acoustics : an introduction to its physical principles and applications*, McGraw-Hill series in mechanical engineering (McGraw-Hill Book Co., New York) (1981).

[29] L. Cremer and H. A. Muller, *Principles and Applications of Room Acoustics*, english language edition (Applied Science, London) (1982).

[30] P. M. Morse and K. U. Ingard, *Theoretical Acoustics* (McGraw-Hill, New York) (1968).

[31] E. H. Dowell, G. F. Gorman, and D. A. Smith, "Acoustoelasticity: General theory, acoustic natural modes and forced response to sinusoidal excitation, including comparisons with experiment", J. Sound Vib. **52**, 519–542 (1977).

[32] Y. Kubota and E. H. Dowell, "Asymptotic modal analysis for sound fields of a reverberant chamber", J. Acoust. Soc. Am. **92**, 1106–1112 (1992).

[33] L. Meirovitch and P. Hagedorn, "A new approach to the modelling of distributed non-self-adjoint systems", J. Sound Vib. **178**, 227–241 (1994).

[34] J. Pan, S. J. Elliott, and K. H. Baek, "Analysis of low frequency acoustic response in a damped rectangular enclosure", J. Sound Vib. **223**, 543–566 (1999).

[35] L. P. Franzoni and E. H. Dowell, "On the accuracy of modal-analysis in reverberant acoustical systems with damping", J. Acoust. Soc. Am. **97**, 687–690 (1995).

[36] W. P. Mason and R. N. Thurston, *Physical Acoustics: Principles and Methods*, volume XVII (Academic Press, New York,) (1984).

[37] P. M. Morse and R. H. Bolt, "Sound waves in rooms", Review of Modern Physics **16**, 69–150 (1944).

[38] G. B. Arfken and H.-J. Weber, *Mathematical methods for physicists*, 5th edition (Harcourt/Academic Press, San Diego) (2001).

[39] S. R. Bistafa and J. W. Morrissey, "Numerical solutions of the acoustic eigenvalue equation in the rectangular room with arbitrary (uniform) wall impedances", J. Sound Vib. **263**, 205–218 (2003).

[40] Y. Naka, A. A. Oberai, and B. G. Shinn-Cunningham, "Acoustic eigenvalues of rectangular rooms with arbitrary wall impedances using the interval Newton/generalized bisection method", J. Acoust. Soc. Am. **118**, 3662–3671 (2005).

[41] D.-Y. Maa, "Sound field in a room and its active noise control", Applied Acoustics **41**, 113–126 (1994).

[42] D.-Y. Maa, "Formula of sound field in a room, re-examination", Shengxue Xuebao/Acta Acustica **27**, 385–388 (2002).

[43] J. Pan, "A 2nd note on the prediction of sound intensity", J. Acoust. Soc. Am. **97**, 691–694 (1995).

[44] M. P. Morse, "The transmission of sound inside pipes", J. Acoust. Soc. Am. **11**, 205–210 (1939).

[45] L. E. Kinsler, *Fundamentals of acoustics*, 4th edition (John Wiley & Sons, Inc., New York) (2000).

[46] J. Pan, "A note on the prediction of sound intensity", J. Acoust. Soc. Am. **93**, 1641–1644 (1993).

[47] L. L. Beranek, *Acoustics* (McGraw-Hill, New York) (1954).

[48] C. F. Eyring, "Reverberation time in "dead" rooms", J. Acoust. Soc. Am. **1**, 168 (1930).

[49] W. B. Joyce, "Exact effect of surface roughness on the reverberation time of a uniformly absorbing spherical enclosure", J. Acoust. Soc. Am. **64**, 1429–1436 (1978).

[50] W. B. Joyce, "Power series for the reverberation time", J. Acoust. Soc. Am. **67**, 564–571 (1980).

[51] M. Hodgson, "Experimental evaluation of the accuracy of the sabine and eyring theories in the case of non-low surface absorption", J. Acoust. Soc. Am. **94**, 835–840 (1993).

[52] L. L. Beranek, "Analysis of sabine and eyring equations and their application to concert hall audience and chair absorption", J. Acoust. Soc. Am. **120**, 1399–1410 (2006).

[53] Y. Jing and N. Xiang, "On boundary conditions for the diffusion equation in roomacoustic prediction: Theory, simulations, and experiments", J. Acoust. Soc. Am. **123**, 145–153 (2008).

[54] D. Lubman, "Fluctuations of sound with position in a reverberant room", J. Acoust. Soc. Am. **44**, 1491–1502 (1968).

[55] R. K. Cook, R. V. Waterhouse, R. D. Berendt, S. Edelman, and J. M. C. Thompson, "Measurement of correlation coefficients in reverberant sound fields", J. Acoust. Soc. Am. **27**, 1072–1077 (1955).

[56] D. Lubman, "Spatial averaging in a diffuse sound field", J. Acoust. Soc. Am. **46**, 532–534 (1969).

[57] S. J. Elliott, P. Joseph, A. J. Bullmore, and P. A. Nelson, "Active cancellation at a point in a pure tone diffuse sound field", J. Sound Vib. **120**, 183–189 (1988).

[58] R. V. Waterhouse, "Interference patterns in reverberant sound fields", J. Acoust. Soc. Am. **27**, 247–258 (1955).

[59] M. R. Schroeder, "New method of measuring reverberation time", J. Acoust. Soc. Am. **37**, 409–412 (1965).

[60] P. A. Nelson, A. R. D. Curtis, S. J. Elliott, and A. J. Bullmore, "The active minimization of harmonic enclosed sound fields, part i: Theory", J. Sound Vib. **117**, 1–13 (1987).

[61] A. J. Bullmore, P. A. Nelson, A. R. D. Curtis, and S. J. Elliott, "The active minimization of harmonic enclosed sound fields, part ii: A computer simulation", J. Sound Vib. **117**, 15–33 (1987).

[62] S. J. Elliott, A. R. D. Curtis, A. J. Bullmore, and P. A. Nelson, "Active minimization of harmonic enclosed sound fields, part iii: Experimental verification", J. Sound Vib. **117**, 35–58 (1987).

[63] P. Nelson and S. Elliott, *Active control of sound* (Academic Press, London) (1993).

[64] P. Joseph, S. J. Elliott, and P. A. Nelson, "Near field zones of quiet", J. Sound Vib. **172**, 605–627 (1994).

[65] P. Joseph, S. J. Elliott, and P. A. Nelson, "Statistical aspects of active control in harmonic enclosed sound fields", J. Sound Vib. **172**, 629–655 (1994).

[66] S. D. Sommerfeldt and P. J. Nashif, "An adaptive filtered-x algorithm for energy-based active control", J. Acoust. Soc. Am. **96**, 300–306 (1994).